



McGill

Design and validation of an Argon Laser Thermal Propulsion Thruster Powered by a Fiber Laser

Gabriel Roland Dubé

Department of Mechanical Engineering
McGill University, Montreal

December 2024

A thesis submitted to McGill University
in partial fulfillment of the requirements of the degree of
Master of Science

Contents

List of Figures	v
List of Tables	vi
Abstract	vii
Résumé	viii
Acknowledgements	ix
1 Introduction	1
1.1 Motivation	1
1.2 Literature review	3
1.3 Summary and direction of work in this thesis	9
2 Modelling heat capacity	13
2.1 Equilibrium calculations	13
3 Facility design	17
3.1 Version 1 test section	17
3.2 Version 2	17
3.2.1 Requirements	17
3.2.2 Initial sizing of the double choked LTP thruster	21
3.2.3 Test section and thrust stand	22
3.2.4 Laser and optics	23
3.2.5 Timing control	25
3.2.6 Data acquisition (DAQ) system and oscilloscope	25
3.2.7 Cameras	26
3.2.8 Spark initiation system	27

3.2.9	Needle valve	27
4	Experiments	30
4.1	Static LSP validation	30
4.1.1	V1 LSP spark initiation	30
4.1.2	NO ₂ seeding	32
4.1.3	V2 LSP spark initiation and QCW LSP	33
4.1.4	Optical experiments: going from QCW to CW LSP	34
4.1.5	V2 CW LSP	38
4.2	V2 Cold flow thruster characterization	41
4.2.1	Cold flow thrust tests	41
4.2.2	Thruster nozzle effective sonic area A^*	43
4.2.3	Needle valve effective sonic area A^*	45
4.2.4	Summary of results	46
4.3	Initial QCW LSP thrust tests (hot fire)	46
5	Discussion	49
6	Conclusion	56
References		57
A	YLR-300/3000-QCW-MM-AC Calibration Report	61
B	P30 Collimator Calibration Report	68
C	Bubble Meter Calibration Report and A^* Calculation	70
D	Omega PX119A-1KG5V Calibration	77
E	V2 Test Section Parts Drawings	79
F	V2 Second (Rear) Window Mount	88
G	Untested V2 Parts Drawings	90

List of Figures

1.1	LTP architecture (Duplay [4])	2
1.2	Overview of LTP system (Duplay [4])	2
1.3	Cross-section drawing of 10 kW thruster from Shoji [6] (original is of poor quality)	3
1.4	Experimental apparatus from Keefer <i>et al.</i> [8]	4
1.5	Experimental apparatus from Zerkle <i>et al.</i> [10]	5
1.6	Apparatus used in Black <i>et al.</i> [12]	6
1.7	Two thruster models from Toyoda <i>et al.</i> [13]	7
1.8	Experimental setup from Lu <i>et al.</i> [14]	8
1.9	LSP setups from Takano <i>et al.</i> [16]	9
2.1	Gibbs free energy (G) plotted against the degree of dissociation of hydrogen under three different pressures	15
2.2	Comparing calculated C_p values of argon to those from CEA	16
3.1	V1 LTP thruster from Duplay [4]	18
3.2	Render of the V2 LTP thruster	19
3.3	Cutaway of a double choked LTP thruster showing both choking orifices: the metering valve and the nozzle.	21
3.4	V2 LTP thruster	23
3.5	V2 LTP thruster	24
3.6	Laser system	24
3.7	Electronics rack with laser at the base	25
3.8	Delay generators and oscilloscope	26
3.9	DAQ system	26
3.10	Spark initiation system. On the left is a power supply, while spark coil number 6 is on the right.	27
3.11	Assembled electrodes with Ultra-Torr cap and electrical connectors	28

3.12 WL14H-320P Needle valve	28
3.13 Size comparison between V1 (top) and V2 (bottom). V2 is in static configuration, without the extension cylinder.	29
4.1 V1 spark alignment	31
4.2 Signal timing diagram. The <i>trig</i> prefix denotes triggering signals. The component is active when the line is high. Timings in ms are also indicated on the figure.	31
4.3 QCW LSP spark initiation in V1: 3079 W, 20 bar. LSP142_SPRK15.	32
4.4 Average dynamic pressure rise of QCW LSP shots in a mixture of NO ₂ and argon compared to that of pure argon QCW LSP	33
4.5 2 FOVs of alignment laser light on power meter. The aberration at the center of the red light is due to laser damage to the window.	34
4.6 100% power (3079 W) QCW LSP shot	34
4.7 LSP threshold graph for V1 with 125 mm focal length lens	36
4.8 Model of the lenses showing paraxial rays and focus	37
4.9 Spot diagrams of the three lens systems studied	38
4.10 LSP threshold graph for V1 with dual-lens system	39
4.11 LSP threshold graph for V2 with dual-lens system	39
4.12 First CW LSP captured by the webcam: 342 W, 20.0 bar. LSP385_V2_CW1. .	40
4.13 First CW LSP captured by the Photron high-speed camera: 314 W, 20.0 bar. LSP385_V2_CW1.	40
4.14 Dynamic pressure rise from CW LSP measured with PCB transducer	41
4.15 Typical cold flow pressure and thrust curves for 20 bar chamber pressure . .	42
4.16 Absolute pressure versus thrust and curve fit of pressure-thrust relation . .	42
4.17 Multiple cold flow thrust tests in succession	43
4.18 Saad blowdown model and experimental data	44
4.19 Bubble meter setup	45
4.20 Two QCW thrust tests	47
4.21 Nozzle ablation during flowing test. LSP315_V2_Flow4.	47
4.22 V2 Flowing QCW LSP. LSP321_V2_Flow10.	48
5.1 V1 single plug electrodes	50
5.2 V1 with newly machined opposing bottom ports	50
5.3 Electrode manufacturing process	51
5.4 Ablation damage to the flat rear plate of the thruster after two 3 kW laser shots	52
5.5 Rear window damage on V2	53

LIST OF FIGURES

LIST OF FIGURES

5.6 Window extension tube	54
5.7 Nozzle laser damage	55
5.8 New nozzle parts	55

List of Tables

1.1	Summary of a selection of past LSP experiments. λ : wavelength, P : maximum laser power, p : pressure, \dot{m} : mass flow rate, I_{sp} : maximum specific impulse, F_T : maximum thrust	11
1.2	Comparative table of experimental LTP thruster efficiencies	12
4.1	Statistics from the power meter after 10 times 50 ms laser shots at 10 % and 12 % power	35
4.2	Simulated focal length and spot diameter of various lens assemblies in Win-Lens3D. The average laser flux is calculated for 342 W of incident power . .	37
4.3	Calculated Opening Area for Needle Valve at Different Rotations (Upstream Pressure = 5000 kPa and Outlet Pressure = 100 kPa), adapted from Appendix C	46
4.4	Summary of the studied V2 thruster characteristics	46

ABSTRACT

Recent advancements in space commercialization have made access to low Earth orbit (LEO) more affordable. However, for ambitious missions like rapid human transit to Mars, existing propulsion methods fall short. Laser-Thermal Propulsion (LTP) emerges as a promising solution, utilizing lasers to heat propellant gas and generate thrust with greater efficiency than traditional rocket engines. The objective of this thesis was to test a Version 1 (V1) lab-scale LTP thruster for interplanetary space flight, as well as design and test an improved Version 2 (V2) thruster. These will both be powered by a 300 W Continuous Wave (CW), 3 kW Quasi-Continuous Wave (QCW) 1.07 μm fiber laser. Argon is used as the propellant at a pressure of 20 bar. Spark initiation of QCW Laser-Supported Plasma (LSP) was successfully implemented in V1 and V2. NO₂ seeding of the argon at partial pressures between 0.12 bar to 0.55 bar showed the gas absorbed more than double the laser energy compared to pure argon propellant. A CW LSP was achieved in V2, lasting 85.1 ms. This represents a 1.7 times longer lifetime than the maximum QCW pulse length of 50.0 ms at this power. Average cold flow thrust of V2 was 0.96 N. Parts to further improve V2 are presented to eventually enable a CW hot fire test of the thruster.

RÉSUMÉ

Les progrès récents de la commercialisation de l'espace ont rendu l'accès à l'orbite terrestre basse (LEO) plus abordable. Cependant, pour des missions ambitieuses telles que le transit humain rapide vers Mars, les méthodes de propulsion existantes ne sont pas à la hauteur. La propulsion laser-thermique (LTP) apparaît comme une solution prometteuse, utilisant des lasers pour chauffer le gaz propulseur et générer une poussée avec une plus grande efficacité que les moteurs fusées traditionnels. L'objectif de cette thèse était de tester un propulseur LTP Version 1 (V1) à l'échelle du laboratoire pour les vols spatiaux interplanétaires, ainsi que de concevoir et de tester un propulseur Version 2 (V2) amélioré. Ces deux propulseurs seront alimentés par un laser à fibre de $1.07\text{ }\mu\text{m}$ ayant une puissance ondes continues (CW) de 300 W et une puissance à ondes quasi continues (QCW) de 3 kW. L'argon est utilisé comme gaz propulseur à une pression de 20 bar. L'amorçage par étincelle du plasma soutenu par laser (LSP) QCW a été implémenté avec succès dans V1 et V2. L'ensemencement de l'argon en NO_2 à des pressions partielles comprises entre 0.12 bar to 0.55 bar a montré que le gaz absorbait plus du double de l'énergie laser par rapport à de l'argon pur. Un LSP CW a été obtenu avec V2, d'une durée de 85.1 ms. Cela représente une durée de vie 1.7 fois plus longue que la longueur d'impulsion QCW maximale de 50.0 ms à cette puissance. La poussée moyenne à froid de V2 était de 0.96 N. Des pièces permettant d'améliorer encore V2 sont présentées afin de permettre éventuellement un essai CW à chaud du propulseur.

ACKNOWLEDGEMENTS

Re-write Ac-
knowle-
gments

First, I want to thank my supervisor, Professor Andrew J. Higgins, for his deep knowledge, mentorship and support throughout this journey. I also want to thank him for giving me, and the lab, the singular opportunity to pursue graduate studies on advanced space propulsion. In Canada, this is a rare topic of research indeed, but it is only with advances in this field that humanity will be able to reach the stars.

I would like to extend my heartfelt appreciation to the members of the McGill Interstellar Flight Experimental Research Group. Emmanuel and Siera, in the pursuit of science together, you have given me dear memories that will last a lifetime. I wish Siera much success in continuing the work Emmanuel and I have but started.

Sebastian helped manufacture the V2 electrodes. Thank you for your knowledge on how to do things in the lab.

Editorial help was provided by Emmanuel Duplay, Siera Riel, John Kokkalis, Sebastian Rodriguez, and Dan-Cornelius Savu.

Thank you to my parents, who have always encouraged me in my studies. My thanks to Anna, for always listening to my late night rants.

My thanks to Alain Halbouny, Jade Tabbara, Karl Atallah, Serge Rubeiz, and Shady Tawil for designing and assembling the second version (V2) laser-thermal thruster, as well as producing its drawings and beautiful renders. Thank you to Meisam Aghajani, Mathieu Beauchesne, Ramnarine Harihar (Harry), and Andy Hofmann, the machinists who built it. Without V2, we would not have the experimental insights we have today.

Thank you Thariq Meulendijks for the needle valve A^* calibration and for help with bubble meter experiments.

This work was funded by the Natural Sciences and Engineering Research

Council of Canada (NSERC) Canada Graduate Scholarships — Master's (CGS-M) program and the McGill Summer Undergraduate Research in Engineering (SURE) program.

Chapter 1

Introduction

1.1 Motivation

In 2016, Lubin [1] proposed sending 1 g space probes to Alpha Centauri at 20 % the speed of light, using massive ground-based laser arrays. This could be enabled by a Moore's law in fiber laser technology, with a rapid doubling of power and a similar exponential decrease in costs.

As a near-term stepping stone using a smaller array, the laser can be coupled to a gas, reducing efficiency but increasing thrust. This process, Laser-Thermal Propulsion (LTP), would allow rapid interplanetary transfers, notably to Mars. The concept of LTP was first suggested by Kantrowitz [2] as a way to decrease launch costs and continues to be of interest. A conceptual design of an LTP spacecraft was proposed by Duplay *et al.* [3], with a similar architecture to Lubin [1]: a 10 m laser array beams 100 MW of power to an orbiting spacecraft for injection burns (Figure 1.1). With a 1 ton payload, 6 kN of thrust and 3000 s of I_{sp} , a 1 h laser beaming maneuver gives 14 km/s of delta-V to the spacecraft, which reaches Mars in 45 days.

Initially, hydrogen propellant is introduced in the thrust chamber of the vehicle. The laser is focused inside the chamber (see Figure 1.2) and is absorbed by the gas via inverse Bremsstrahlung, creating a Laser-Supported Plasma (LSP) core. Colder hydrogen flows around the LSP core and is heated by it to 10 000 K. The hot gas is then exhausted through a conventional converging-diverging nozzle at the exhaust velocity, imparting thrust to the vehicle.

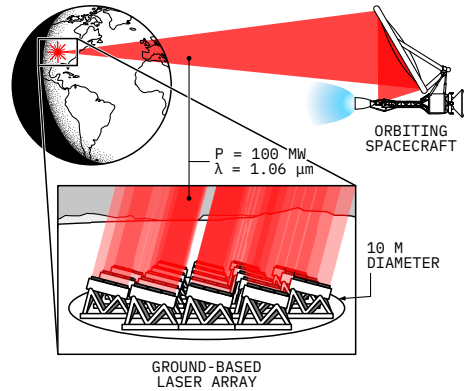


Figure 1.1: LTP architecture (Duplay [4])

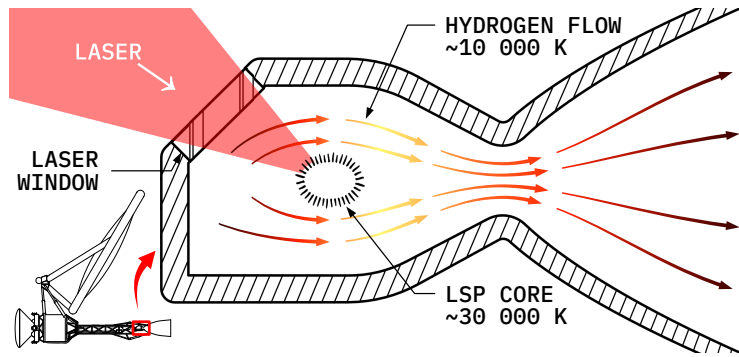


Figure 1.2: Overview of LTP system (Duplay [4])

In a conventional chemical rocket engine, the energy source is the oxidizer and the fuel, which are reacted together to release energy. They are transported with the rocket and set the temperature of the combustion reaction (typically 2000 K to 3000 K), which is directly related to the exhaust velocity.

Separating the power source used for propulsion (here, the laser) from the spacecraft itself allows crucial weight savings, either increasing the payload mass fraction or decreasing transit time. Using a laser also allows for much greater thrust chamber temperatures than chemical propulsion, as the temperature of these plasmas is typically 15 000 K to 30 000 K. This gives in turn greater exhaust velocities. This propulsion method could therefore be an order of magnitude more efficient than our current rocket engines if certain engineering problems can be solved.

Increasing the amount of energy deposited by the laser into the propellant remains a topic of active research and is a significant hurdle for the operational use of LTP. The two main conversion efficiencies are:

1. Absorption of the laser energy by the plasma
2. Heat transfer from the plasma to the propellant

A selection of past LSP experiments will now be presented, with an emphasis on these efficiencies. As the efficiencies chosen are different from source to source, they will be defined where applicable.

1.2 Literature review

The experimental basis of LTP was developed by Generalov *et al.* [5] in 1970. For the first time, an LSP was generated with a 150 W CO₂ laser operating at a 10.6 μm wavelength. In this case, the LSP was initiated by a second, 10 kW pulsed CO₂ laser.

Work was done in the mid-1970s by Shoji [6] and Shoji and Larson [7] to design a small-scale 10 kW and full-scale 5000 kW LTP engine. Carbon-seeded hydrogen was chosen to capture the plasma's radiation, which was mostly in the UV wavelength. 20 % of the laser power would be lost by convection and radiation to the walls in the 10 kW thruster, with an additional 5 % of laser power lost by radiation through the thruster window. However, these engines were not tested. The 10 kW prototype (??) was built and delivered to NASA at the conclusion of their effort.

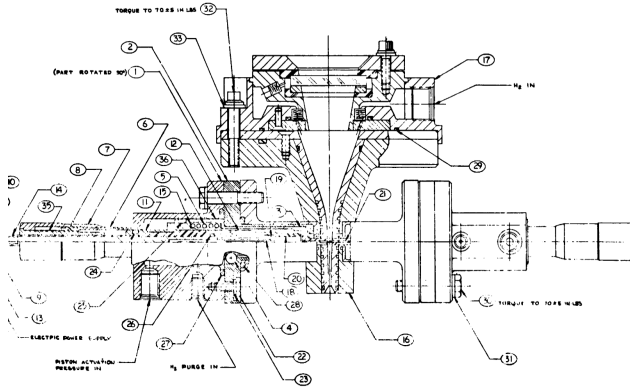


Figure 1.3: Cross-section drawing of 10 kW thruster from Shoji [6] (original is of poor quality)

In the 1980s, Keefer *et al.* [8] studied LSP in a forced convective flow environment. Using a 1.5 kW CO₂ laser with power levels of 360 W to 840 W and pressures of 1.3 atm to 2.3 atm, with varying argon flow velocities, the temperature field of the plasma was measured. From the temperature field, and assuming local thermodynamic equilibrium, the power absorbed

by the plasma and the power radiated from it can be calculated. [Figure 1.4](#) shows the ap-

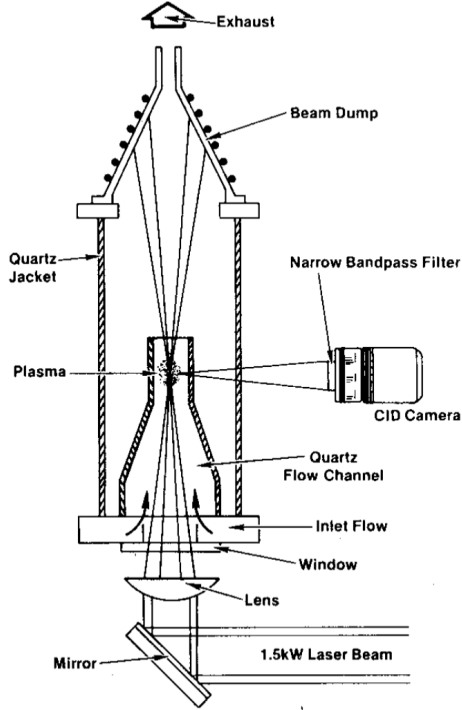


Figure 1.4: Experimental apparatus from Keefer *et al.* [8]

paratus used for these measurements. An inner quartz flow channel contained the plasma, while an outer quartz jacket contained the pressure. The plasma was initiated by laser heating of a tungsten rod, which was removed after initiation. Downstream, a water-cooled copper beam dump absorbed the energy of the laser and the heated argon flow, but was not used for measurements. The plasma's temperature was obtained through analyzing digital images. This temperature field was then used to calculate the power absorption and the radiation loss. The power absorbed by the plasma was between 23 % to 61 % of incident laser power, while radiation loss was between 51 % to 80 % of the absorbed power.

Contemporary to Keefer *et al.* [8], Mazumder and Krier headed a group at the University of Illinois that advanced the field of LTP. Krier *et al.* [9] reported laser absorption in an argon plasma approaching 80 %. [Figure 1.5](#) shows the apparatus that was used by Krier *et al.* [9], Zerkle *et al.* [10] and Chen and Mazumder [11]. This vertical cylindrical flow chamber was made of 304 steel and had an internal diameter of 5 inches. A water-cooled calorimeter was used as a beam dump for the 10 kW CO₂ laser. The laser energy not collected by the beam dump was assumed to be absorbed by the plasma, as the radiation reflected off the plasma is less than 2 % at these electron number densities. Moveable thermocouples gave two-dimensional maps of the flow surrounding the plasma core. The direct laser heating

of the thermocouples and their carriage was taken into account. These two-dimensional

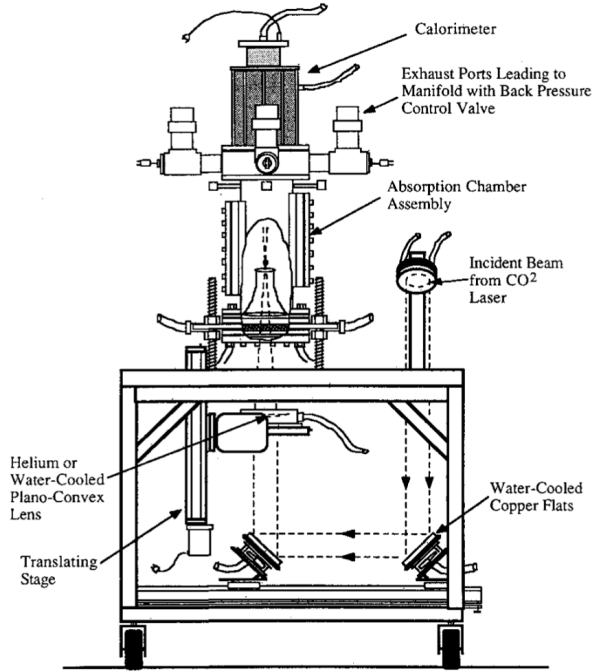


Figure 1.5: Experimental apparatus from Zerkle *et al.* [10]

temperature maps. Thermal efficiency was between 6 % to 25 %, with radiative losses of 64 % and 30 %, respectively. Thermal efficiency was defined as:

$$\eta_{\text{th}} = \frac{\text{Power retained by the gas}}{\text{Incident laser power}}$$

The minimum maintenance intensity of the plasma was also estimated at 0.1 MW/cm^2 to 0.3 MW/cm^2 .

Further work by Zerkle *et al.* [10] with the apparatus shown in Figure 1.5 reported absorption from 55 % to 97 % and thermal efficiency from 11 % to 46 %. This was done in 12.5 atm of flowing argon, with laser powers up to 7 kW. Chen and Mazumder [11] again increased the thermal efficiency of this apparatus, with 41 % to 62 % of the laser energy being retained by the gas as thermal energy. This was among the highest thermal efficiencies measured by an LSP experiment. Here, 86 % of the laser's energy is absorbed by the LSP. This was attained with a 5 kW CO_2 laser, with flow speeds between 2 m/s to 10 m/s. They discuss that greater thermal efficiency is due to greater laser power, a high enough flow speed and a greater laser focusing f number.

Based on work by the Illinois group, an LTP engine demonstrator was tested in 1995 by

INSERT EX-
PLANATION
HERE

Black *et al.* [12] with a 10 kW CO₂ laser. This was planned to be a step towards a full-scale thruster. More than 100 thruster firings were completed, lasting 1 to 2 minutes each. The 10 kW thruster is presented in Figure 1.6a. It is mounted in a vacuum chamber to a thrust measurement assembly. Efficiency was calculated from:

$$\eta = \frac{F^2}{2\dot{m}P_L}$$

with P_L the input laser power at the thruster window. Both argon and hydrogen were used. Argon propellant produced 200 s of I_{sp} and a peak efficiency of 0.24. With hydrogen propellant, an I_{sp} of 350 s and a peak efficiency of 0.37 were reported. A preliminary design

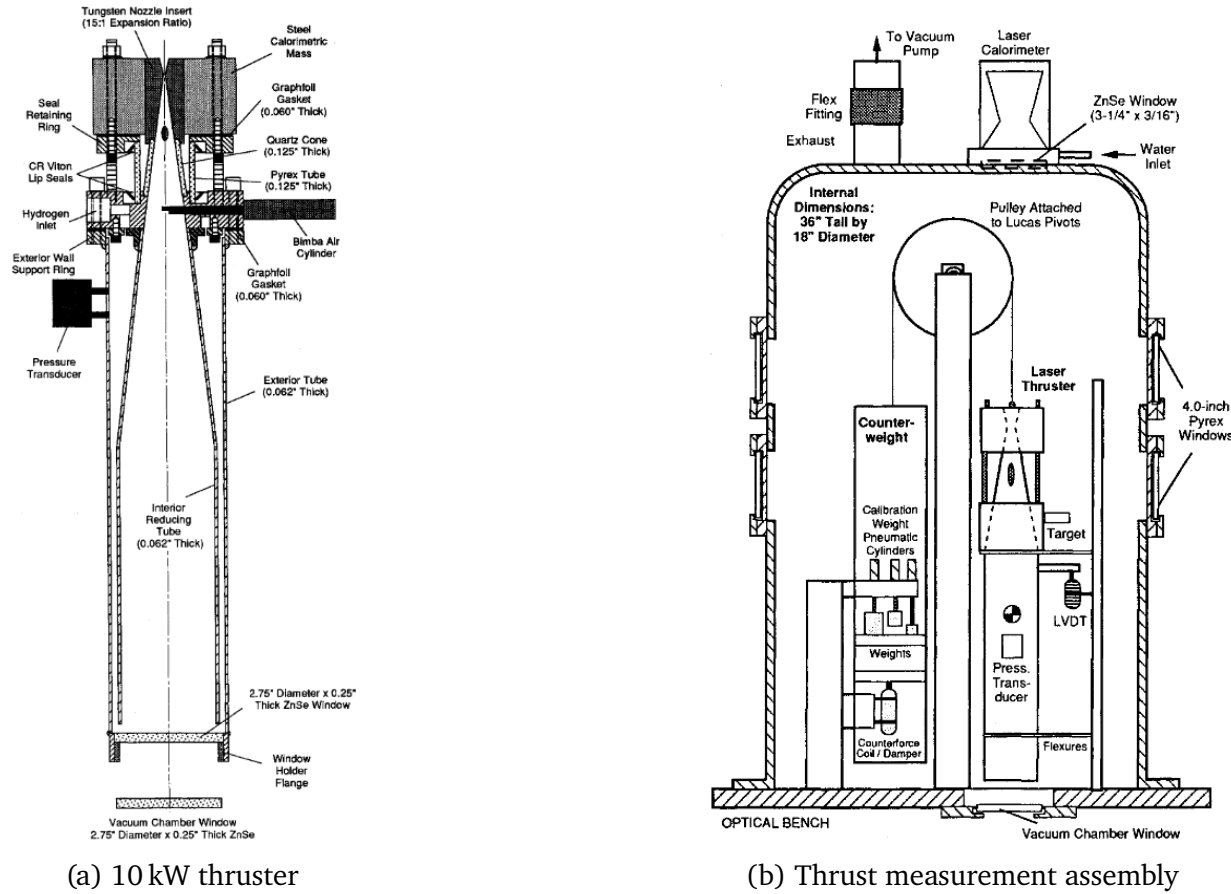


Figure 1.6: Apparatus used in Black *et al.* [12]

for the full-scale 100 kW thruster was also presented, with a predicted specific impulse of 1000 s, thrust of 4.5 N and a conversion efficiency of 80 %.

In the early 2000s, Toyoda *et al.* [13] built and tested two different thruster models, presented in Figure 1.7. These thrusters, using argon or nitrogen heated by LSP, were powered

by a 2 kW CO₂ laser. The LSPs were initiated by a retractable tungsten rod at the laser's focus. Thrust measurements were done both in atmospheric pressure and in vacuum. This comparative study showed that confining the plasma into a smaller chamber increased heat transfer and therefore, efficiency. Toyoda *et al.* [13] defined the energy conversion efficiency as the amount of laser power that is converted into usable kinetic energy for thrust. It is calculated as¹:

$$\eta_e = \frac{F_{\text{hot}}^2 - F_{\text{cold}}^2}{2\dot{m}P}$$

Where F_{hot} is the thrust with laser on, F_{cold} is the cold flow thrust (laser off) and P is incident laser power. An energy conversion efficiency of 37% and an I_{sp} of 113 s were measured with the second model Figure 1.7b in vacuum with argon propellant. The pressure ratio, defined as the chamber pressure divided by the nozzle exit pressure, was 420. A water cooling system measured the heat loss to the walls to be 55% of incident laser power, with a final 8% being “other loss”. Heat loss to the walls was expected to be recycled with regenerative cooling in a real-world application.

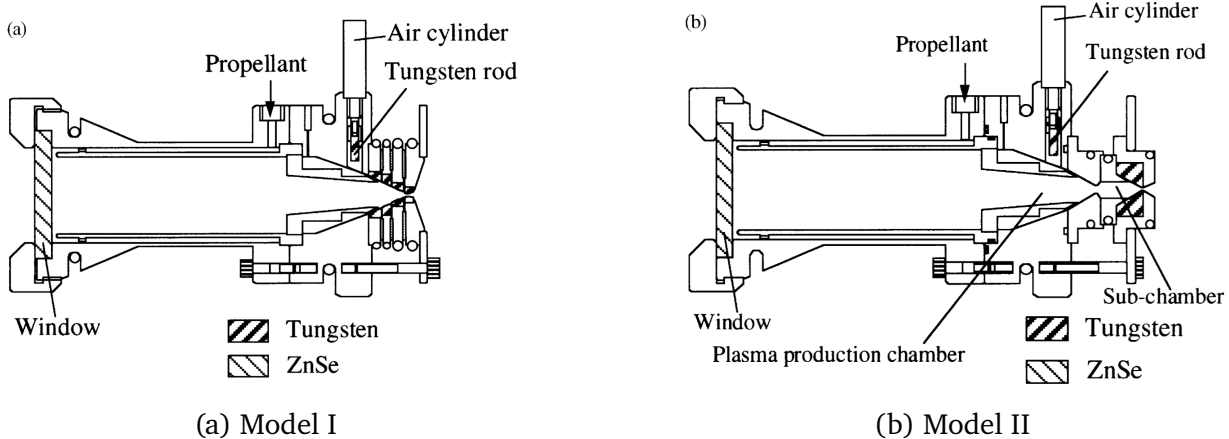


Figure 1.7: Two thruster models from Toyoda *et al.* [13]

Lu *et al.* [14] investigated LSP for lighting applications instead of propulsion. Therefore, an emphasis was made on spectroscopy measurements. A 300 W fiber laser at a wavelength of 1080 nm was focused to a 50 μm diameter spot in a high pressure chamber. Argon was used, with pressures between 10 bar to 20 bar. A lower initiation power (117 W) than other studies was achieved at 20 bar. This was attributed to the smaller focus delivering a greater photon flux. N₂ was later added between 0.1 % to 1.0 %. As expected, increasing the laser power or the gas pressure was found to increase the radiation intensity of the LSP. However,

¹As mentioned by Duplay [4], there appears to be a typographical error in the reference as the units are inconsistent. The corrected equation is presented here.

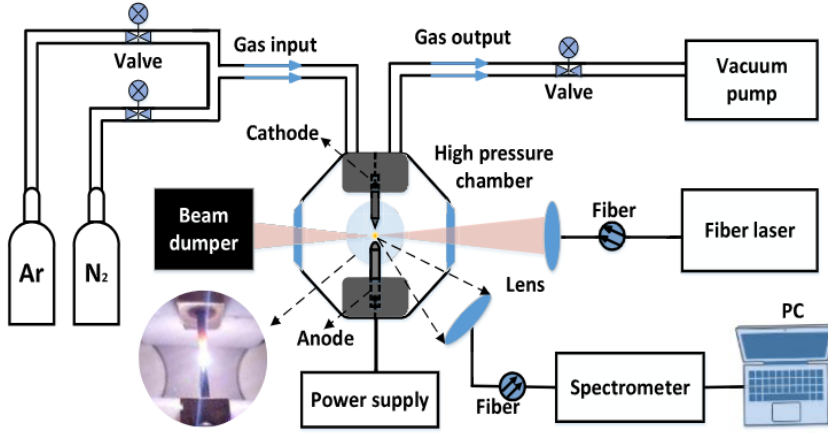


Figure 1.8: Experimental setup from Lu *et al.* [14]

adding N₂ reduced both the electron temperature and electron density of the LSP, reducing its radiation intensity.

Seeding the propellant with another species has been discussed as a way to increase the energy absorption into the working fluid of an LTP engine. LSPs in pure methane and methane-seeded gasses have been investigated by Kamei *et al.* [15]. Methane dissociates into hydrogen and carbon with the high temperature of the LSP. As mentioned with Shoji [6], carbon particles would absorb the LSP's UV radiation. A 1.1 kW diode laser at a wavelength of 940 nm was beamed into a high-pressure chamber fitted with arc initiation electrodes. The gap between these electrodes was 1 mm. A CCD type spectrometer recorded emission spectra of the initiation arc discharge and of the LSP. LSPs in three different gasses were attempted: pure methane, methane-argon, and methane-xenon.

In methane at 0.1 MPa, soot formation between the electrodes prevented LSP initiation. The spectrometer confirmed the dissociation of methane, as line spectra of carbon and hydrogen were observed at the initiation arc. Initiation was also unsuccessful in argon-methane with a pressure between 0.1 MPa to 0.3 MPa and a methane volume fraction between 20 % to 60 %. LSP was successfully generated in methane-xenon, with a lower threshold power (850 W) than in pure xenon. The partial pressure of methane was between 0.02 MPa to 0.6 MPa, with a partial pressure of xenon of 0.10 MPa.

Takano *et al.* [16] used a diode laser emitting simultaneously at 927 nm and 951 nm to generate LSPs in argon. This resulted in an I_{sp} of 105 s and a thrust efficiency of 8 %. This I_{sp} was calculated from the plenum pressure when the laser was on. They define thrust

efficiency as:

$$\eta = \frac{g_0 I_{\text{sp}} (F_{\text{hot}} - F_{\text{cold}})}{2P_{\text{laser}}}$$

Two setups were used: the LSP generation chamber previously used by Kamei *et al.* [15] (Figure 1.9a) and an LSP thruster (Figure 1.9b). The LSP chamber was used to determine

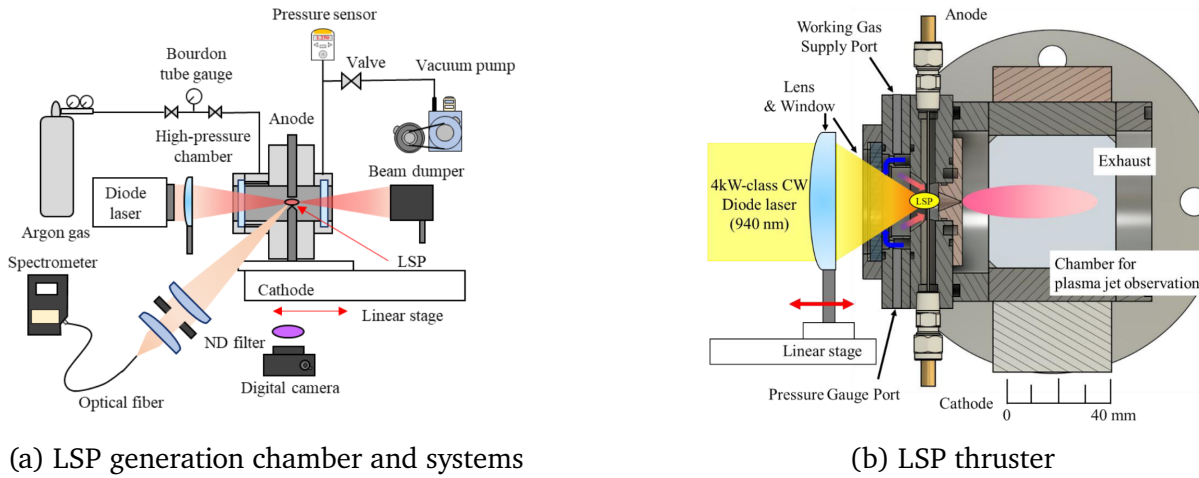


Figure 1.9: LSP setups from Takano *et al.* [16]

the effect of various F-numbers on the argon LSP. The thruster has an interchangeable copper throat, with diameters of 0.7 mm and 1.0 mm. In both setups, electric arc initiation was used. Once initiated in the thruster, the LSP is moved toward the nozzle with the lens mounted on a motorized stage. It was found that moving the LSP this way increased the heat exchange with the propellant. Thrust was calculated by using the pressure measurements inside the thruster's heating chamber.

Duplay [4] used a 3 kW pulsed fiber laser to create LSPs in static and flowing argon. In static argon, about 80 % of the laser energy was being absorbed by the plasma, with approximately 15 % of the laser energy heating the bulk gas. This was done between 5 bar to 20 bar.

1.3 Summary and direction of work in this thesis

From the literature review, Table 1.1 and Table 1.2 were compiled. Most studies have used CO₂ lasers with a wavelength of 10.6 μm. Use of a CO₂ laser for power beaming to a remote target for propulsion applications is limited by the range over which the laser can be focused due to their long laser wavelength.

Indeed, the diffraction limit of a laser, which is the theoretical lower limit on beam divergence, equals the wavelength (λ) divided by the diameter D of the output beam [17].

$$\text{Diffraction limit (radians)} = \lambda/D$$

Prof. Higgins comment: Would be better to explain the range over which a laser can be focused.

This relegated CO₂ lasers to ground-to-orbit launch. However, high power fiber lasers emitting near 1 μm have recently become readily available. Being able to beam energy to low earth orbit, fiber lasers make laser propulsion more feasible.

To increase thermal efficiency, Chen and Mazumder [11] suggest:

1. A greater laser power, which gives greater inverse bremsstrahlung absorption coefficient and longer absorption path length;
2. A high enough flow speed to push the LSP back to the laser focus, but not too fast as to blow the plasma out;
3. A greater laser focusing f number, creating a longer and narrower plasma. This increases the probability a photon from the laser will be absorbed by the plasma and reduces the radiation loss.

For a small-scale, demonstration thruster, I_{sp} values near 100 s can be expected, with thrust values under 1 N, as was found by Toyoda *et al.* [13] and Takano *et al.* [16].

The objective of this research project will be to test a Version 1 (V1) lab-scale LTP thruster for interplanetary space flight, as well as design and test an improved Version 2 (V2) thruster. These will be both powered by a 1.07 μm fiber laser. This project will mainly build upon the experimental research started by Duplay [4] with the V1 thruster.

Before going into experiments, it is important to characterize certain thermodynamic properties of the gasses used. Notably, the modelling of heat capacity will be presented in the next chapter.

Table 1.1: Summary of a selection of past LSP experiments. λ : wavelength, P : maximum laser power, p : pressure, \dot{m} : mass flow rate, I_{sp} : maximum specific impulse, F_T : maximum thrust

LSP Facility	Year	Laser	λ [μm]	P [kW]	Gas	p [atm]	\dot{m} [g/s]	I_{sp} [s]	F_T [N]
Generalov <i>et al.</i> [5]	1970	CO ₂	10.60	0.15	Xe	3.0-4.0	-	-	-
Keefer <i>et al.</i> [8]	1986	CO ₂	10.60	0.84	Ar	1.3-2.3	0.01-0.19	-	-
Krier <i>et al.</i> [9]	1986	CO ₂	10.60	10	Ar	-	2.3-4.6	-	-
Zerkle <i>et al.</i> [10]	1988	CO ₂	10.60	7	Ar	-	-	-	-
Chen and Mazumder [11]	1989	CO ₂	10.60	5	Ar	-	-	-	-
Black <i>et al.</i> [12]	1995	CO ₂	10.60	10	Ar	1.4-2.4	5.1-9.4	200	7
Toyoda <i>et al.</i> [13]	2002	CO ₂	10.60	10	H ₂	3.4	1.1	350	3
		CO ₂	10.60	2	Ar, N ₂	2.0-5.5	-	113	0.44
Lu <i>et al.</i> [14]	2022	Fiber	1.08	0.30	Ar, N ₂	9.9-19.7	-	-	-
Takano <i>et al.</i> [16]	2024	Diode	0.927 and 0.951	4.4	Ar	10-15	-	105	-
Duplay [4]	2024	Fiber	1.07	3	Ar	5-20	0	-	-

Table 1.2: Comparative table of experimental LTP thruster efficiencies

LSP Facility	Laser absorption	Efficiency	Value of efficiency
Keefer <i>et al.</i> [8]	0.23 - 0.61	-	-
Krier <i>et al.</i> [9]	0.50 - 0.80	$\eta_{\text{th}} = \frac{\text{Power retained by the gas}}{\text{Incident laser power}}$	0.06 - 0.25
Zerkle <i>et al.</i> [10]	0.55 - 0.97	$\eta_{\text{th}} = \frac{\text{Power retained by the gas}}{\text{Incident laser power}}$	0.11 - 0.46
Chen and Mazumder [11]	0.86	$\eta_{\text{th}} = \frac{\text{Power retained by the gas}}{\text{Incident laser power}}$	0.41-0.62
Black <i>et al.</i> [12]	-	$\eta = \frac{F_{\text{hot}}^2}{2\dot{m}P_{\text{L}}}$	0.20 - 0.25 (Ar), 0.25 - 0.40 (H)
Toyoda <i>et al.</i> [13]	-	$\eta_e = \frac{F_{\text{hot}}^2 - F_{\text{cold}}^2}{2\dot{m}P}$	0.37
Takano <i>et al.</i> [16]	-	$\eta = \frac{g_0 I_{\text{sp}} (F_{\text{hot}} - F_{\text{cold}})}{2P_{\text{laser}}}$	0.08
Duplay [4]	0.80	$\eta_{\text{th}} = \frac{\text{Power retained by the gas}}{\text{Incident laser power}}$	0.15

Chapter 2

Modelling heat capacity

Gabriel's comment: The original goal was to have a 0D model of the LTP thruster that could be compared to experiments. Prof. Higgins wanted an experimental line and a theory line on a graph that were somewhat on top of each other. Given that we received the V2 experiment parts to be setup at the end of April, I concentrated my efforts on getting the thruster running so we could get experimental data. Due to reasons explored in the discussion chapter, more parts had to be made for the V2 experiment to work. I ended up without experimental data and without this model completed. This is the reason Prof. Higgins dismissed my thesis in August, and I attempted a re-scoping of the work toward designing and commissioning the V2 thruster. I will have to change the justification of why this chapter was written if I keep it.

To correctly predict the temperature increase of the gas that should be expected when laser energy is input, the heat capacity of argon and hydrogen was modelled. Argon is the current gas used in experiments, as it is economical and easy to ionize. Hydrogen is projected to be used in the full-scale LTP engine for its increased I_{sp} due to having lower molecular weight.

2.1 Equilibrium calculations

The following seventh order polynomials and their coefficients (a_1 to a_7 , b_1 , and b_2), from McBride *et al.* [18], were implemented in Python. Species of interest were H, H₂, Ar, Ar⁺, and electrons e⁻. Plasma temperatures studied allowed us to treat the argon as singly ionized. The heat capacity at constant pressure, as well as the temperature (T) dependent part of enthalpy and entropy of each species are given by C_p^0 , H^0 and S^0 , respectively. \bar{R} is

the universal gas constant.

$$C_p^0(T)/\bar{R} = a_1 T^{-2} + a_2 T^{-1} + a_3 + a_4 T + a_5 T^2 + a_6 T^3 + a_7 T^4 \quad (2.1)$$

$$H^0(T)/\bar{R}T = -a_1 T^{-2} + a_2 \ln(T)/T + a_3 + a_4 T/2 + a_5 T^2/3 + a_6 T^3/4 + a_7 T^4/5 + b_1/T \quad (2.2)$$

$$S^0(T)/\bar{R} = -a_1 T^{-2}/2 - a_2 T^{-1} + a_3 \ln(T) + a_4 T + a_5 T^2/2 + a_6 T^3/3 + a_7 T^4/4 + b_2 \quad (2.3)$$

Next, the functions for entropy \bar{s}_i of each species i and Gibbs energy \bar{g}_i , both per kmol, were implemented. These values depend on temperature T and partial pressure p_i . y_i is the molar fraction of the species, and p_{ref} is the reference pressure, equal to 1 bar.

$$\bar{s}_i(T, p_i) = \bar{s}_i^0(T) - \bar{R} \ln \frac{y_i p}{p_{ref}} \quad (2.4)$$

$$\bar{g} = \bar{h} - T\bar{s} \quad (2.5)$$

Considering the number of moles n_i , expressions of the Gibbs energy of the two mixtures $G_{mixture}$ are found:

Starting with 1 kmol argon,

$$G_{mixture, Ar}(T, p) = n_{Ar} \bar{g}_{Ar}(T, p_{Ar}) + n_{Ar+} \bar{g}_{Ar+}(T, p_{Ar+}) + n_e \bar{g}_e(T, p_e) \quad (2.6)$$

Starting with 1 kmol hydrogen,

$$G_{mixture, H_2}(T, p) = n_H \bar{g}_H(T, p_H) + n_{H2} \bar{g}_{H2}(T, p_{H2}) \quad (2.7)$$

Plotting the Gibbs energy of the hydrogen mixture as a function of its degree of dissociation x , for different total pressures p :

A similar dissociation graph can be found with argon, but with three species. The Gibbs energy is then minimized to determine the molar fractions y_i at which the mixture reaches

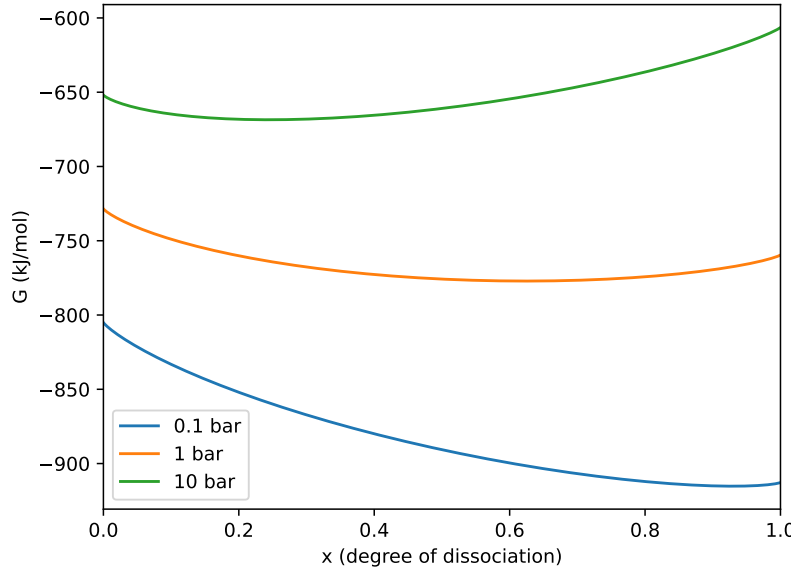


Figure 2.1: Gibbs free energy (G) plotted against the degree of dissociation of hydrogen under three different pressures

equilibrium. From this, the enthalpy H of the mixture was found. The C_p of the mixture was then calculated from the enthalpy with:

$$C_p = \frac{\partial H}{\partial T} \quad (2.8)$$

For argon, these calculated C_p values were validated against values from CEA [19].

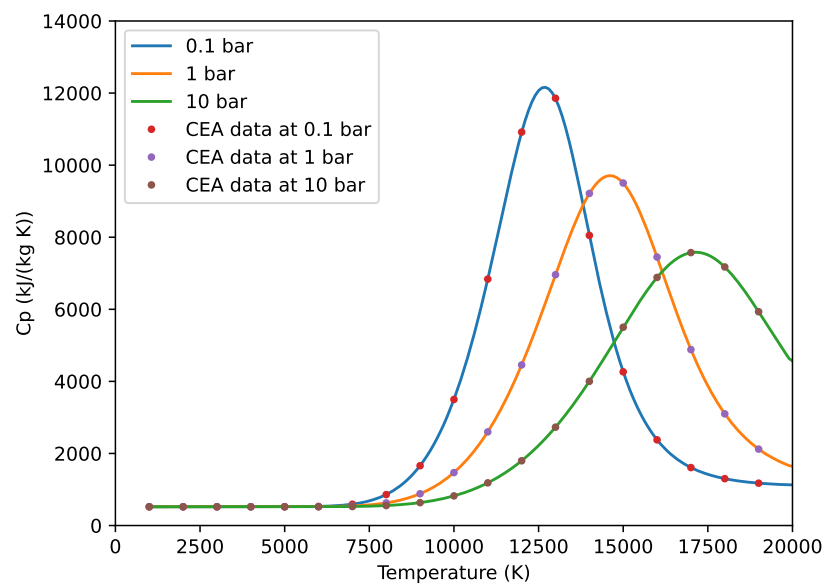


Figure 2.2: Comparing calculated C_p values of argon to those from CEA

Chapter 3

Facility design

3.1 Version 1 test section

The design process of the first generation thruster, called Version 1 (V1, see [Figure 3.1](#)), can be found in Duplay [4]. It proved to be a dependable prototype, repurposed from a previous unrelated experiment. However, it presented problems that required a second generation prototype to be designed and manufactured.

298 recorded pulsed laser shots were conducted with V1, exploring the power-pressure threshold, wire initiation and spark initiation. A side window permitted direct visualization of the LSP with a high speed camera (Photron Fastcam SA5).

3.2 Version 2

To improve upon the V1 facility, an entire LTP thruster redesign was done. This resulted in the much smaller Version 2 (V2) purpose-built LTP thruster at the end of April 2024, seen in [Figure 3.2](#).

3.2.1 Requirements

The following requirements were developed for the design of the V2 thruster. The objective was to detect a measurable difference in thrust between an argon cold gas thruster and an argon “hot gas” thruster, heated by a laser supported plasma (LSP).

1. Laser thruster

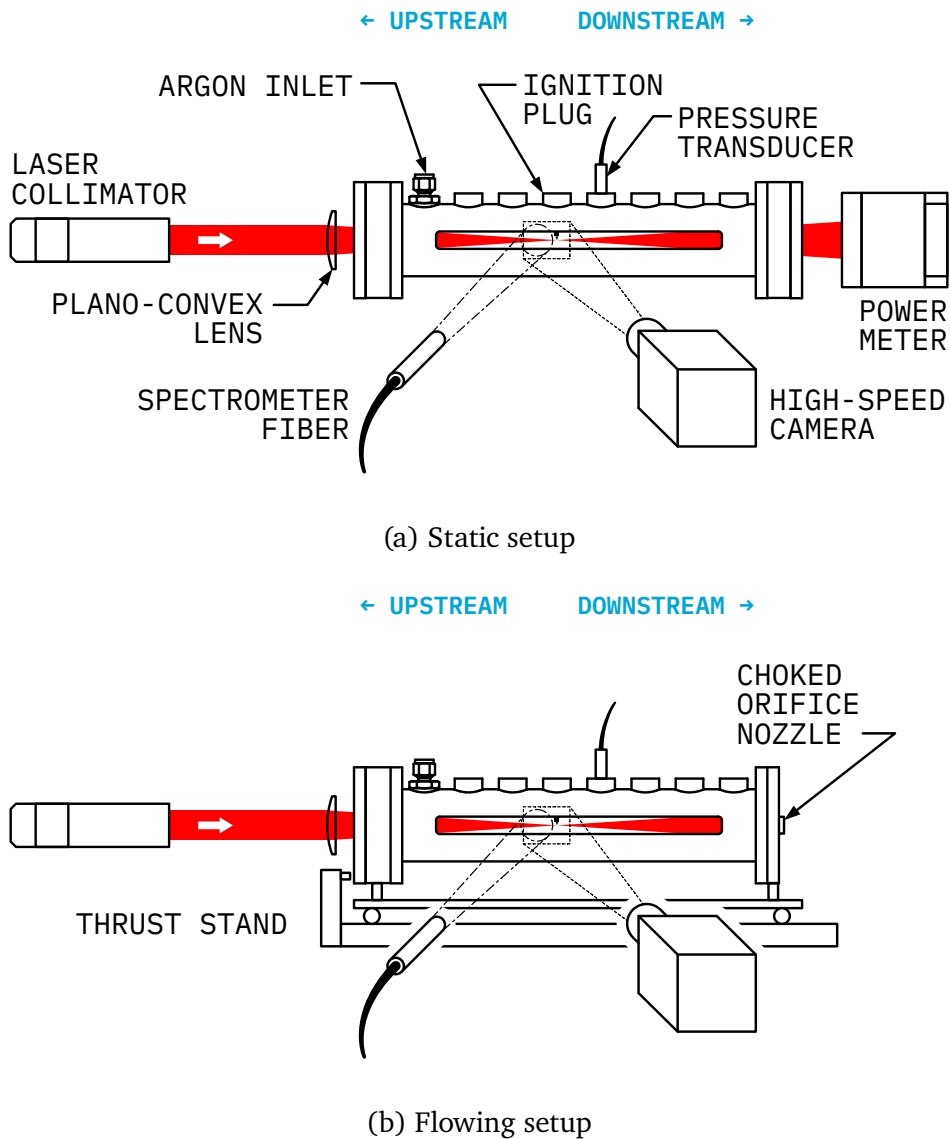
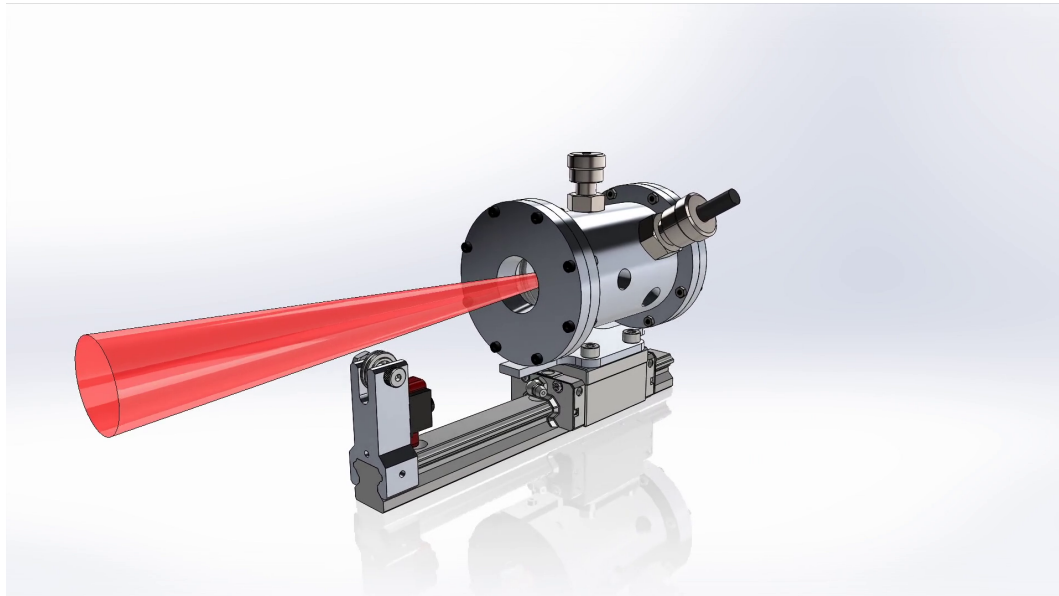
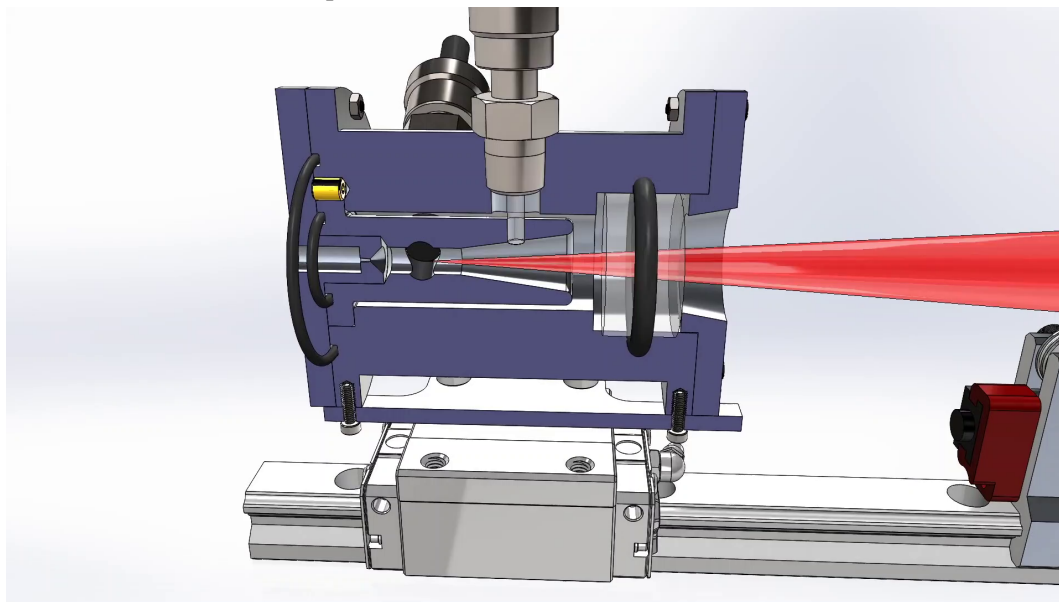


Figure 3.1: V1 LTP thruster from Duplay [4]

- (a) A 300 W Continuous Wave (CW) 1070 nm laser shall sustain the plasma (Nominal power 300 W, actual max power 350 W)
- (b) The thruster shall have a minimum safe “hot” operation time of 30 s
 - i. In the event of failed LSP initiation, the thruster shall safely absorb the total laser power for at least 10 s
- (c) An optical path shall be present to let the laser into the thruster, utilizing a 100 mm focal length lens at minimum and a collimated beam with a maximum diameter of 30 mm



(a) View of the laser path (in red) and thruster mounted on its thrust stand



(b) Cutaway view of the inside of the thruster

Figure 3.2: Render of the V2 LTP thruster

- i. The optical components shall not be damaged by the laser flux
- (d) Argon shall be used as the working fluid
 - i. The argon feed gas shall be at room temperature
- (e) A gas feed path shall bring argon gas into the thruster
 - i. The gas feed shall be choked at the thruster inlet

- ii. The gas feed shall be evenly distributed in the thruster
 - (f) The mass flow rate of the argon gas shall be measured and controlled by interchangeable upstream choked orifices
 - (g) The maximum allowable operating pressure (MAOP) of the thruster shall be 50 bar
 - i. The nominal pressure of the thruster shall be 25 bar
 - (h) A converging-diverging exhaust nozzle shall be designed to accelerate the gas to a supersonic speed
 - i. The nozzle shall be easily changeable
 - (i) A 1/8" NPT port for a pressure transducer shall be present along the thruster
 - (j) An optical port shall be present for spectrometry measurements of the plasma
 - (k) The thruster shall be installed on a thrust stand (See section 3. Thrust stand)
2. Initiation system/electrical
- (a) The LSP shall be initiated by an electrical spark
 - (b) The spark gap shall be measurable, controllable, and repeatable
 - (c) The spark shall be generated by an AEM 30-2853 High Output Smart Coil, supplying 41 kV with up to 118 mJ
 - (d) All parts of the thruster and thrust stand shall be directly or indirectly connected to a common electrical ground
3. Thrust stand
- (a) The thrust stand shall measure thrust on the order of 0.1 N to 5 N
 - (b) The thrust stand shall minimize friction losses
 - (c) The thrust stand shall be securely fixed using standard optical breadboard mounting hardware

With these requirements, preliminary geometric dimensions of the V2 thruster could commence. It was expected to be much smaller than V1, as the goal was to isolate the LSP region and increase heat flux to the gas.

3.2.2 Initial sizing of the double choked LTP thruster

When adding energy to the thruster chamber with a laser, it is useful to choke the inflow upstream of the chamber. Indeed, this keeps the P_0 and \dot{m}_{in} constant, so the increase in chamber pressure can be interpreted as a measure of energy deposition. The second choke happens at the nozzle to accelerate the hot gas to a supersonic speed. Therefore, this configuration is double choked (see [Figure 3.3](#)), a classic problem in compressible fluid mechanics.

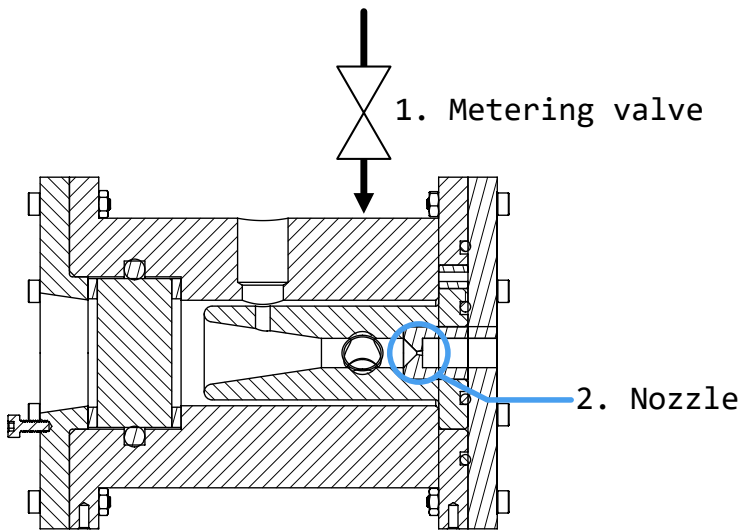


Figure 3.3: Cutaway of a double choked LTP thruster showing both choking orifices: the metering valve and the nozzle.

The starting assumptions were the following: a 300 W power input (the laser) supplies energy to an LTP experiment that has an internal pressure of 25 bar, with a 50 bar feed pressure. It is required that the hot gas operation (laser on) increases the gas' exit velocity to twice that of the cold gas operation (laser off). We will determine the gas mass flow rate and the diameter of the two orifices needed to choke the flow.

Starting with a cold gas thruster using argon, the speed of sound of argon (c_0) is 323 m/s. This is at ambient temperature (300 K), as we have no laser energy to heat the gas in this case. With a nozzle, the gas is accelerated to approximately twice this speed. The v_{exit} , which is our main performance parameter, is therefore 646 m/s.

Laser on (hot) operation will now be examined. Taking the previous v_{exit} and ionizing the whole flow, it is supposed that our efficiency is doubled. This gives a $v_{exit} \approx 1300$ m/s. What nozzle throat size is therefore necessary for this \dot{m} with $p_{chamber} = 25$ bar? We know

that $MW_{Ar} = 40 \text{ g/mol}$. The speed of sound is $c = \sqrt{\gamma RT}$. As we want to double the speed of sound, we are multiplying the temperature by 4.

$$\text{Power} = \dot{m}(h_2 - h_1) = \dot{m}c_p(T_2 - T_1)$$

Using a constant c_p of argon of $0.520 \text{ kJ kg}^{-1} \text{ K}^{-1}$, the calculated \dot{m} is 0.641 g/s .

Fliegner's formula describes the mass flow rate of an isentropic flow:

$$\frac{\dot{m}}{A} = p_0 \sqrt{\frac{\gamma}{T_0 R}} \frac{M}{(1 + \frac{\gamma-1}{2} M^2)^{\frac{\gamma+1}{2(\gamma-1)}}}$$

With $\gamma = \frac{c_p}{c_v} = 1.666$ for argon and choked flow at the nozzle, the area and the diameter of the circular nozzle are 0.176 mm^2 and 0.473 mm , respectively. These calculations can be repeated for the feed orifice, with the same \dot{m} , a pressure of 50 bar and ambient temperature. This gives us an orifice diameter of about 0.2 mm.

3.2.3 Test section and thrust stand

As can be seen in [Figure 3.4](#), the V2 test section was designed with multiple ports for modularity, enabling static and flowing tests with argon propellant. Ports that were not in use were fitted with pipe plugs. In all tests, the two opposing electrode ports and one argon inlet port were used. The second argon inlet, intended to offer a more uniform flow if needed, was not used. The optical access port was initially fitted with a quartz rod in an Ultra-Torr fitting. After flowing through the test section, used argon propellant was vented directly to the lab. [Figure 3.5](#) shows the two final configurations in the lab.

The thrust stand is a ball bearing carriage (McMaster-Carr 6709K12) mounted on a 15 mm wide, 160 mm long guide rail (McMaster-Carr 6709K33). It is mounted on the optical breadboard using acrylic spacers. A string through a pulley holds a variable weight, adding a preload to the test section. This ensures adequate contact between the test section and the load cell, and allows calibration of the load cell. Two load cells are used with different force sensing range: Honeywell FSG020WNPB (0 N to 20 N) and Honeywell FSG005WNPB (0 N to 5 N).

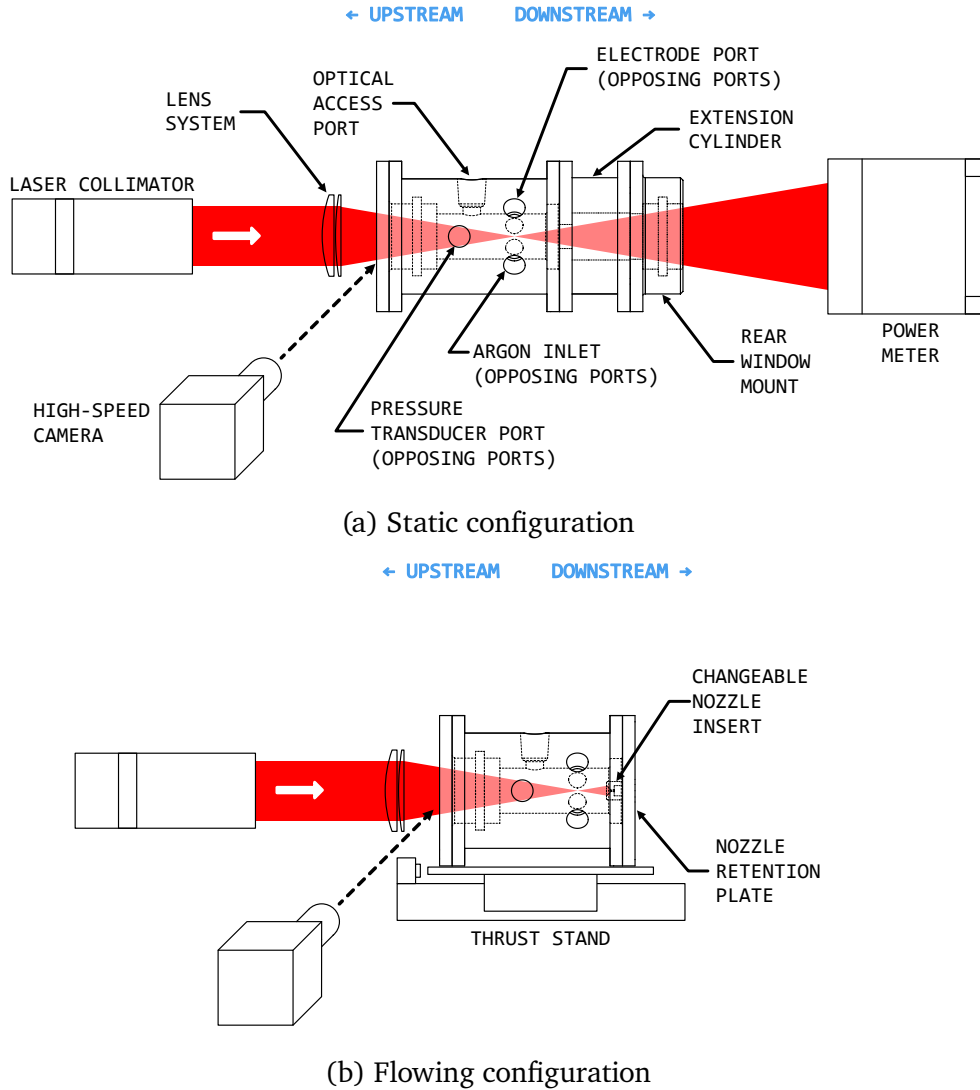
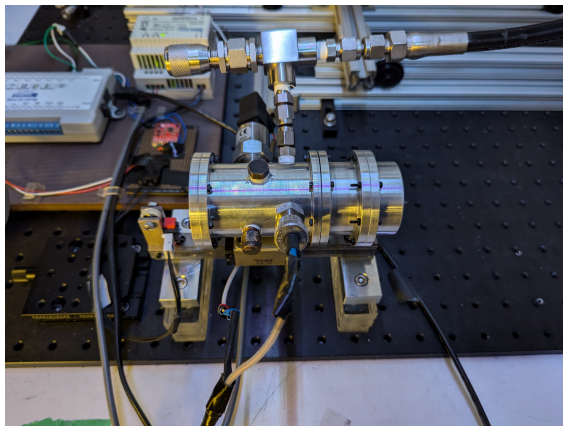


Figure 3.4: V2 LTP thruster

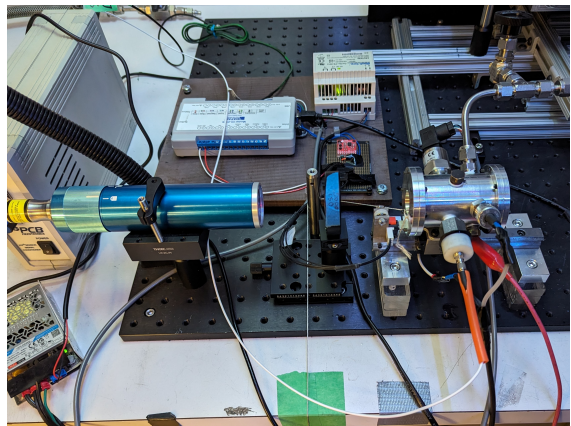
3.2.4 Laser and optics

The laser used as the plasma's power source is an IPG Photonics YLR-300/3000-QCW-MM-AC Ytterbium fiber laser. The wavelength of the emitted light is 1070 nm. Its nominal maximum power is 3 kW quasi-continuous wave (QCW) or 300 W continuous wave (CW). At 3 kW, a QCW pulse has a maximum duration of 10 ms. The maximum duration of a 300 W QCW pulse is 50 ms. The IPG Photonics P30-001736 collimator outputs a 30 mm diameter laser beam. The laser also includes a red visible laser for alignment, which is coaxial to the main beam. These components form the laser system, presented in [Figure 3.6](#).

Calibration reports for the laser and the collimator can be found in [Appendix A](#). The laser



(a) Final static configuration. Note the extension part and window mount. Optics and laser collimator are not pictured here, but would be installed during testing.

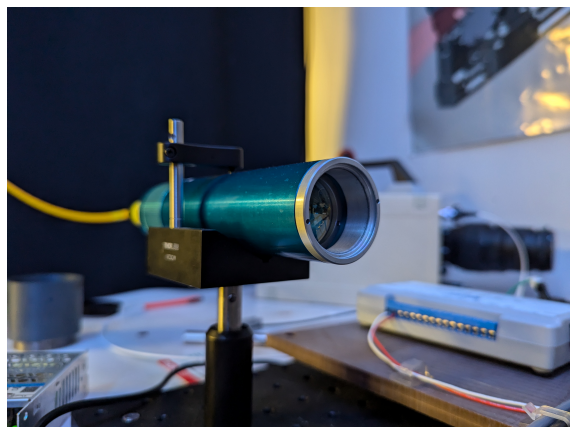


(b) Final flowing configuration. The nozzle is held by the rear plate.

Figure 3.5: V2 LTP thruster



(a) IPG Photonics YLR-300/3000-QCW-MM-AC laser



(b) IPG Photonics P30-001736 collimator

Figure 3.6: Laser system

is mounted at the base of a freestanding electronics rack ([Figure 3.7](#)).

V2 uses two lenses placed close to each other to focus the laser from the collimator. These are the Thorlabs LA1380-C and LA1417-C N-BK7 plano-convex lenses with a 1050 nm to 1700 nm anti-reflective coating. Their focal lengths of 500 mm and 150 mm, respectively, give a combined focal length of 115 mm. These two lenses are mounted in a single Thorlabs LMR2 lens mount with two retaining rings. A Thorlabs DT12 translation stage enables left-right alignment of the laser focus, while a Thorlabs DTS25 translation stage gives control on the depth (axial position) of the focus.

The design
of this lens
system is
discussed in
the experimen-
tal chapter.
Should
it be here?

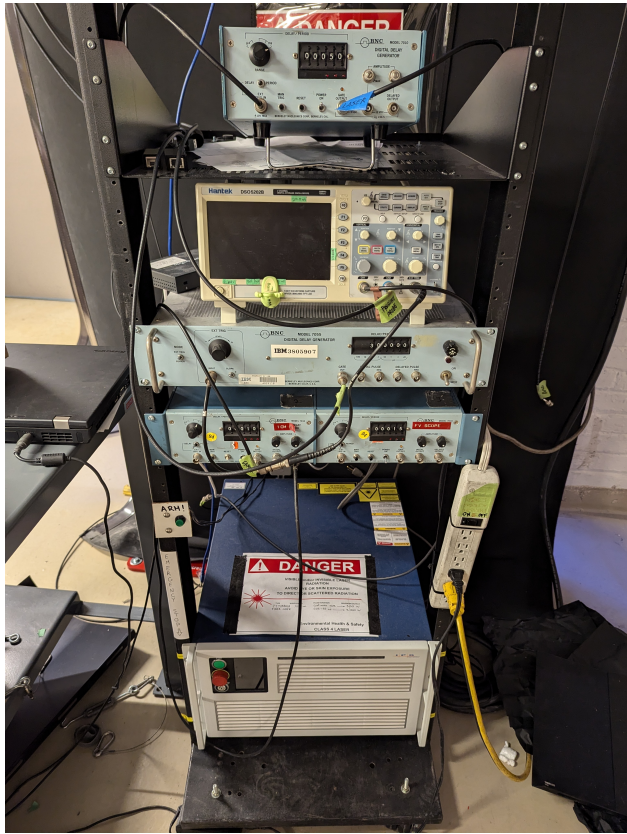


Figure 3.7: Electronics rack with laser at the base

3.2.5 Timing control

Correct timing of the laser and spark initiation is necessary to initiate LSP when the laser is in QCW mode, and to minimize damage to V2's nozzle in CW mode. To this end, delay generators are used (BNC models 7010 and 7055) as seen in [Figure 3.8](#). They are mounted at the top of the electronics rack.

3.2.6 Data acquisition (DAQ) system and oscilloscope

Load cell and pressure transducer voltage is sent to a DATAQ Instruments DI-2018, on [Figure 3.9](#). This data is streamed to a personal computer by USB, where the thrust and pressure traces can be saved for analysis. Two pressure sensors were used: a PCB Model 113B28 and an Omega PX119A-1KG5V. Refer to [Appendix D](#) for the Omega pressure sensor calibration.

[Photos of pressure sensor and PCB assembly]

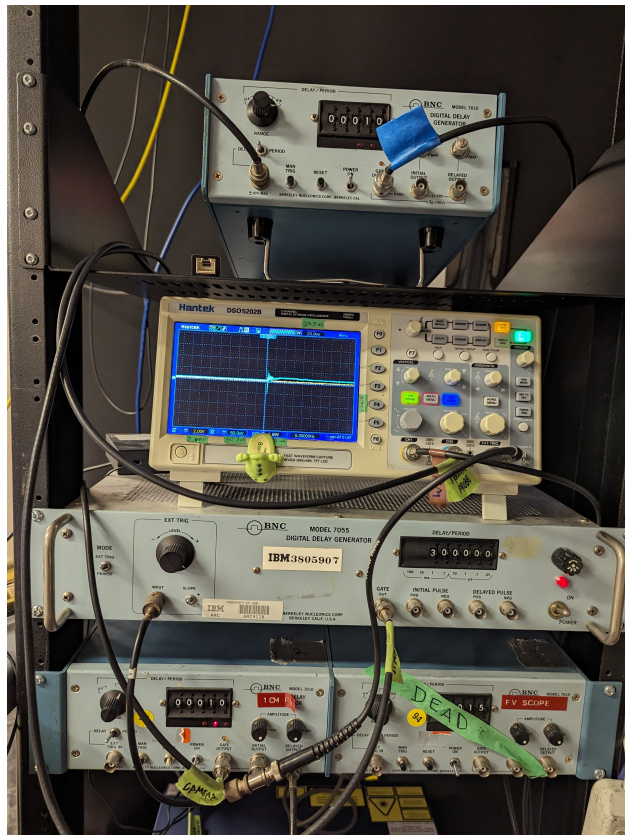


Figure 3.8: Delay generators and oscilloscope

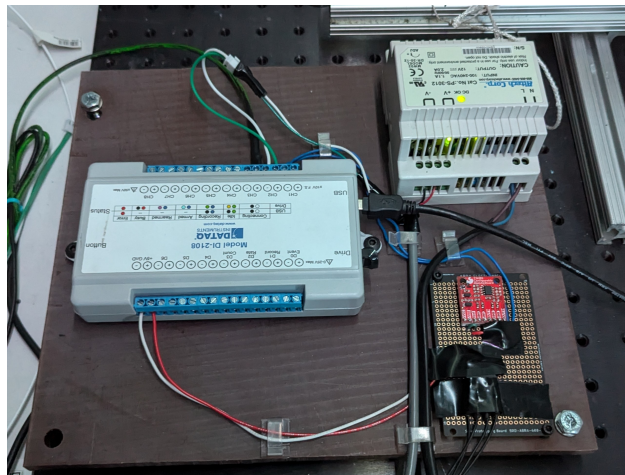


Figure 3.9: DAQ system

3.2.7 Cameras

A Photron SA5 high speed camera was used during certain LSP shots to determine if LSP initiation had happened and how long the plasma had lasted. Due to the fact that no side window was present on V2, the Photron camera looked at an angle from the side into the

front window, seeing the reflection of the plasma core (as in [Figure 3.4](#)). During LSP shots, the camera's sensor was protected by an Aurora PowerXND-II Variable Neutral Density Filter and a Hoya 58 mm UV and IR cut filter.

A generic USB webcam was also connected to the data acquisition laptop, giving a live wide-angle view of the entire experiment. As these cameras are sensitive to IR, it gave an extra confirmation that the laser emission was off before opening the laser safety curtain.

3.2.8 Spark initiation system

The spark was generated by an AEM 30-2853 High Output Smart Coil, supplied by a 10 A power supply. The coil can generate a 40 kV, 103 mJ spark. The trigger signal wire from the delay generator comes in from the left of [Figure 3.10](#). It passes through the power supply electrical box in a quad shielded coaxial cable. The smart coil is placed in a separate electrical box to reduce electromagnetic interference. The spark energy exits through the cable on the right of [Figure 3.10](#).



[Figure 3.10](#): Spark initiation system. On the left is a power supply, while spark coil number 6 is on the right.

[Figure 3.11](#) shows the assembled electrodes, the sharper one being connected to the smart coil's output. The other electrode is grounded.

3.2.9 Needle valve

To be able to run the thruster in the double choked configuration, an adjustable orifice upstream of the thruster is required. The WL14H-320P needle valve ([Figure 3.12](#)) was chosen for this.



Figure 3.11: Assembled electrodes with Ultra-Torr cap and electrical connectors



Figure 3.12: WL14H-320P Needle valve

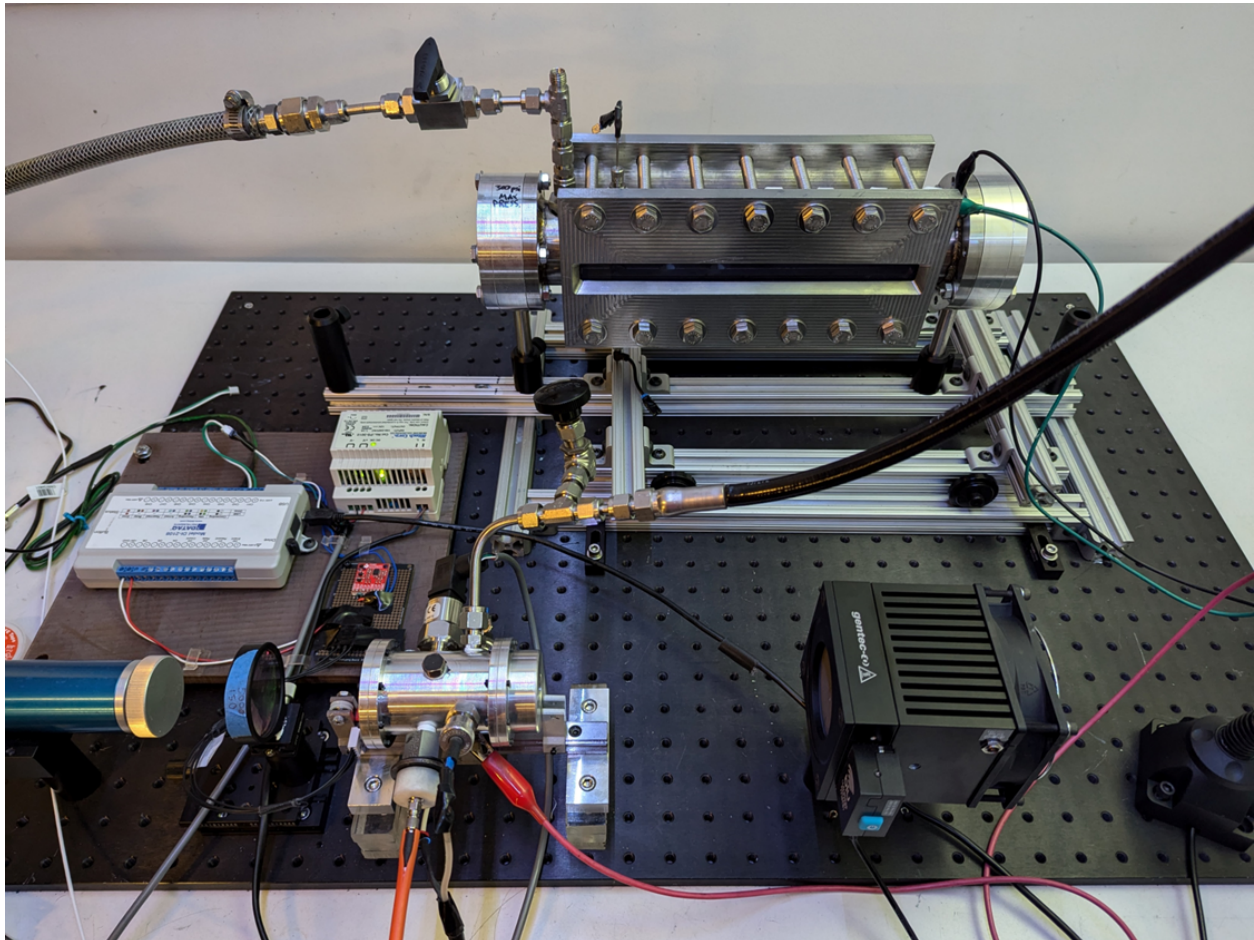


Figure 3.13: Size comparison between V1 (top) and V2 (bottom). V2 is in static configuration, without the extension cylinder.

Chapter 4

Experiments

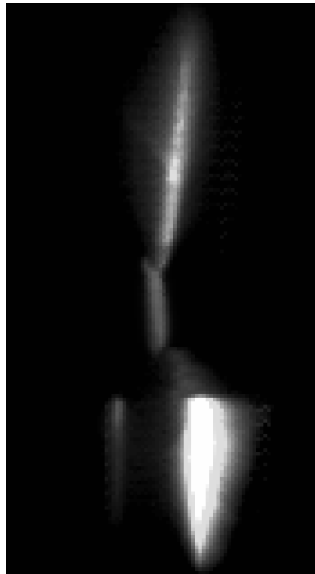
The following chapter will explain the methodology and the results of the various experiments undertaken to develop, validate, and characterize the V2 thruster. Argon gas was used as the propellant in all cases, due to its low cost, safety and ease of ionization.

4.1 Static LSP validation

4.1.1 V1 LSP spark initiation

For spark initiation to work reliably, the laser focus and the spark must both be aligned in space and in time. To resolve the spark spatially, the Photron SA5 camera was placed in front of the V1 test section instead of the laser, looking axially into the test section. This would be the point of view of the laser beam during an LSP shot. [Figure 4.1a](#) shows a composite photo of the added opacities of five spark discharges (without laser). Each frame of the video has an opacity of $1/N$, with N being the total number of frames to add. This gives an average position of the spark, which is seen as being slightly left of the electrodes' centerline.

Using the thickness of the electrode (1.55 mm) as a reference, the spark gap's length is 0.79 mm and the average spark is 0.23 mm wide. Timing data was also recorded for the spark by the high speed camera. To align the laser focus to the spark in time, the laser was reinstalled, and the camera was placed back to its normal position looking into the side of the test section (seen in [Figure 4.1b](#)). The beam was then focused on one of the electrodes at low power. This caused the electrode to glow white-hot when the laser was on. The



(a) Composite photo showing spark between two electrodes. The spark gap is approximately 0.79 mm.



(b) Front of V1 test section showing electrode position. This view is rotated 90° from [Figure 4.1a](#)

Figure 4.1: V1 spark alignment

timings presented in [Figure 4.2](#) were determined by this investigation.

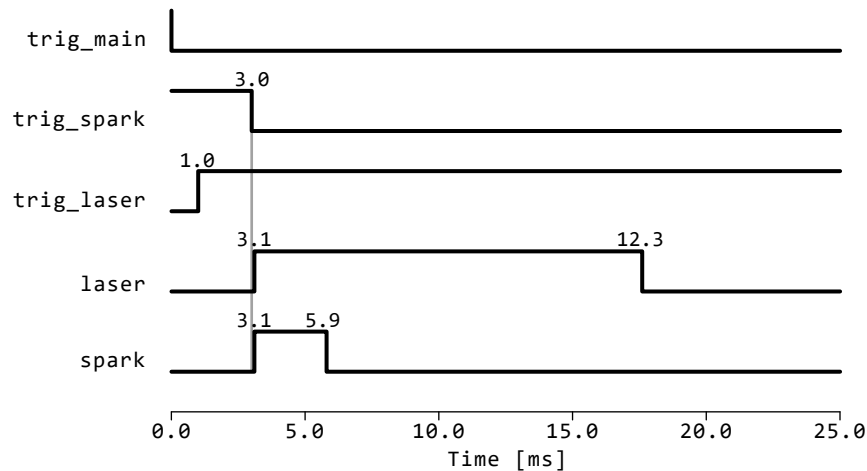


Figure 4.2: Signal timing diagram. The *trig* prefix denotes triggering signals. The component is active when the line is high. Timings in ms are also indicated on the figure.

With the position of the laser aligned to the spark and the timings synchronized, QCW LSP spark initiation in V1 was achieved with a 200 mm focal length lens at 100% power (3079 W) and a pressure of 20 bar, as seen in [Figure 4.3](#).

4. EXPERIMENTS

4.1. STATIC LSP VALIDATION

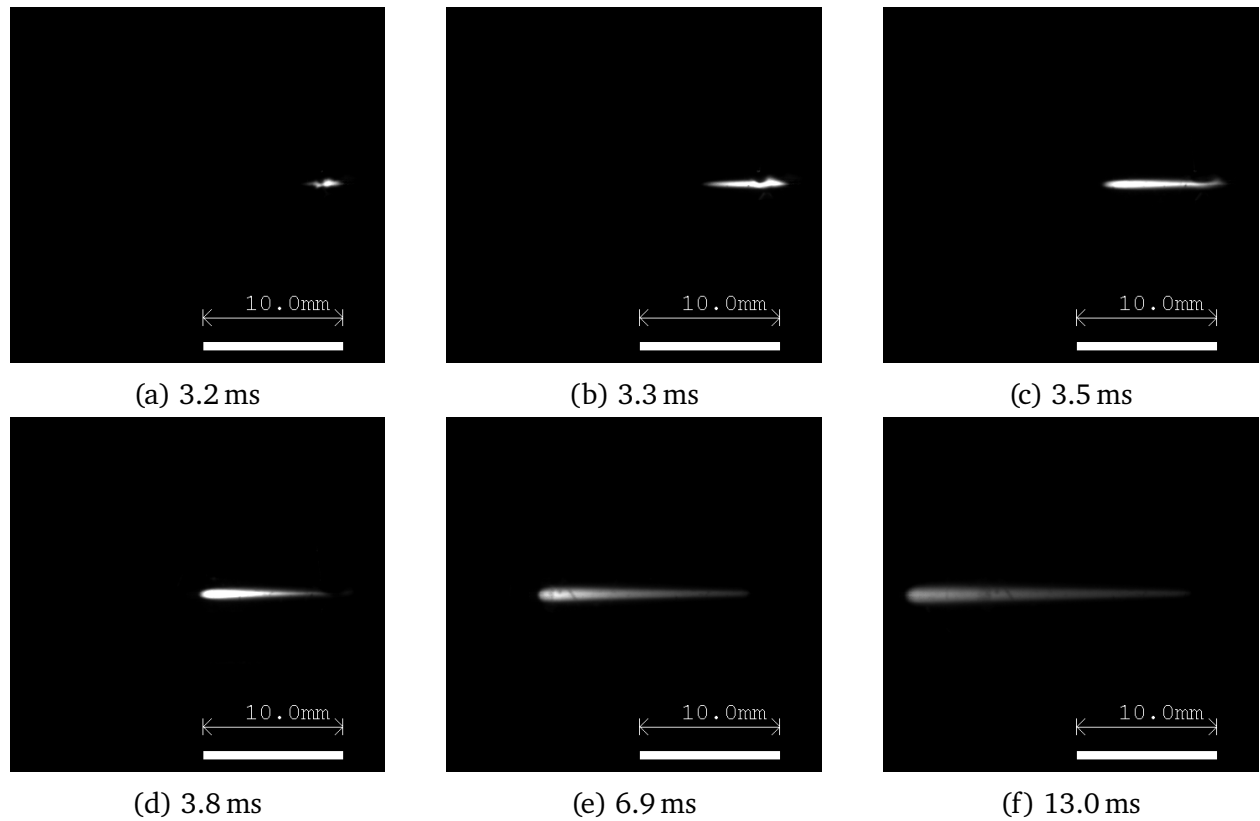


Figure 4.3: QCW LSP spark initiation in V1: 3079 W, 20 bar. LSP142_SPRK15.

The LSP is initiated at 3.2 ms, as soon as the spark is discharged. The front of the LSP moves towards the left (upstream, towards the laser), until the end of the QCW laser pulse at 13 ms. Once the laser ends its emission, the LSP dies down within two frames (0.2 ms).

4.1.2 NO₂ seeding

Comment from Prof. Higgins: If you want to present the NO₂ work, you'll need to: Explain attenuation/absorption coefficient as it appears in Beer-Lambert law and how this defines the length scale over which absorption occurs. Explain how absorption coefficient is derived from the cross-section of the molecule, which will involve using the HITRAN database, etc. It is not acceptable to just say "we added NO₂" and reference it off to some paper.

As the plasma emits in the ultraviolet (UV) range, it is necessary to seed with a gas that absorbs UV but not the infrared (IR) laser. Khan *et al.* [20] shows that NO₂ and SO₂ are two candidates. NO₂ was first used as it was easy to produce in-house in significant quantities. The V1 system was set up with a vacuum pump connected to an outside air exhaust to safely vent the NO₂ gas. The pump was also used to bring the pressure in the test section down

I could include here the dynamic pressure rise of the LSP.

to a rough vacuum before introducing the gasses.

Three control QCW LSP shots were undertaken in pure argon and their dynamic pressure trace from the PCB transducer was recorded. Next, 0.55 bar of NO_2 , or 200 mL at STP, was introduced into the chamber. V1 was then pressurized with argon to 20 bar. With the spark active, three LSPs were generated in the seeded atmosphere. The dynamic pressure rise of the seeded argon was approximately double the one seen in pure argon. The next two LSP shots were conducted with 0.24 bar (85 ml at STP) of NO_2 and filled to 20.2 bar with argon. Again, higher pressure rises were observed, but slightly less than the 0.55 bar shots. The chamber was finally half evacuated to 10.17 bar and then filled back to 20.15 bar with argon. This would have brought the partial pressure of NO_2 to 0.12 bar. Two LSPs were initiated, with a higher pressure rise than pure argon, but less than the higher concentration NO_2 shots. [Figure 4.4](#) presents the averages of these recorded pressure traces.

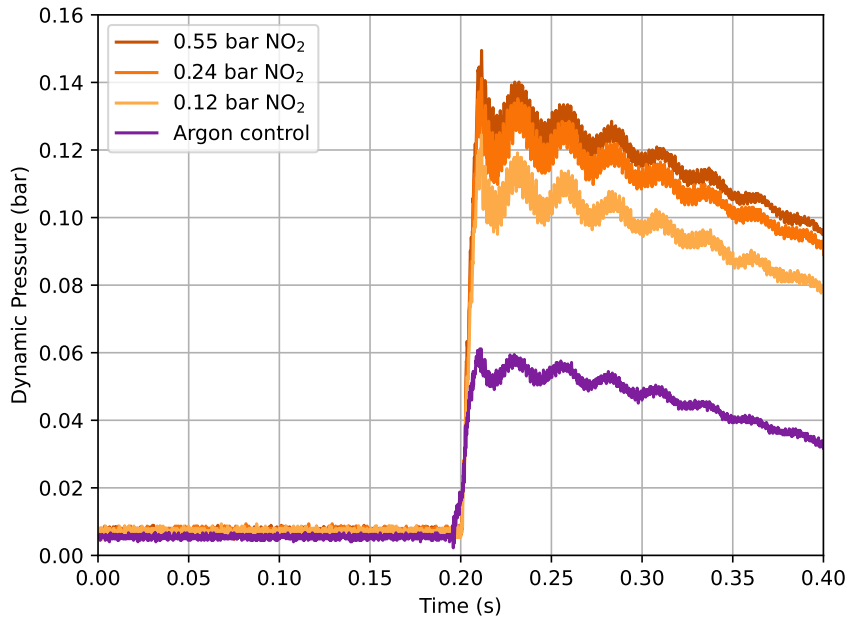


Figure 4.4: Average dynamic pressure rise of QCW LSP shots in a mixture of NO_2 and argon compared to that of pure argon QCW LSP

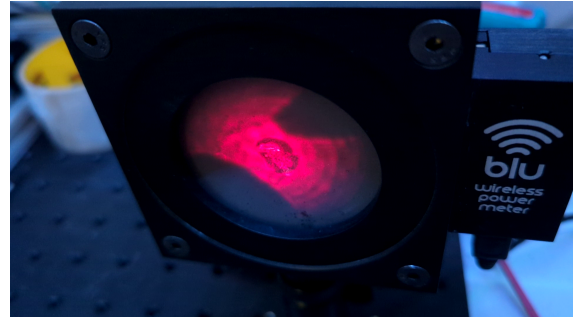
4.1.3 V2 LSP spark initiation and QCW LSP

For V2, the timings of the spark and laser pulse were kept the same as [Figure 4.2](#). To align the laser focus spatially, the power meter was used as a screen to project the visible (red) alignment laser. By moving the V2 test section back and forth on the thrust stand rail, the

field of view (FOV) of the shadows projected on the power meter can be modified, as seen in [Figure 4.5](#). The laser focus can then be moved with the translation stages, so the brightest spot matches the center of the electrodes' shadow.



(a) V2 alignment, zoomed out



(b) V2 alignment, zoomed in

Figure 4.5: 2 FOVs of alignment laser light on power meter. The aberration at the center of the red light is due to laser damage to the window.

Once the laser focus was aligned, a QCW LSP With the Photron SA5 looking into the front of the thruster at an angle, and the PCB transducer recording the pressure rise, LSP initiation was confirmed in V2. [Figure 4.6](#), taken by the webcam, shows the brightness of a full power QCW LSP. Note the bright plasma emission to the left of the image on the laser safety curtain.

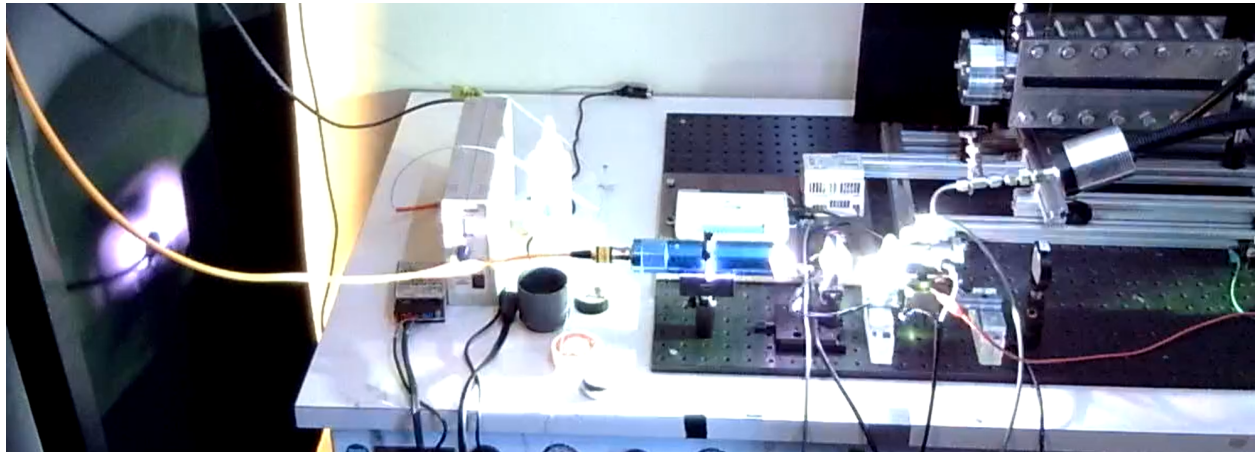


Figure 4.6: 100% power (3079 W) QCW LSP shot

4.1.4 Optical experiments: going from QCW to CW LSP

Due to the low continuous laser power in this experiment compared to others in the literature, increasing the laser flux with a small focus is critical. The real amount of power

in the pulsed shots was measured to get a conversion between the laser power setting (in %) to power (W). 10 shots each at 10 % and 12 % were measured with the power meter, with statistics compiled by the power meter software ([Table 4.1](#)). The average power was calculated by dividing the average pulse energy (J) by the pulse duration (50 ms).

Table 4.1: Statistics from the power meter after 10 times 50 ms laser shots at 10% and 12 % power

Value [Unit]	10x 50 ms shots at 10% power	10x 50 ms shots at 12% power
Average energy value [J]	9.985	12.89
Maximum energy value [J]	10.2	13.3
Minimum energy value [J]	9.63	12.0
RMS Stability [%]	1.690	2.811
PTP Stability [%]	5.599	10.31
Std deviation [J]	0.169	0.362
Average power [W]	200	258

At 10% power, an 9.985 J average during 50 ms gives an average power of 200 W. Extrapolating from these measurements, 300 W is achieved at 13.5 %.

Pulsed shots at lower power levels with a 200 mm focal length lens (Thorlabs LA1979-C) revealed a difficulty to initiate QCW LSP below 30 % power, around 1 kW. This presents a problem, as the maximum CW power of the laser is significantly lower at 342 W (see [Appendix A](#)). A test campaign was started in February 2024 to determine if LSP initiation in the V1 thruster was possible under this maximum CW power level. [Equation 4.1](#) [21] can be used to estimate the diameter at the focus:

$$\text{Spot diameter(mm)} = \frac{4 \times \text{Focal length(mm)} \times \text{Wavelength(mm)} \times M^2}{\pi \times \text{Beam diameter at lens(mm)}} \quad (4.1)$$

The beam propagation factor M^2 is a scale to measure beam quality. A diffraction-limited Gaussian beam has the minimum M^2 of 1 Hecht [17]. The YLR-300/3000 laser has a BPP of 2 mm mrad, as found in [Appendix A](#). As $M^2 = \frac{\pi}{\lambda} \text{BPP}$ [22], this corresponds to an M^2 of 5.87. From [Equation 4.1](#), lowering the focal length of the lens lowers the spot size, increasing laser flux. *Lens Tutorial* [23] also mentions that a dual-lens system can lower the beam diameter at focus.

A single plano-convex lens with a 125 mm focal length (Thorlabs LA1384-C) was then chosen, as it was the lowest focal length lens that could focus at V1's initiation plug position. A 100 mm focal length lens was available, but the focus was before the electrodes, even when pressing the lens against the front window. [Figure 4.7](#) shows a record of LSP initiation

attempts at various power settings and lens axial positions with the 125 mm focal length lens. 20 bar of argon was used for these shots. Power levels lower than 15%, initiation was

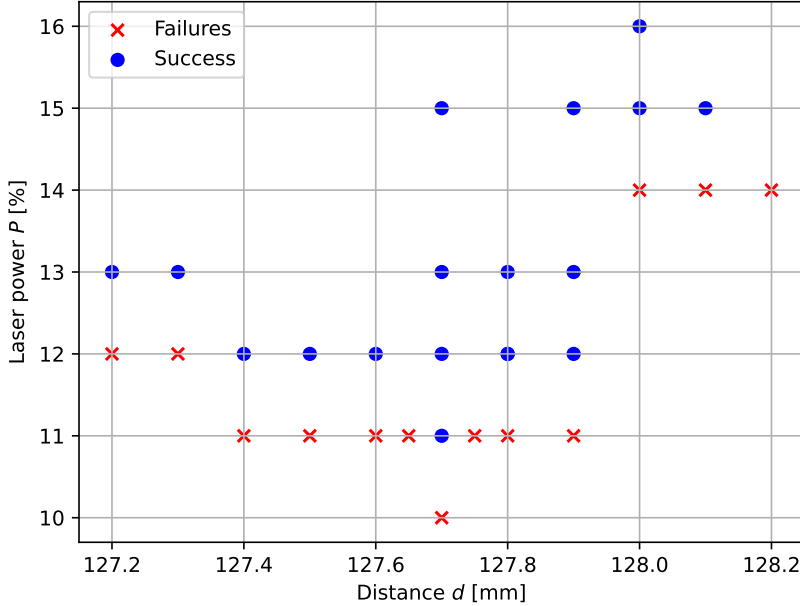


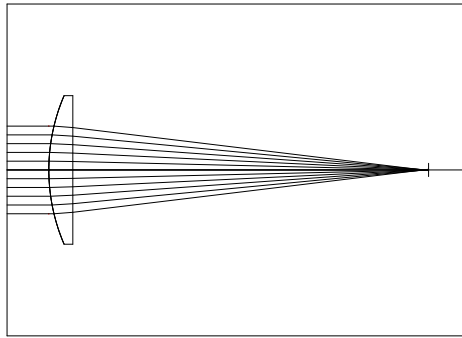
Figure 4.7: LSP threshold graph for V1 with 125 mm focal length lens

unreliable and could take up to 20 attempts to get one initiation. For example, initiation at 11 % was successful once, but it was not possible to replicate this. A tighter focus was necessary to increase initiation reliability by increasing laser flux at the focus, and a dual-lens system was designed.

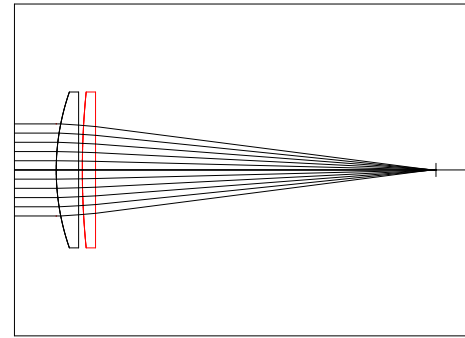
For a dual-lens system, the spot diameter must be calculated numerically. Ray tracing software, such as WinLens3D Basic, calculate the geometry of paraxial¹ rays and show the path of these rays at the focus. WinLens3D was chosen to simulate the spot size of both the single- and dual-lens systems, as it is free and powerful enough for this application. The modelled lenses are seen in Figure 4.8.

With a dual-lens system, the longest focal length lens should be placed first in this case, as the diameter of the beam entering the second lens is maximized. This would lead to a tighter focus. However, it was placed after as it was impossible to mount before with the available mounting hardware. The difference in spot size is minimal. A practical consideration for the experiments is that the LSP will be formed upstream of the laser focus when there is no gas flow. Therefore, the focus needs to be slightly after the initiation system.

¹Rays having small angles and distances to the optical axis



(a) 125 mm focal length lens



(b) Dual-lens 500 mm and 150 mm system

Figure 4.8: Model of the lenses showing paraxial rays and focus

[Figure 4.9](#) presents the spot diagrams that were then produced with WinLens3D. Note the difference in scales and spacing used throughout. From these three spot diagrams, the average laser flux at 342 W was calculated (see [Table 4.2](#)). It is assumed that the laser energy is evenly distributed in a circle as wide as the farthest ray from the center. The

Table 4.2: Simulated focal length and spot diameter of various lens assemblies in WinLens3D. The average laser flux is calculated for 342 W of incident power

Lens	Nominal focal length (mm)	Focal length at 1070 nm (mm)	Beam diameter at focus (mm)	Average laser flux at 342 W (MW/cm ²)
Single	125	122	0.20	1.09
Single	100	93	0.15	1.94
Dual	500, 150	110	0.08	6.80

LSP experiments were continued with this dual-lens system (500 mm and 150 mm focal lengths), as it offers a 6.25 times increase of the laser flux compared to the single 125 mm focal length lens. To increase the laser flux even more, an aspheric lens of comparable focal length could be used, though it costs 10 times as much as a single plano-convex lens.

[Figure 4.10](#) presents a record of LSP initiation attempts at various power settings and lens axial positions with this dual-lens system. The completion of these tests validated the dual-lens design, showing that LSPs in the CW power regime of the laser could be generated. The first LSPs in V2 were therefore done using the dual-lens system. A similar graph to [Figure 4.10](#) was then created with V2 to find the lens position where the minimum laser power could reliably initiate QCW LSP. [Figure 4.11](#) presents these initiation attempts.

4. EXPERIMENTS

4.1. STATIC LSP VALIDATION

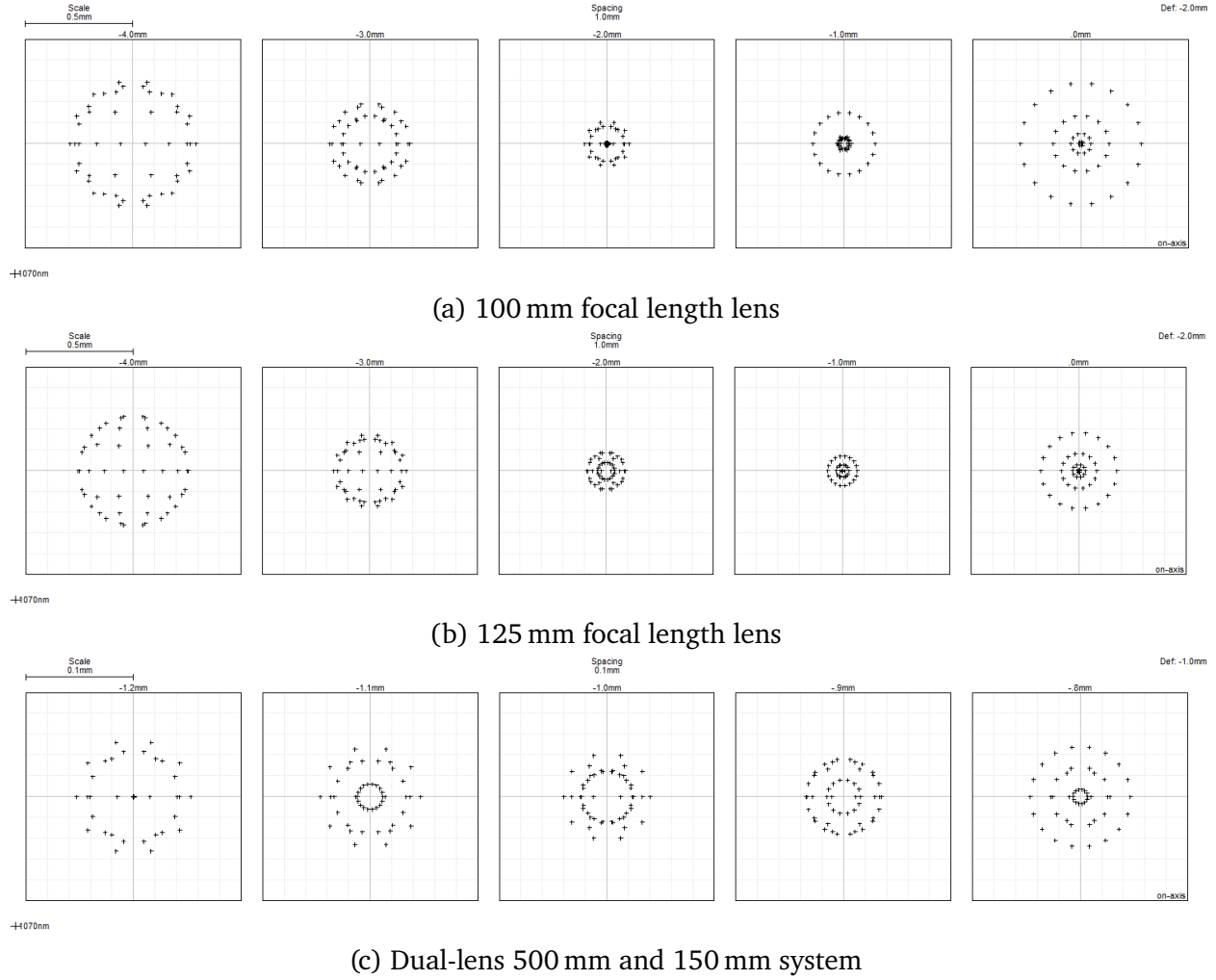


Figure 4.9: Spot diagrams of the three lens systems studied

4.1.5 V2 CW LSP

A 100 % power CW shot was then attempted with 20 bar of static argon.

The webcam footage ([Figure 4.12](#)) will be examined first. The laser is first turned on. A flash marks the spark initiation and lifetime of the LSP. This flash lasts only a few frames. Notice the higher brightness in [Figure 4.12c](#), reflecting off various surfaces like the white box (PCB signal conditioner) on the left of the collimator. The laser was kept running for about a second before it is turned off.

Observation of the high speed camera footage ([Figure 4.13](#)), recorded at 10000 frames per second, showed the CW LSP starting at frame 32 (3.2 ms) and ending at frame 883 (88.3 ms), lasting 85.1 ms. This represents a 1.7 times longer lifetime than the maximum QCW pulse length of 50.0 ms at this power. The brightness of the plasma increases regularly

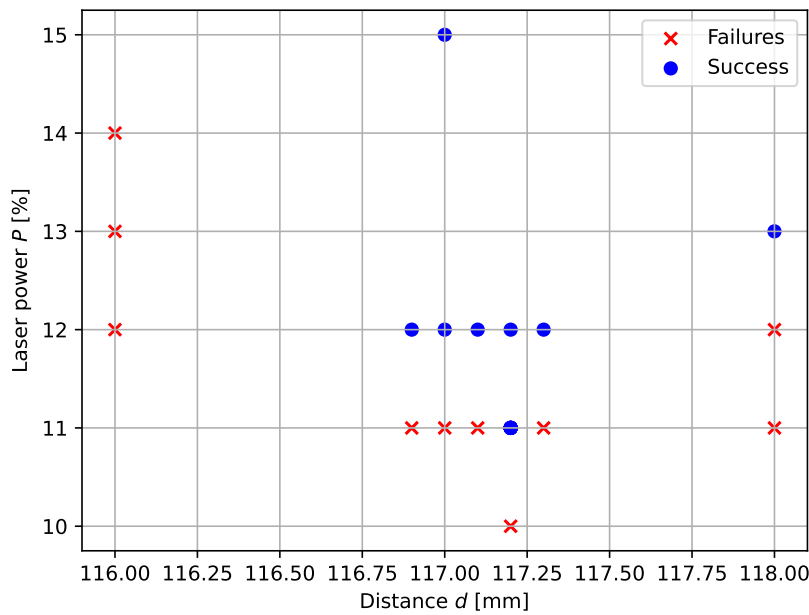


Figure 4.10: LSP threshold graph for V1 with dual-lens system

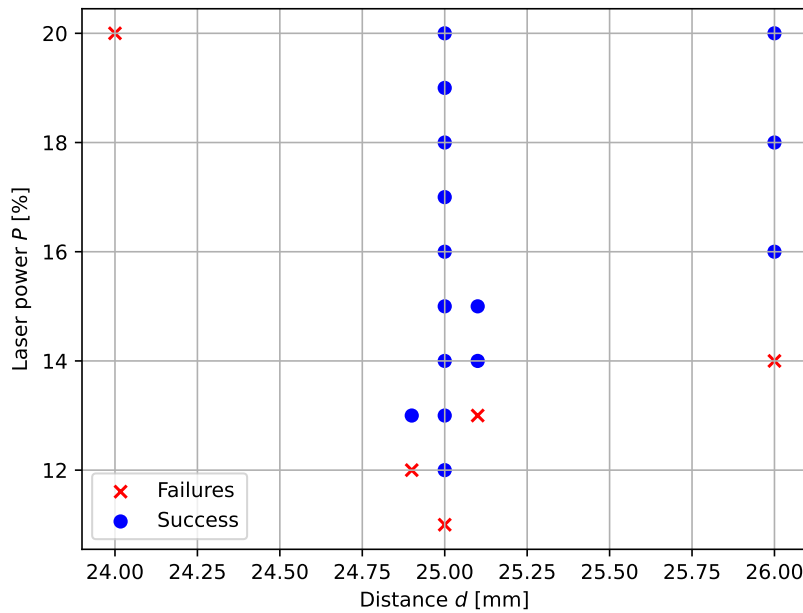
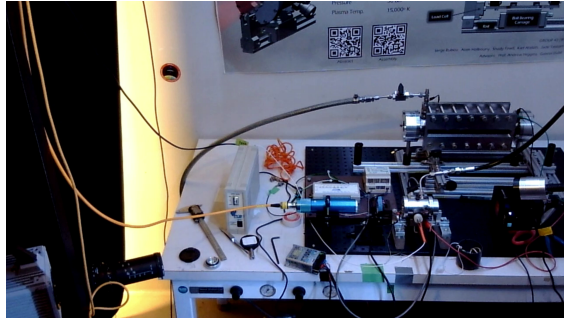


Figure 4.11: LSP threshold graph for V2 with dual-lens system

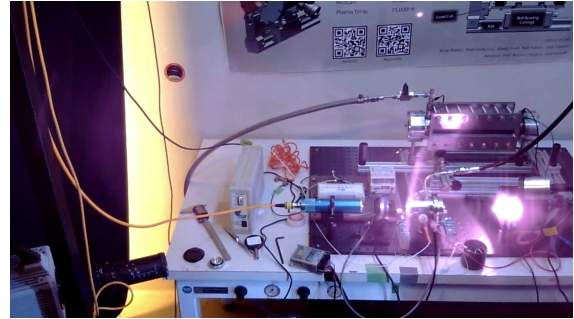
after initiation, to reach its maximum intensity around 50 ms, and this brightness is constant for 10 ms. A flickering of the LSP is seen at 70.0 ms, before it dies down and is completely

4. EXPERIMENTS

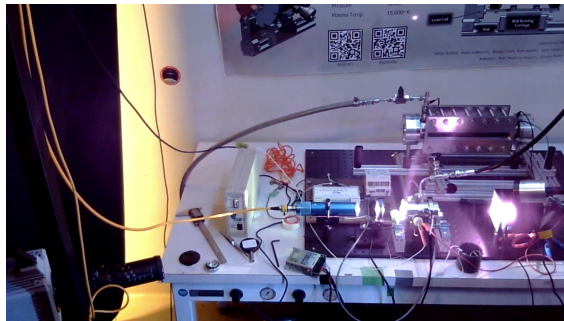
4.1. STATIC LSP VALIDATION



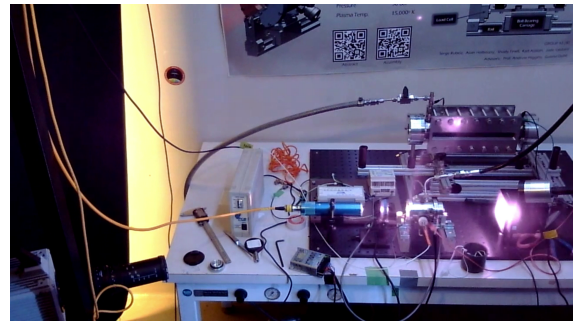
(a) Laser on - 1 s



(b) Laser on + 0 s

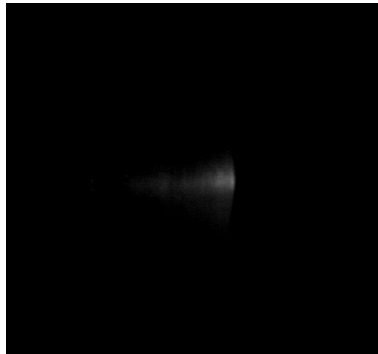


(c) Laser on + 0.5 s: LSP spark initiation

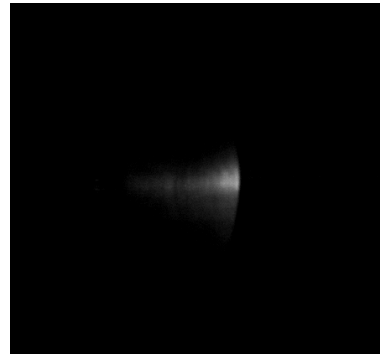


(d) Laser on + 1 s

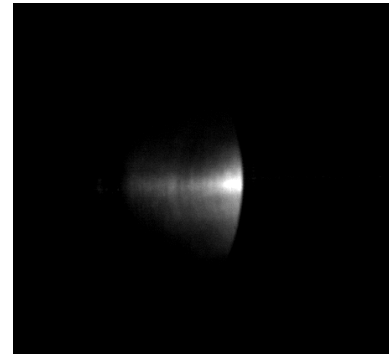
Figure 4.12: First CW LSP captured by the webcam: 342 W, 20.0 bar. LSP385_V2_CW1.



(a) 4.8 ms



(b) 25.0 ms



(c) 50.8 ms

Figure 4.13: First CW LSP captured by the Photron high-speed camera: 314 W, 20.0 bar. LSP385_V2_CW1.

extinguished after 88.3 ms.

[Figure 4.14](#) shows the pressure rise recorded by the PCB transducer connected to the oscilloscope. This was the first CW LSP generated in the lab. Minimal damage to the window was noticed after this test.

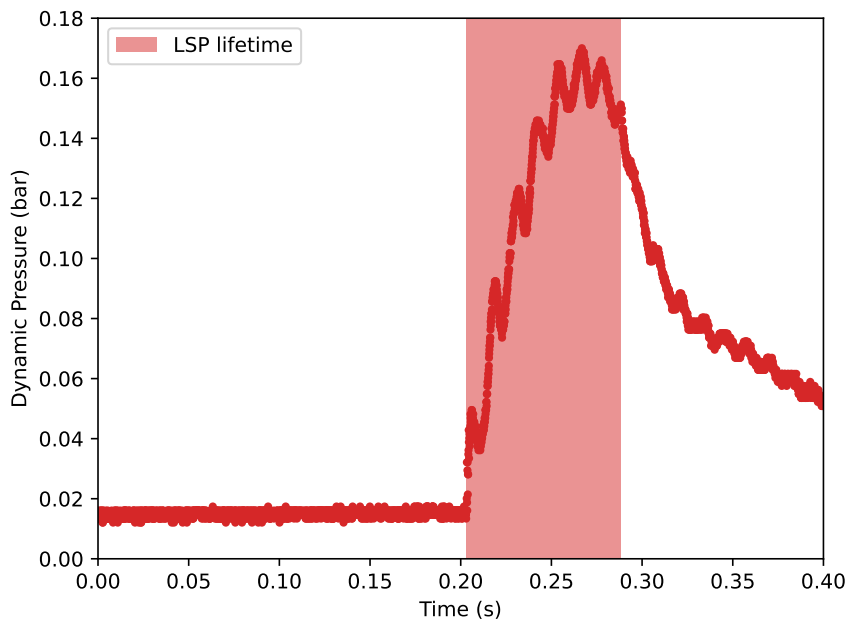


Figure 4.14: Dynamic pressure rise from CW LSP measured with PCB transducer

4.2 V2 Cold flow thruster characterization

4.2.1 Cold flow thrust tests

Cold flow tests (laser off) were completed with V2 to give a baseline measurement of thrust before eventual hot fire tests (laser on), and to validate the functioning of all data acquisition systems.

For thrust tests, pressure and thrust were recorded. [Figure 4.15](#) shows a typical thrust and pressure curve for a chamber pressure of 20 bar. Note that the thrust measurement does not return to the same value it was at initially.

Next, cold flow thrust tests were completed at chamber pressures from 5 bar to 35 bar. A linear curve fit of the experimental results is presented in [Figure 4.16](#).

The empirical relation of pressure versus thrust is given by:

$$\text{Thrust (N)} = 0.0394 * \text{Pressure (bar)} + 0.0318$$

Only 5 points is indeed a bit thin to say its linear.

Repeatability of the thrust measurements was then examined with the Honeywell FSG005WNPB 0 N to 5 N load cell and a 200 g preload, with an argon inlet pressure of 20 bar. The raw

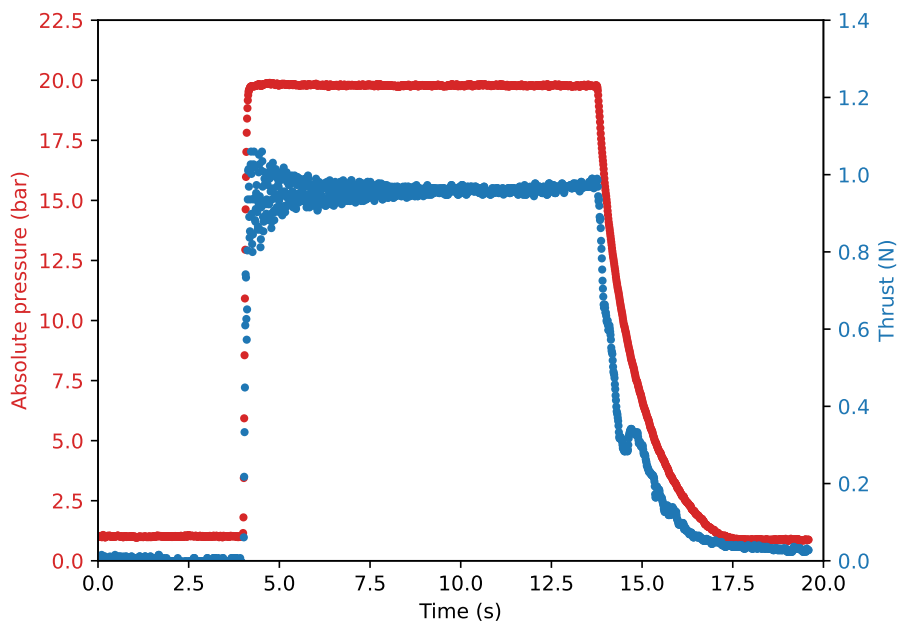


Figure 4.15: Typical cold flow pressure and thrust curves for 20 bar chamber pressure

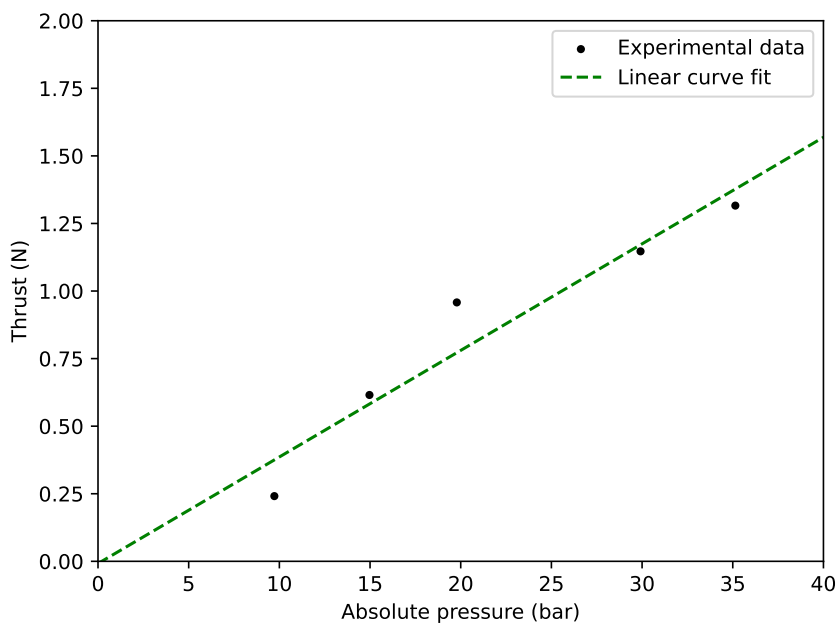


Figure 4.16: Absolute pressure versus thrust and curve fit of pressure-thrust relation

I don't have the calibration for this graph

voltage of the load cell was recorded, as the hysteresis was the point of interest and not the thrust. Significant hysteresis of the thrust stand is seen in [Figure 4.17](#). The final thrust is

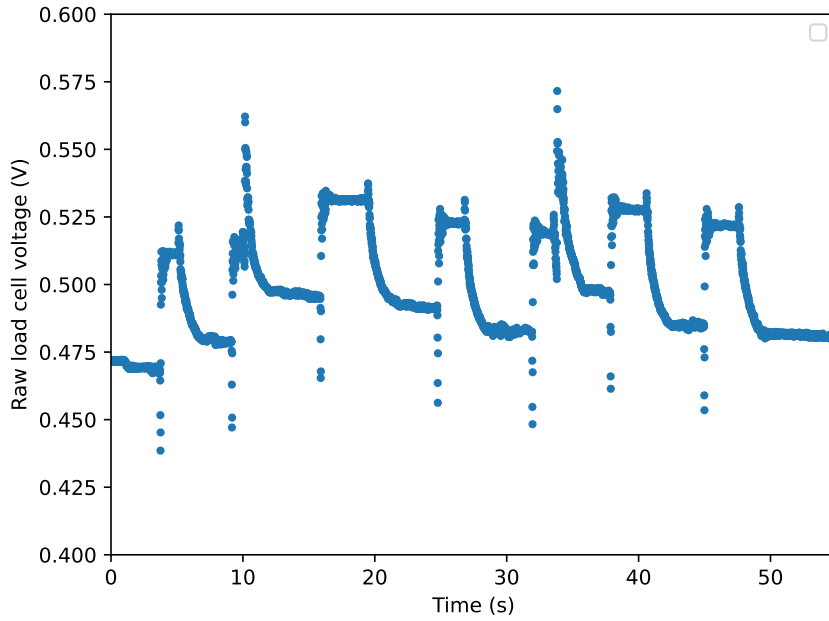


Figure 4.17: Multiple cold flow thrust tests in succession

sometimes higher than the initial thrust, and sometimes the inverse is true. The discontinuities at 10 s and 35 s are due to the accidental shutoff of the gas supply.

4.2.2 Thruster nozzle effective sonic area A^*

To determine the mass flow rate \dot{m} of the thruster, sonic isentropic flow at the nozzle throat is assumed. The following equation can then be used:

$$\dot{m} = \frac{A^* p}{\sqrt{T}} \sqrt{\gamma} \left(\frac{\gamma + 1}{2} \right)^{\frac{-\gamma+1}{2(\gamma-1)}} \quad (4.2)$$

Where A^* , the nozzle effective sonic area, is an unknown, p is pressure, T is temperature, γ is the specific heat ratio, and R is the gas constant.

To characterize the effective sonic area, A^* , of the thruster nozzle, a choked orifice blow-down test was undertaken based upon the theory in Saad [24]. V2 in flowing configuration was pressurized to 20 bar of argon. The argon flow was then closed. The pressure curve was recorded by the Omega transducer.

The internal volume of the V2 thruster in flowing configuration was determined by weighing it before and after it was filled with isopropyl alcohol. Using a density of 785.09 kg/m³, the

A flow meter was not used because we did not have one

volume was found to be $9.68 \times 10^{-6} \text{ m}^3$, or 9.68 ml.

The following expression for the pressure-time history of a blow down choked orifice flow [24] was then implemented in Python. As the timescale is short (less than 10 seconds), the process is considered adiabatic, and the isentropic case is used:

$$t = \frac{-2V \left[\left(\frac{p(t)}{p_i} \right)^{(1-\gamma)/2\gamma} \right]}{(1-\gamma)R\sqrt{T}A \sqrt{\frac{\gamma}{R}} \left(\frac{2}{\gamma+1} \right)^{(\gamma+1)/(\gamma-1)}} \quad (4.3)$$

Where t is time, $p(t)$ is the absolute pressure in the system at time t , p_i is the initial absolute pressure in the system, V is the volume of the V2 thruster and tubing after the valve, T is temperature, A is the area of the nozzle's throat. With this equation, the absolute pressure in bar was plotted versus time in seconds for different values of A , with a specific heat ratio γ of 1.67, a temperature of 300 K, and an R of 208.13 J/kg*K (see Figure 4.18). An experimental pressure curve was also overlaid, similar to Figure 4.15, but cut to only show the decrease in pressure right after the gas feed valve is closed. The time at which this valve is closed is defined as $t = 0$.

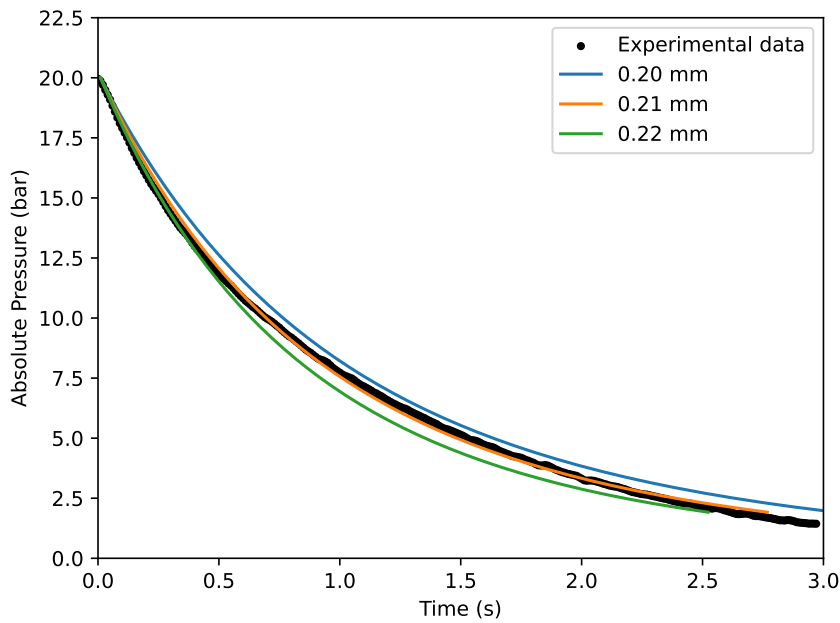


Figure 4.18: Saad blowdown model and experimental data

The best match was found to be an area of $3.46 \times 10^{-8} \text{ m}^2$, giving a diameter of 0.21 mm.

4.2.3 Needle valve effective sonic area A^*

The WL14H-320P needle valve (see [Figure 3.12](#)) was calibrated to relate its rotation increments to its flow rate. This was undertaken by connecting the valve's input to a gas supply, while the valve's output was connected to a bubble flow meter constructed for this experiment ([Figure 4.19](#)). The bubble flow meter and experiment methodology were presented in Barigou and Davidson [25].

A uniform bubble created at the base of the tube rises upwards towards the top of the tube as it is displaced by the pressurizing gas. This end of the tube is open to the atmosphere. A stopwatch is started when the bubble passes the base of the green tape line and stopped once the bubble passes the base of the red tape line. These stopwatch measurements are repeated three times and averaged. This enables precise measurement of the volumetric flow rate.

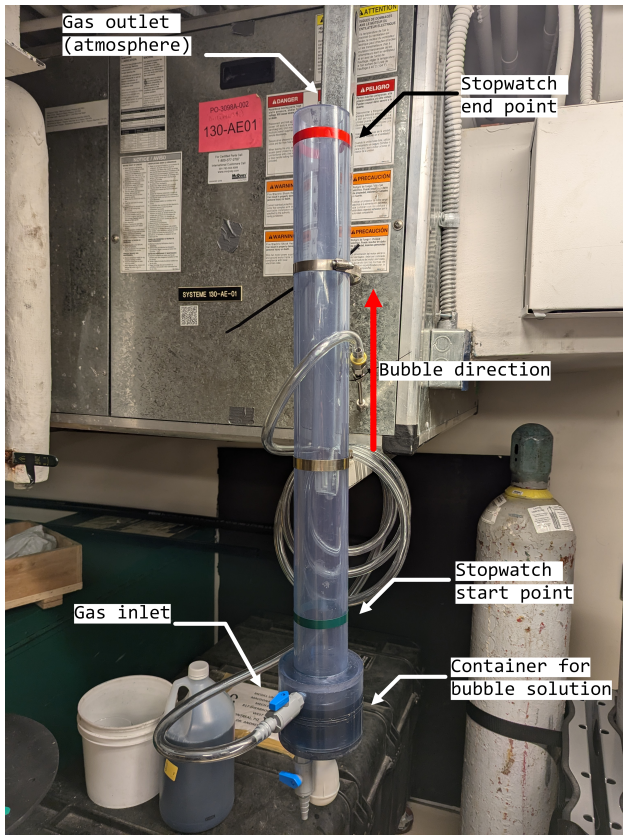


Figure 4.19: Bubble meter setup

First, the valve was calibrated with air at 3.45 bar and 6.89 bar. The valve was then calibrated with 20 bar and 50 bar of argon. The volumetric flow rate was measured in both cases for increments of 0.50 rotations to 2.0 rotations. The calculated opening area of the

valve is presented in [Table 4.3](#).

Table 4.3: Calculated Opening Area for Needle Valve at Different Rotations (Upstream Pressure = 5000 kPa and Outlet Pressure = 100 kPa), adapted from [Appendix C](#)

Increment	Volume Flow (L/s)	Mass Flow (g/s)	Area (mm ²)	Diameter (mm)
0.50	0.25	0.410	0.028	0.188
1.00	0.37	0.607	0.041	0.229
1.10	0.51	0.836	0.057	0.269
1.20	0.67	1.099	0.075	0.308
1.30	0.97	1.591	0.108	0.371
1.40	1.24	2.033	0.138	0.419

Assuming that the temperature inside V2 during CW LSP thrust tests is 1200 K and the mass flow rate is 0.641 g/s, [Appendix C](#) recommends a rotation increment of approximately 1.33 to produce an A^* of 0.147 mm².

4.2.4 Summary of results

[Table 4.4](#) presents a summary of the results determined from cold flow thruster characterization.

Table 4.4: Summary of the studied V2 thruster characteristics

Characteristic	Value and unit
Needle valve A^* with predicted experiment conditions	$0.147 \times 10^{-6} \text{ m}^2$
Nozzle A^*	$3.46 \times 10^{-8} \text{ m}^2$
Internal volume of thruster in flowing configuration	$9.68 \times 10^{-6} \text{ m}^3$
Average cold flow thrust at 20 bar	0.96 N

4.3 Initial QCW LSP thrust tests (hot fire)

With V2 CW LSP achieved, and the cold flow thrust tests completed, initial QCW LSP thrust tests were attempted. The needle valve was not installed as it was not yet procured.

The thrust stand was unfortunately not calibrated before these tests. Thrust values should be closer to 1 N according to previous cold flow data. Nonetheless, the QCW pulse changes the thrust in both cases, but in opposing directions. No concrete increase in thrust could be determined with the current V2 setup when the laser was on.

Didn't have time to measure m_{dot} with the bubble meter, but I could calculate a predicted value

4. EXPERIMENTS

4.3. INITIAL QCW LSP THRUST TESTS (HOT FIRE)

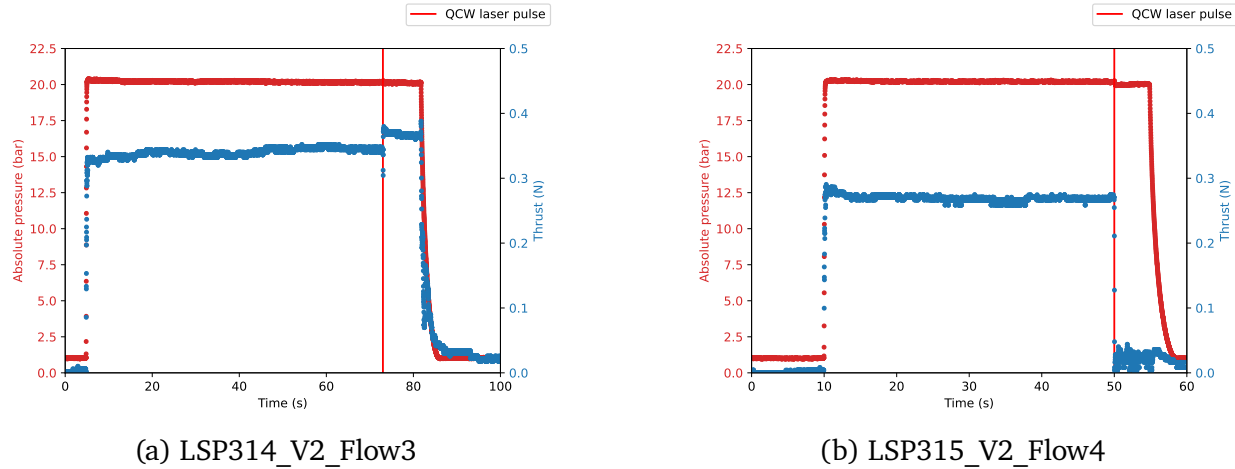


Figure 4.20: Two QCW thrust tests

The following webcam frame (Figure 4.21) was taken from the LSP315_V2_Flow4 3079 W QCW shot, with the electrodes unplugged so no LSP could be initiated. A plasma plume still left the nozzle and the noise of the flow changed once the laser was fired, indicating possible nozzle ablation.

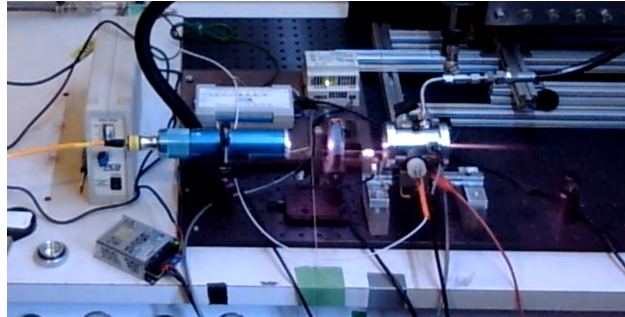


Figure 4.21: Nozzle ablation during flowing test. LSP315_V2_Flow4.

Further flowing tests confirmed that LSP could be initiated by a spark in flowing argon. The following frame (Figure 4.22) from the Photron SA5 shows LSP light emission.

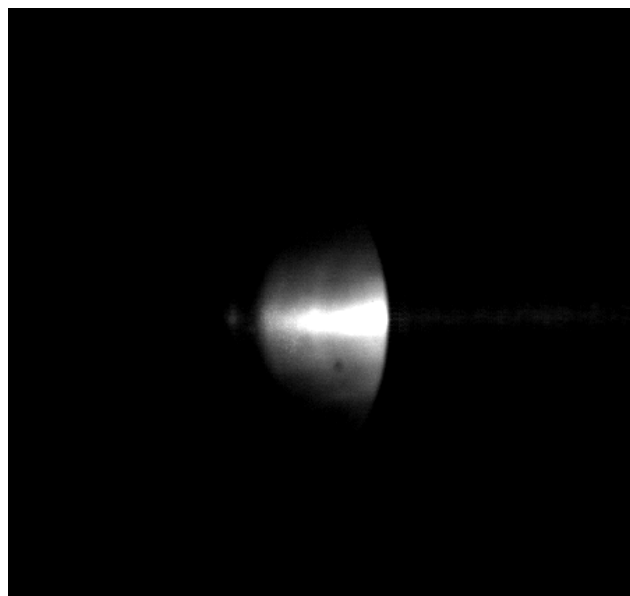


Figure 4.22: V2 Flowing QCW LSP. LSP321_V2_Flow10.

Chapter 5

Discussion

This project was started on the heels of Duplay [4], with the V1 test section using wire initiation during summer 2023. Spark initiation is preferred for a few reasons. First, there would be no solid object blocking the beam path. This would allow the power meter to measure the energy that was not absorbed by the plasma. Second, replacing the target wire is a time-consuming process that was conducted every 1–3 shots, requiring the test section to be re-pressurized. Indeed, spark initiation would allow a much higher shot rate. Third, when conducting flowing experiments, the wire could be moved out of the focus by the flowing argon. Finally, the wire prevents the downstream propagation of the plasma by being physically in the way.

With V1, spark initiation was first attempted with an initiation plug that could fit into a single port, seen in [Figure 5.1](#). The electrodes were side by side. However, the spark was created at a different height every time between the parallel electrodes.

Using opposing electrodes would ensure that their tips were the closest point to each other, greatly increasing spatial repeatability of the spark and enabling the electrode gap length to be easily adjusted. Opposing ports ([Figure 5.2](#)) were drilled into the bottom of the V1 apparatus to fit an electrode through the top and one through the bottom, as seen in [Figure 4.1b](#).

Another critical issue was that of coil burnout. 5 coils were damaged to the point that they could no longer create a strong enough spark across the spark gap. A contributing factor could have been the poor electrode retention of the Ultra-Torr fittings, as 20 bar of gas could visibly push the electrodes away 1 mm to 2 mm. An increase in the spark gap increases its resistance, putting a higher load on the coil. Another concern was electro-

5. DISCUSSION

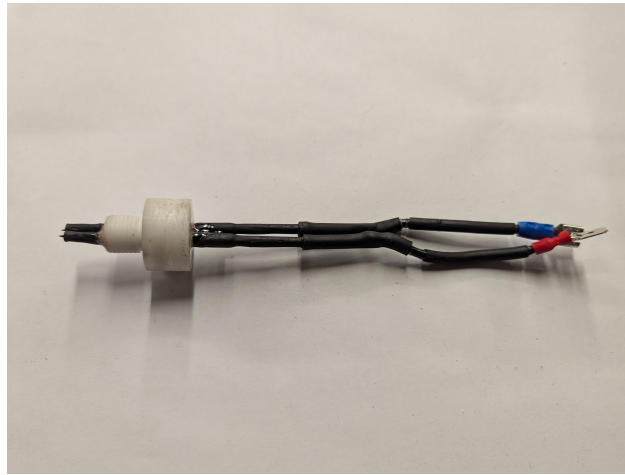


Figure 5.1: V1 single plug electrodes



Figure 5.2: V1 with newly machined opposing bottom ports

magnetic interference between the coil and its power supply. Originally in the same box, the 10 A current-limited power supply and the smart coil were placed in separate electrical boxes. Quad shielded coaxial cable was used between the coil and its controlling delay generator as an additional precaution.

With these problems solved, reliable spark initiation of LSP was achieved in V1. NO₂ seeding

5. DISCUSSION

tests were then undertaken to determine if more laser energy could be captured by the propellant. With as low as (0.6%) of NO₂ mixed with argon, double the pressure rise was observed. This indicated that the propellant was absorbing twice the energy from the plasma. As the NO₂ fraction was increased, there were diminishing returns to the pressure rise. This was encouraging, as not much NO₂ is needed to have a great impact on the energy absorption.

However, this test section was made of steel, creating too much friction on its rails during thrust tests. This was mitigated in part by a rope system mentioned in Duplay [4], but was not found to be repeatable. Having the LSP heat a smaller internal volume than the 0.38 L of V1 was also desirable, as a greater effect on internal pressure and thrust would be seen.

Critically, rubber seals were exposed to the laser path during continuous (CW) lasing with a lower focal length lens (picture), severely burning them in the only CW test conducted. A shorter test section designed for a 100 mm focal length lens would allow the beam to pass through without hitting the sides of the test section. A purpose-built test section, named V2, was therefore designed over the course of two semesters.

The achievement of consistent spark initiation with V1 coincided with the arrival of the V2 test section parts in late April. Static pressure testing of V2 up to 75 bar for 25 minutes was completed successfully. However, the off-the-shelf 44 kV wire originally intended to be used as the electrodes burst during pressure tests. An electrode redesign was therefore necessary. Molded dielectric epoxy (Stycast ES 1001 McMaster-Carr [26]) around an industrial sewing needle core was chosen, as it was economical and the outer diameter of the electrodes could be precisely controlled by sanding the surface of the set epoxy. Molds were 3d printed and Mann Ease Release™300 was applied to all their inside surfaces.



(a) Molds with steel needle core in place



(b) Molding process



(c) Assembled electrodes with Ultra-Torr cap and electrical connectors

Figure 5.3: Electrode manufacturing process

The electrodes were then sanded down to fit tightly into Ultra-Torr vacuum connectors.

5. DISCUSSION

Although these connectors were not designed for high pressure, previous experience has shown that they are appropriate up to about 20 bar of internal pressure if tightened enough. The result is presented in [Figure 5.3c](#). Once installed in the V2 thruster, the electrodes were pushed into contact with each other and the Ultra-Torr connectors tightened. Statically pressurizing V2 to 20 bar was enough to separate the electrodes from one another by about 1 mm.

With the dual-lens system, static LSP via spark initiation in V2 was achieved on the first QCW shot at 100% power (3050 W). This was initially done with a flat aluminum plate at the end of the test section (see [Figure 5.4](#) and [Appendix E](#)).

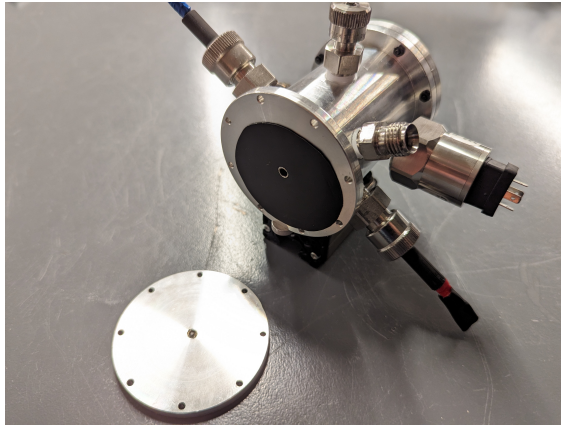


Figure 5.4: Ablation damage to the flat rear plate of the thruster after two 3 kW laser shots

The black sheet in [Figure 5.4](#) is Thorlabs laser-absorbing aluminum foil, used in a failed attempt to protect the rear plate from damage. In addition to this ablation problem, the laser could only be aligned between the electrodes when the rear plate was taken off. This required re-pressurization after every attempt at alignment. Given that the electrodes would also move under the 20 bar pressure, this was very tedious.

To solve this, a second window holder was machined ([Appendix F](#)) that would replace the flat plate. The laser could then be aligned when the test section was pressurized, and the alignment could be changed without opening the thruster. The window allowed the laser energy that was not absorbed by the plasma to pass freely through the apparatus, also enabling power meter measurements. With the new window mount installed, the goal was then to bring the QCW initiation power down to the maximum CW power of the laser, 342 W, in order to attempt a CW LSP.

A dual-lens system was designed to increase laser flux at the focus by decreasing the area of the focus while keeping the power constant. The lenses were validated with V1 and used

5. DISCUSSION

in all of V2's LSP shots. Once a LSPs lower than 342 W were initiated reliably, our first 100% power (342 W) CW LSP was generated for 85.1 ms, a 1.7 times longer lifetime than the maximum QCW pulse length of 50.0 ms. While these results were encouraging, more experiments with CW laser operation must be completed to determine if lifetimes can be extended to an order of magnitude more, i.e. around one second. This would greatly help with measuring a difference in thrust when the laser is on.

After the first CW LSP, more CW and pulsed shots were attempted. These continued to damage the rear window, as seen in the center of [Figure 5.5](#). Eventually, a 3 s CW shot melted it severely enough that visual laser alignment between the electrodes of V2 was no longer possible. A window extension tube (seen in [Figure 5.6](#), drawings in [Appendix G](#))

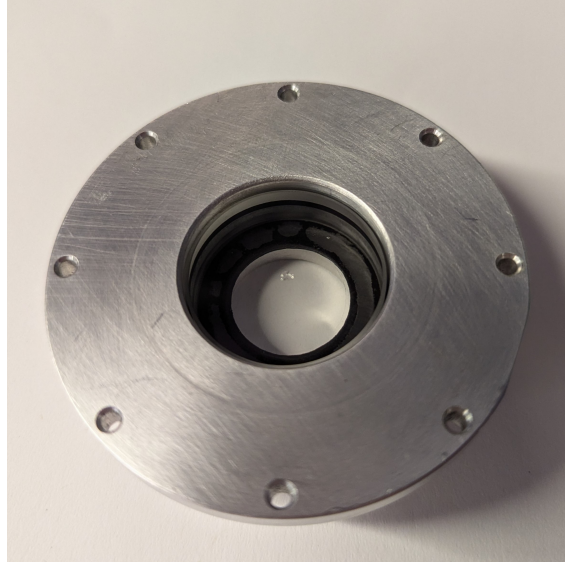


Figure 5.5: Rear window damage on V2

was manufactured to solve this, moving the rear window downstream to where the laser flux density is comparable to the front window, where no damage was seen. This extension tube has yet to be tested.

In parallel to the static LSP validation, characterization of the thruster with argon cold flow was advanced. High hysteresis of the thrust measurements was found, with the thrust stand often not returning to its original zero after a cold flow test. To attempt to correct these problems, a more sensitive load cell was installed with a 0 N to 5 N force sensing range (Honeywell FSG005WNPB). Lubricant was also added to the cart's bearings. However, the issue remained (see [Figure 4.17](#)) due to high friction between the rail and the ball bearing carriage preventing the thruster from resetting at the same place every time. The present type of thrust stand is therefore inadequate for future thrust tests. A different type of thrust

5. DISCUSSION

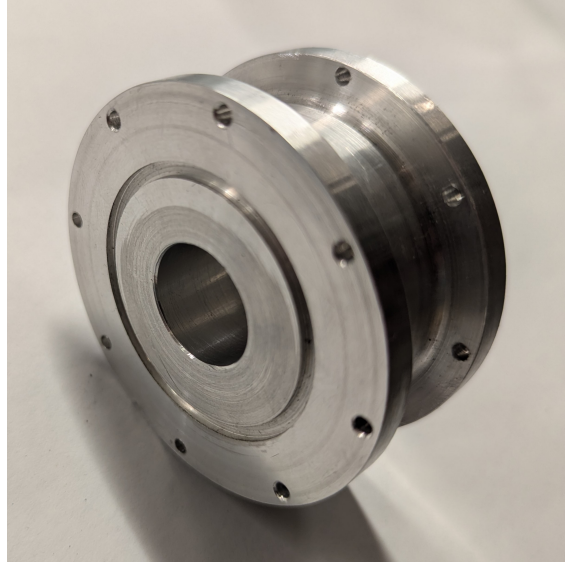


Figure 5.6: Window extension tube

stand (e.g. a rotating arm), should be built to measure thrust repeatably and reliably.

Initial QCW LSP (hot fire) thrust tests aimed to determine if QCW LSP initiated by a spark in flowing argon was possible with V2, and if usable thrust data could be collected. It was shown that LSP could be initiated, and a change of thrust was measured, but this was due to nozzle ablation in all cases. [Figure 4.21](#) shows nozzle ablation during a QCW flowing test, with [Figure 5.7](#) showing the damage to the nozzle afterward. No LSP was initiated in this test, however a plasma plume can be seen exiting the nozzle. This plasma was generated by nozzle ablation, proving that this experiment can operate as a laser ablation thruster. This was not what the thruster was designed for, and lead to a redesign of the V2 nozzle. To solve the ablation of the aluminum nozzle under pulsed laser shots, a new backplate ([Figure 5.8a](#) and [Appendix G](#)) was manufactured to accept nozzle inserts. Toyoda *et al.* [13] use a refractory metal, tungsten, as the nozzle material. Other possibilities are machinable ceramics, stainless steel or graphite. Graphite was chosen as it was already used by Shoji [6] and is economical. These inexpensive, changeable inserts ([Figure 5.8b](#) and [Appendix G](#)) were made from superfine iso-molded graphite rods sourced from Graphitestore (0.500" diameter x 12" L, SKU GT001685). V2's inner cylinder was also re-machined ([Appendix G](#)) to guarantee a seal with the new nozzle. Due to machining delays however, these final parts are still to be tested.

Longer term, to ultimately test LTP as a viable means of space propulsion, more improvements to the V2 setup can be envisioned. A simple but costly one is to use a more powerful laser, instead of the 300 W CW one used here. This would increase thrust and laser absorp-

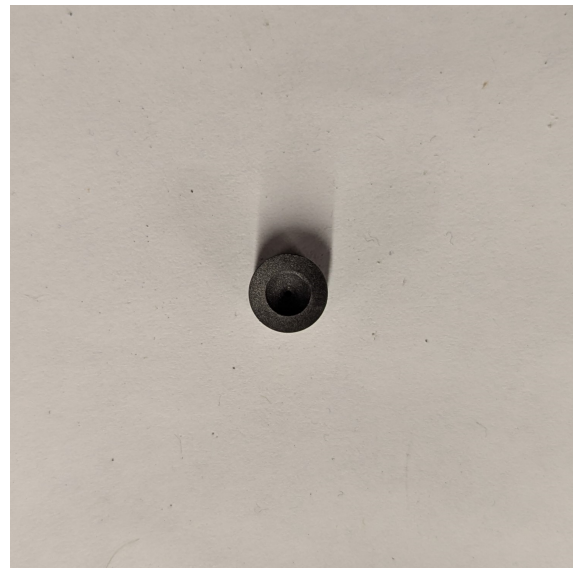
5. DISCUSSION



Figure 5.7: Nozzle laser damage



(a) Nozzle retention plate



(b) Graphite nozzle insert

Figure 5.8: New nozzle parts

tion by the plasma, making an eventual thrust increase easier to detect. Using hydrogen as a propellant instead of argon would increase the thruster's specific impulse. However, it would be harder to ionize, possibly requiring higher laser power or better focusing optics. A hydrogen LTP thruster would also need to be run inside a vacuum chamber, as hydrogen is extremely flammable.

Chapter 6

Conclusion

Gabriel: Conclusion is still a work in progress.

This thesis lays the groundwork for future thrust tests with longer plasma lifetimes and better thrust measurement, which would show the thrust added by the laser.

Static LSP tests showed successful spark initiation of QCW LSP in V1 and V2, and an 85.1 ms CW LSP. A new window mount for V2 was successfully. NO₂ seeding was also investigated in V1 as a way to increase energy retention by the gas, and resulted in a twofold increase in argon dynamic pressure.

Cold flow thruster characterization measured thrust of about 1 N at 20 bar. To get repeatable thrust measurements without significant hysteresis, the need for a new thrust stand design with less friction was made clear. Flowing QCW LSP tests lead to a new nozzle design to prevent significant ablation due to laser energy that was not absorbed by the LSP.

Measurements of the mass flow rate \dot{m} of V2 with the bubble flow meter are still to be completed. Once the new parts for V2 are installed and pressure tested, CW LSP tests can restart to explore longer plasma lifetimes.

Long term, to ultimately test if LTP is a viable means of space propulsion:

- Use a more powerful laser
- Move to hydrogen as a propellant
- Complete thrust tests in vacuum

References

- [1] P. Lubin, “A Roadmap to Interstellar Flight,”
Journal of the British Interplanetary Society, vol. 69, no. 2, pp. 40–72, 2 Feb. 2016.
DOI: [10.48550/arXiv.1604.01356](https://doi.org/10.48550/arXiv.1604.01356). [Online]. Available:
<http://arxiv.org/abs/1604.01356>.
- [2] A. Kantrowitz, “The Relevance of Space,”
Bulletin of the Atomic Scientists, vol. 27, no. 4, pp. 32–33, 4 Apr. 1, 1971,
ISSN: 0096-3402. DOI: [10.1080/00963402.1971.11455353](https://doi.org/10.1080/00963402.1971.11455353). [Online]. Available:
<https://doi.org/10.1080/00963402.1971.11455353>.
- [3] E. Duplay, Z. F. Bao, S. Rodriguez Rosero, A. Sinha, and A. Higgins, “Design of a rapid transit to Mars mission using laser-thermal propulsion,”
Acta Astronautica, vol. 192, pp. 143–156, Mar. 1, 2022, ISSN: 0094-5765.
DOI: [10.1016/j.actaastro.2021.11.032](https://doi.org/10.1016/j.actaastro.2021.11.032). [Online]. Available: <https://www.sciencedirect.com/science/article/pii/S0094576521006305> (visited on 2024-06-14).
- [4] E. Duplay, “Argon Laser-Plasma Thruster: Design and Test of a Laboratory Model,”
M.S. thesis, Technical University Delft, Delft, 2024, 149 pp. [Online]. Available:
<https://repository.tudelft.nl/islandora/object/uuid%3A3a853f2e-2d8c-496b-a016-9e9855e8069c> (visited on 2024-02-02).
- [5] N. A. Generalov, V. P. Zimakov, G. I. Kozlov, V. A. Masyukov, and Yu. P. Raizer, “Continuous optical discharge,” *Soviet Journal of Experimental and Theoretical Physics Letters*, vol. 11, pp. 302–304, 1970.
- [6] J. M. Shoji, “Laser-heated rocket thruster,” NASA-CR-135128, Apr. 12, 1977.
[Online]. Available: <https://ntrs.nasa.gov/citations/19770017244> (visited on 2024-02-02).
- [7] J. Shoji and V. Larson, “Performance and heat transfer characteristics of the laser-heated rocket - A future space transportation system,”

REFERENCES

- in *12th International Electric Propulsion Conference*, ser. International Electric Propulsion Conference, American Institute of Aeronautics and Astronautics, Nov. 14, 1976. doi: [10.2514/6.1976-1044](https://doi.org/10.2514/6.1976-1044). [Online]. Available: <https://arc.aiaa.org/doi/10.2514/6.1976-1044> (visited on 2024-02-02).
- [8] D. Keefer, R. Welle, and C. Peters, “Power absorption in laser-sustained argon plasmas,” *AIAA Journal*, vol. 24, no. 10, pp. 1663–1669, Oct. 1986, issn: 0001-1452. doi: [10.2514/3.9498](https://doi.org/10.2514/3.9498). [Online]. Available: <https://arc.aiaa.org/doi/10.2514/3.9498> (visited on 2024-03-12).
- [9] H. Krier, J. Mazumder, T. Rockstroh, T. Bender, and R. Glumb, “Continuous wave laser gas heating by sustained plasmas in flowing argon,” *AIAA Journal*, vol. 24, no. 10, pp. 1656–1662, Oct. 1986, issn: 0001-1452. doi: [10.2514/3.9497](https://doi.org/10.2514/3.9497). [Online]. Available: <https://arc.aiaa.org/doi/10.2514/3.9497> (visited on 2024-02-02).
- [10] D. K. Zerkle, S. Schwartz, A. Mertogul, X. Chen, H. Krier, and J. Mazumder, “Laser-sustained argon plasmas for thermal rocket propulsion,” *Journal of Propulsion and Power*, vol. 6, no. 1, pp. 38–45, 1990, issn: 0748-4658. doi: [10.2514/3.23220](https://doi.org/10.2514/3.23220). [Online]. Available: <https://doi.org/10.2514/3.23220> (visited on 2024-02-03).
- [11] X. Chen and J. Mazumder, “Emission spectroscopy of cw CO₂ laser-sustained argon plasma: Effects of gas-flow speed,” *Journal of Applied Physics*, vol. 66, no. 12, pp. 5756–5762, Dec. 15, 1989, issn: 0021-8979. doi: [10.1063/1.343644](https://doi.org/10.1063/1.343644). [Online]. Available: <https://doi.org/10.1063/1.343644> (visited on 2024-07-18).
- [12] J. Black, H. Krier, and R. J. Glumb, “Laser Propulsion 10-kW Thruster Test Program results,” *Journal of Propulsion and Power*, vol. 11, no. 6, pp. 1307–1316, 6 Nov. 1995, issn: 0748-4658, 1533-3876. doi: [10.2514/3.23973](https://doi.org/10.2514/3.23973). [Online]. Available: <https://arc.aiaa.org/doi/10.2514/3.23973>.
- [13] K. Toyoda, K. Komurasaki, and Y. Arakawa, “Thrust performance of a CW laser thruster in vacuum,” *Vacuum*, 3rd International Symposium on Applied Plasma Science (ISAPS 01), vol. 65, no. 3, pp. 383–388, 3 May 27, 2002, issn: 0042-207X. doi: [10.1016/S0042-207X\(01\)00446-8](https://doi.org/10.1016/S0042-207X(01)00446-8). [Online]. Available: <https://www.sciencedirect.com/science/article/pii/S0042207X01004468>.
- [14] Q. Lu *et al.*, “Characteristic Diagnostics of a Laser-Stabilized High-Pressure Argon Plasma by Optical Emission Spectroscopy,”

REFERENCES

- IEEE Transactions on Plasma Science*, vol. 50, no. 9, pp. 2578–2587, Sep. 2022, ISSN: 1939-9375. doi: [10.1109/TPS.2022.3172977](https://doi.org/10.1109/TPS.2022.3172977). [Online]. Available: <https://ieeexplore.ieee.org/document/9784436> (visited on 2024-03-25).
- [15] T. Kamei, M. Matsui, and T. Ono, “Methane and Methane–Xenon Laser Sustained Plasma using High Power Diode Laser for Space Propulsion,” *TRANSACTIONS OF THE JAPAN SOCIETY FOR AERONAUTICAL AND SPACE SCIENCES, AEROSPACE TECHNOLOGY JAPAN*, vol. 18, no. 5, pp. 271–275, 2020, ISSN: 1884-0485. doi: [10.2322/tastj.18.271](https://doi.org/10.2322/tastj.18.271). [Online]. Available: https://www.jstage.jst.go.jp/article/tastj/18/5/18_18.271/_article (visited on 2024-02-02).
- [16] S. Takano, Y. Homme, Y. Arakaki, and M. Matsui, “Demonstration of Diode Laser-sustained Argon Plasma Thruster using various F-number,” in *AIAA SCITECH 2024 Forum*, American Institute of Aeronautics and Astronautics. doi: [10.2514/6.2024-2704](https://doi.org/10.2514/6.2024-2704). [Online]. Available: <https://arc.aiaa.org/doi/abs/10.2514/6.2024-2704> (visited on 2024-07-18).
- [17] J. Hecht, *Understanding Lasers: An Entry Level Guide*, 4th ed. Hoboken: John Wiley & Sons, Inc., 2019, ISBN: 978-1-119-31064-8.
- [18] B. J. McBride, M. J. Zehe, and S. Gordon, *NASA Glenn Coefficients for Calculating Thermodynamic Properties of Individual Species*, Sep. 1, 2002. [Online]. Available: <https://ntrs.nasa.gov/citations/20020085330> (visited on 2024-07-15).
- [19] “CEARUN rev4.” (), [Online]. Available: <https://cearun.grc.nasa.gov/> (visited on 2024-07-26).
- [20] S. Khan, D. Newport, and S. Le Calvé, “Gas Detection Using Portable Deep-UV Absorption Spectrophotometry: A Review,” *Sensors*, vol. 19, no. 23, p. 5210, 23 Jan. 2019, ISSN: 1424-8220. doi: [10.3390/s19235210](https://doi.org/10.3390/s19235210). [Online]. Available: <https://www.mdpi.com/1424-8220/19/23/5210> (visited on 2024-06-14).
- [21] “Laser spot size and beam waist calculator and formulas,” Gentec-EO. (), [Online]. Available: <https://www.gentec-eo.com/laser-calculators/beam-waist-spot-size> (visited on 2024-07-25).
- [22] D. R. Paschotta. “Beam parameter product.” (), [Online]. Available: https://www.rp-photonics.com/beam_parameter_product.html (visited on 2024-03-26).

REFERENCES

- [23] “Lens Tutorial,” Thorlabs. (), [Online]. Available: <https://www.thorlabs.com> (visited on 2024-07-30).
- [24] M. A. Saad, *Compressible Fluid Flow*. Englewood Cliffs.
- [25] M. Barigou and J. F. Davidson, “The fluid mechanics of the soap film meter,” *Chemical Engineering Science*, vol. 48, no. 14, pp. 2587–2597, Jul. 1, 1993, ISSN: 0009-2509.
DOI: [10.1016/0009-2509\(93\)80269-V](https://doi.org/10.1016/0009-2509(93)80269-V). [Online]. Available: <https://www.sciencedirect.com/science/article/pii/000925099380269V> (visited on 2024-08-04).
- [26] “McMaster-Carr.” (), [Online]. Available: <https://www.mcmaster.com/> (visited on 2024-10-14).

Appendix A

YLR-300/3000-QCW-MM-AC Calibration Report

	TEST RESULTS YTTERBIUM FIBER LASER Model YLR-300/3000-QCW-MM-AC S/N PLMP31901422	Form: Revision: Spec: Page:	P69-00051 1 G22-29650 rev.4 1 of 6
---	---	--------------------------------------	---

This product is covered by the U.S. Pat. Nos. 5,422,897 and 5,774,484 and any foreign counterparts thereof, and other patents pending.

The information and the following charts provided below is the result of tests performed in controlled environments by IPG Photonics. These provided useful, but not warranted, information about the functions and performance of the product.

N	Characteristic	Symbol	Test Conditions	Min	Typ.	Max	Test Results	Unit
Optical characteristics								
1.1	Operation Mode						Pulsed / CW	
1.2	Maximum Average Power	P_{average}	Pulsed mode	300			307.9	W
		P_{CW}	CW mode	300			342.0	W
1.3	Maximum Peak Power	P_{peak}	Pulsed mode				3079.25	W
1.4	Duty Cycle	DC	Pulsed mode				50 ¹⁾	Tested %
1.5	Pulse Duration	τ	Pulsed mode	0.2			50 ²⁾	0.2-50 ms
1.6	Maximal Pulse Energy	E_{max}	Pulsed mode	30			30.8	J
1.7	Emission Wavelength	λ			1070		1069.6	nm
1.8	Emission Linewidth	$\Delta\lambda$	Pulsed mode maximum output power		5	6	1	nm
1.9	Long-term Power Instability		T = const maximum output power CW & Pulsed mode		± 0.5	± 1	± 0.5	%
Optical output								
2.1	Output Fiber Termination						QBH-compatible connector	Tested
2.2	Beam Quality	BPP ³⁾	50µm core fiber pulsed mode	1		2	2	mm x mrad
General characteristics								
3.1	Cooling Method						Forced Air	
Electrical characteristics								
4.1	Operating Voltage, single phase						200-240 VAC, 50/60 Hz	VAC

¹⁾ Maximum duty cycle limit is inversely proportional to peak power: 10% for 3000W, 15% for 2000W, ..., 50% for 600W and lower.

²⁾ Maximum pulse duration limit is inversely proportional to peak power: 10ms for 3000W, 15ms for 2000W, ..., 50ms for 600W and lower.

3) Measurement tolerance for BPP is +/- 10%.

	TEST RESULTS YTTERBIUM FIBER LASER Model YLR-300/3000-QCW-MM-AC S/N PLMP31901422	Form: Revision: Spec: Page:	P69-00051 1 G22-29650 rev.4 2 of 6
---	---	--------------------------------------	---

N	Characteristic	Test Conditions	Test Results
Laser Interfaces			
5.1	Control	Analog	Tested
		RS-232	Tested
		Ethernet	Tested

Date: 29.10.2019

Tested by: Henry Thepsimoung

Approved by: Thomas Rogers

This document has been created automatically and is valid without a signature

	TEST RESULTS YTTERBIUM FIBER LASER Model YLR-300/3000-QCW-MM-AC S/N PLMP31901422	Form: Revision: Spec: Page:	P69-00051 1 G22-29650 rev.4 3 of 6
--	---	--------------------------------------	---

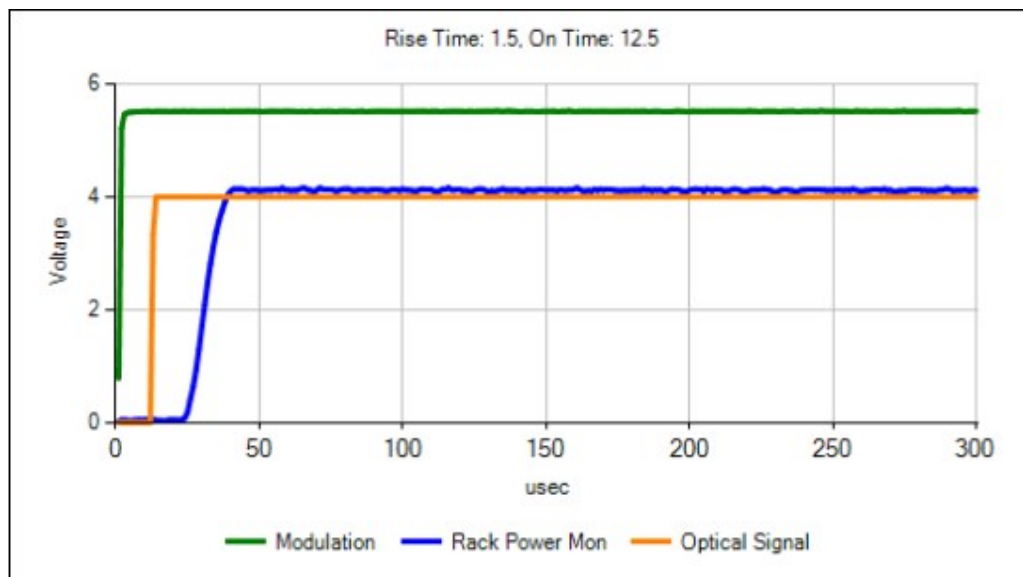


Fig. 1 Switching ON characteristic at nominal output power

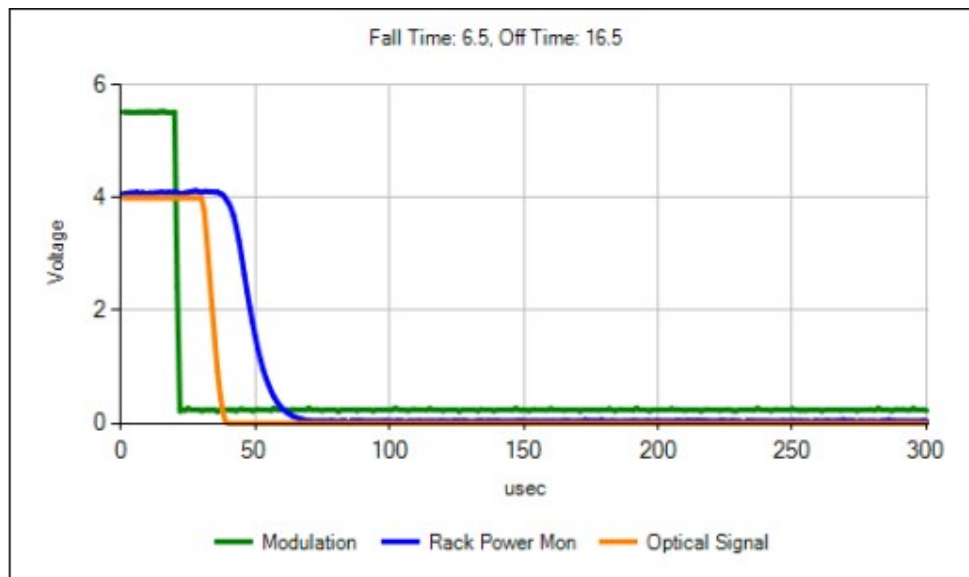


Fig. 2 Switching OFF characteristic at nominal output power

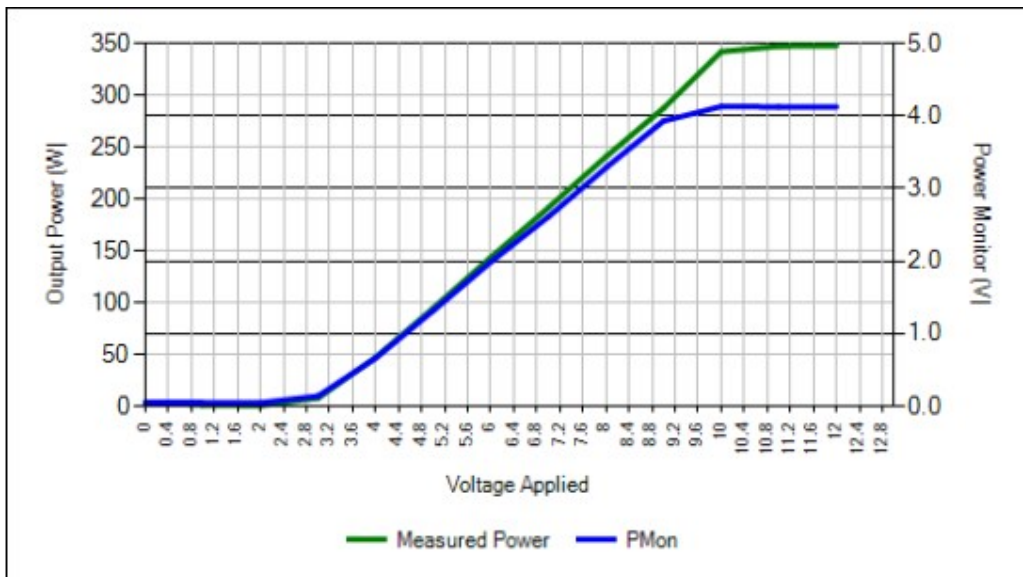


Fig. 3 CW Mode: Output Power vs. Analog Voltage

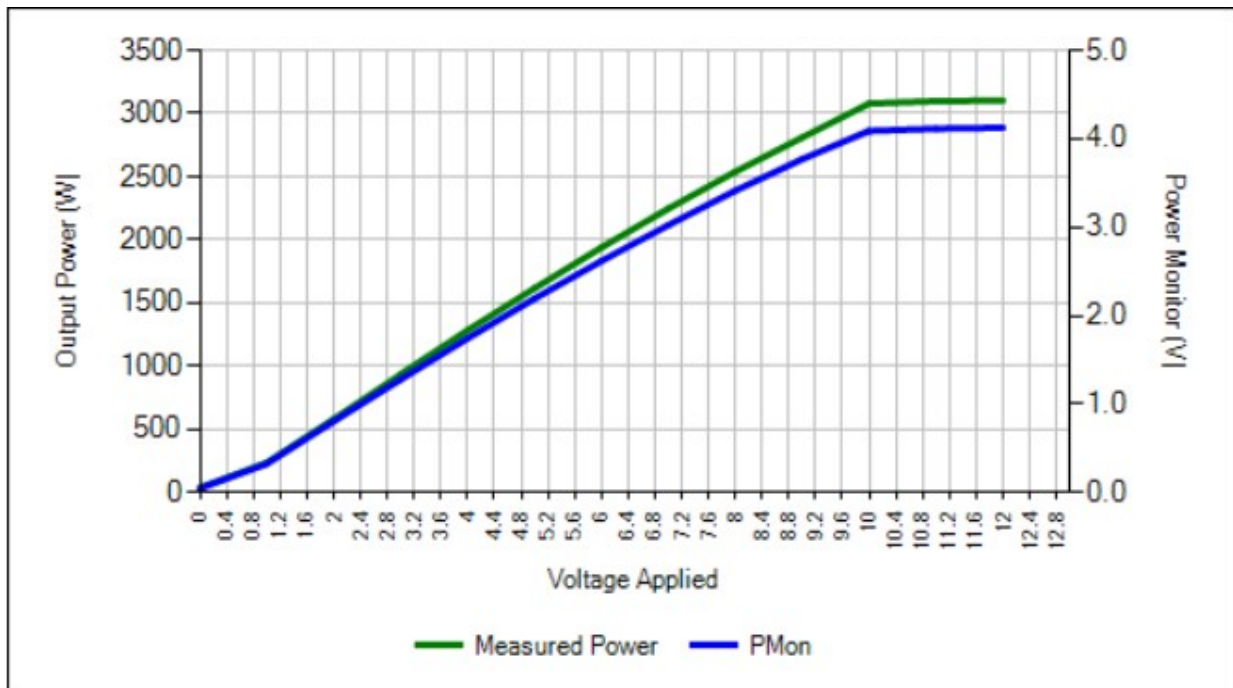


Fig. 4 Pulsed Mode: Peak Output vs. Analog Voltage at RR=10Hz, 10% Duty Cycle

IPG PHOTONICS	TEST RESULTS YTTERBIUM FIBER LASER Model YLR-300/3000-QCW-MM-AC S/N PLMP31901422	Form: Revision: Spec: Page:	P69-00051 1 G22-29650 rev.4 5 of 6
-------------------------	---	--------------------------------------	---

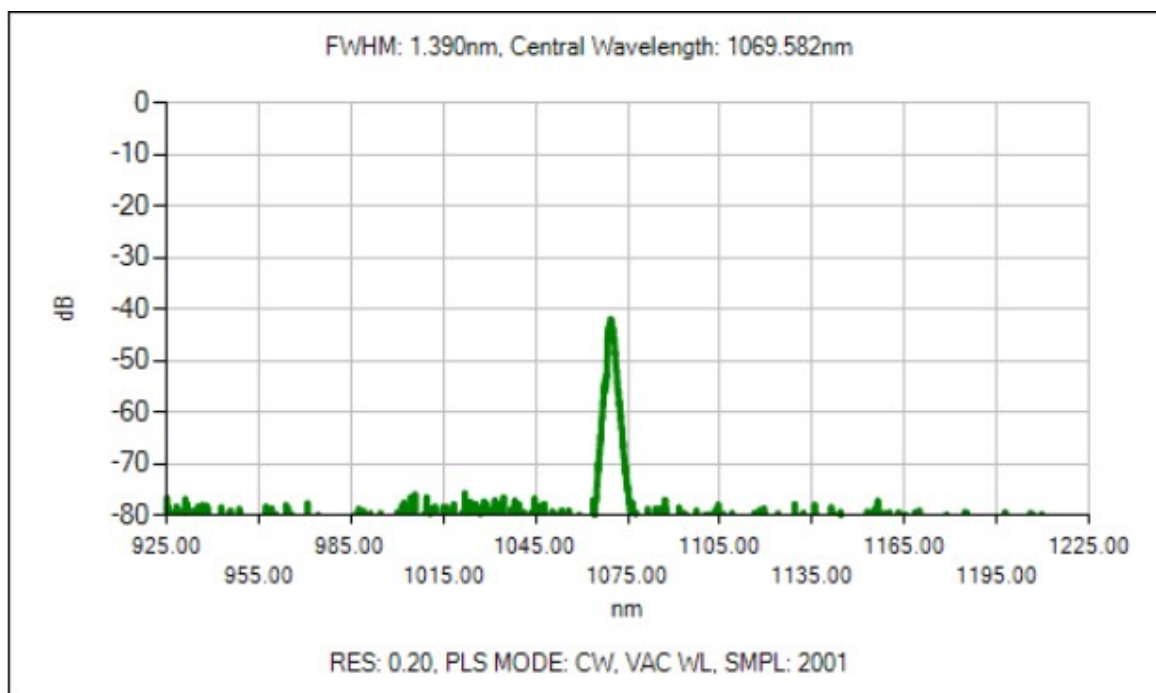


Fig. 5 Output Spectrum at Nominal Output Power

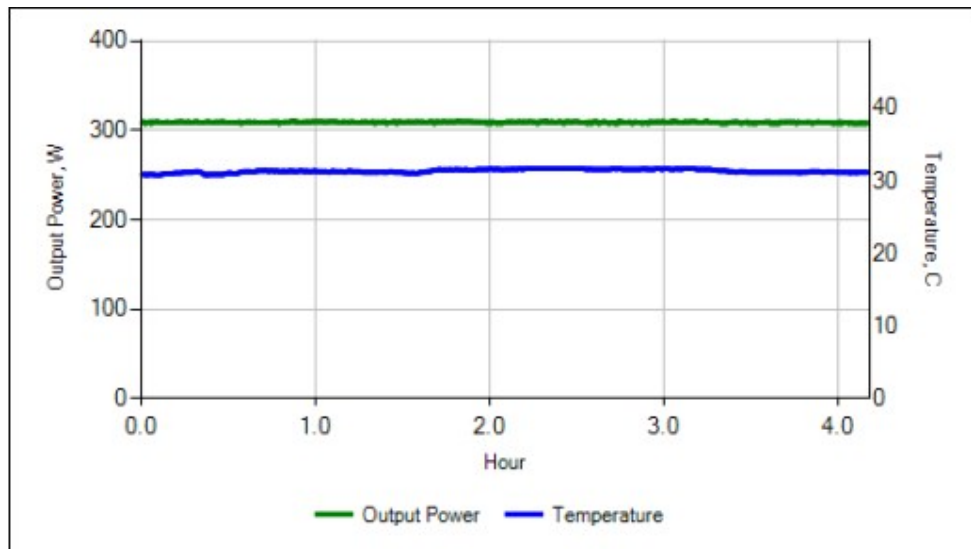


Fig. 6 Output Power Stability Chart

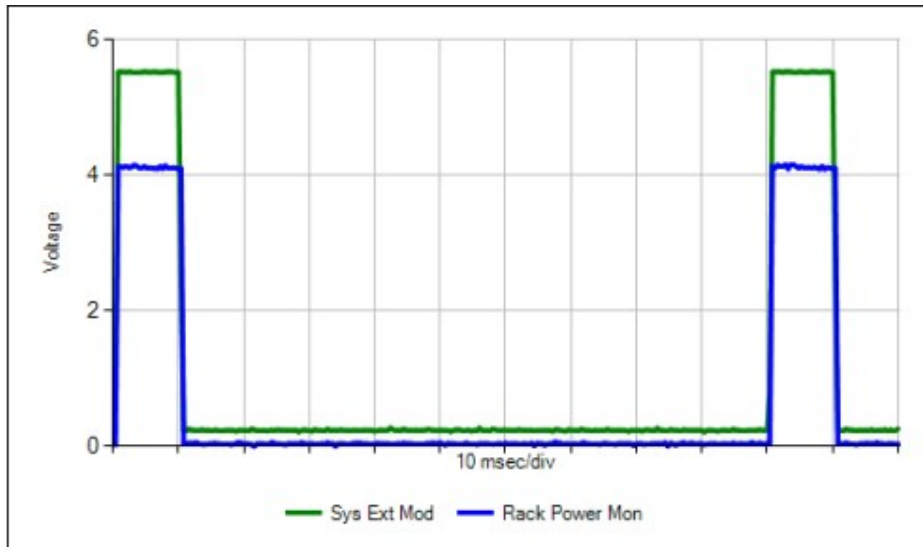


Fig. 7 Pulsed Mode: Laser Output Signal Frequency 10Hz (10% Duty Cycle)

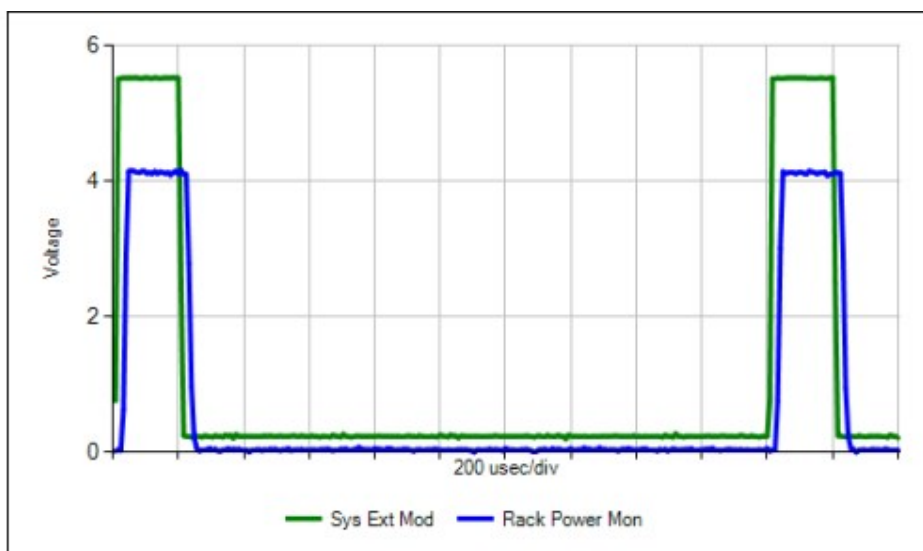


Fig. 8 Pulsed Mode: Laser Output Signal Frequency 500Hz (10% Duty Cycle)

Appendix B

P30 Collimator Calibration Report



Model: P30-001736

Serial Number: CO211706

Date: 3/29/2022 3:11:04 PM

Tested By: Ketsana Chanthavangso

Collimator Test Results Sheet

Characteristic	Conditions	Min.	Typical	Max.	Tested	Units
Z-Position	Measured at Beam Waist				-0.066	m
BPP	Algo. 2nd 100 W			2.5	1.472	mm*mrad
Safety Interlock	Circuit Continuity Tested				Pass	-
Leak Testing	80psi Air for 15min.					-

Raw-Beam:



Raw-Beam:

Position Z:	-66.288 [mm]
Position Z(X):	-3.131 [m]
Position Z(Y):	3.635 [m]
Raw-Beam Radius:	6.813 [mm]
Raw-Beam Radius (X):	6.814 [mm]
Raw-Beam Radius (Y):	6.917 [mm]
Rayleigh length:	31.531 [m]
Rayleigh length X:	29.099 [m]
Rayleigh length Y:	33.790 [m]
Divergence Angle:	0.432[mrad]
Divergence Angle (X):	0.455[mrad]
Divergence Angle (Y):	0.409[mrad]
Raw-Beam Dia. at Laser	13.626[mm]

Exit

Appendix C

Bubble Meter Calibration Report and A^* Calculation

Bubble Meter Performance and Feed Throat Area Calculation for a Laser-Powered Rocket Engine

Thariq Meulendijks

July 31, 2024

This document provides clarification on the results of the bubble meter and explains how these results can be used to determine the flow speed, mass flow, and critical area A^* . The application of this study focuses on the argon flow entering a combustion chamber and exiting via a nozzle.

Chapter 1: Flow Regulator Results

Volume Flow Calculation

Given that 1 mole of an ideal gas occupies 22.4 liters and the molar mass of argon is 40 g/mol, the volume flow rate (Q) for a mass flow rate (\dot{m}) of 0.6 g/s can be calculated as follows:

$$\dot{n} = \frac{\dot{m}}{M} = \frac{0.6 \text{ g s}^{-1}}{40 \text{ g mol}^{-1}} = 0.015 \text{ mol s}^{-1} \quad (1)$$

$$Q = \dot{n} \times 22.4 \text{ L mol}^{-1} = 0.015 \text{ mol s}^{-1} \times 22.4 \text{ L mol}^{-1} = 0.336 \text{ L s}^{-1} \quad (2)$$

Thus, the volume flow rate is 0.336 L s⁻¹.

Results for Air

The flow regulator was tested with air at pressures of 50 psi and 100 psi. The results are summarized in the following table:

Table 1: Flow rate of air through the regulator at different rotations and pressures.

Rotation increments	50 psi (L s ⁻¹)	100 psi (L s ⁻¹)
0.50	0.026	0.048
1.00	0.039	0.067
1.10	0.048	0.085
1.20	0.065	0.125
1.30	0.089	0.168
1.40	0.116	0.221
1.50	0.140	0.253
1.60	0.161	0.306
1.66	0.172	0.336
1.70	0.184	0.345
1.80	0.204	0.381
1.90	0.228	0.425
2.00	0.244	0.460
2.42	0.336	0.656

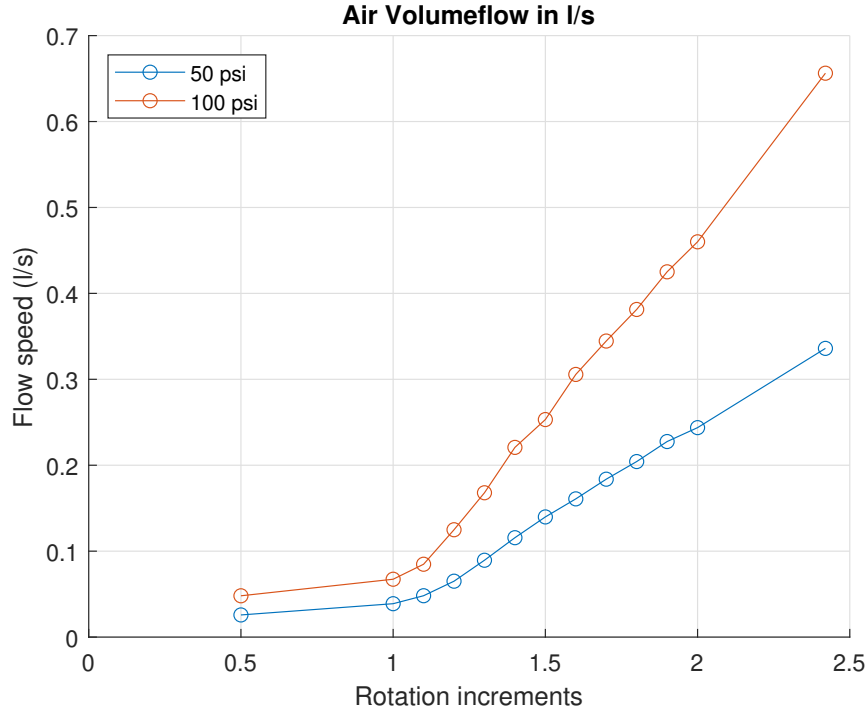


Figure 1: Flow rate vs Rotation for the flow regulator at 50 psi and 100 psi for air.

It can be concluded that the needle valve acts linearly to pressure increase.

Results for Argon

The flow regulator was tested with argon at pressures of 2000 kPa and 5000 kPa. The results are summarized in the following table:

Table 2: Flow rate of argon through the regulator at different rotations and pressures.

Rotation increments	2000 kPa (L s^{-1})	5000 kPa (L s^{-1})
0.50	0.12	0.25
1.00	0.17	0.37
1.10	0.20	0.51
1.20	0.27	0.67
1.30	0.39	1.24
1.40	0.49	1.52
1.50	0.61	1.88
1.60	0.73	2.29
1.66	0.80	2.54
1.70	0.90	2.84
1.80	1.05	3.20
1.90	1.14	3.41
2.00	1.28	3.99

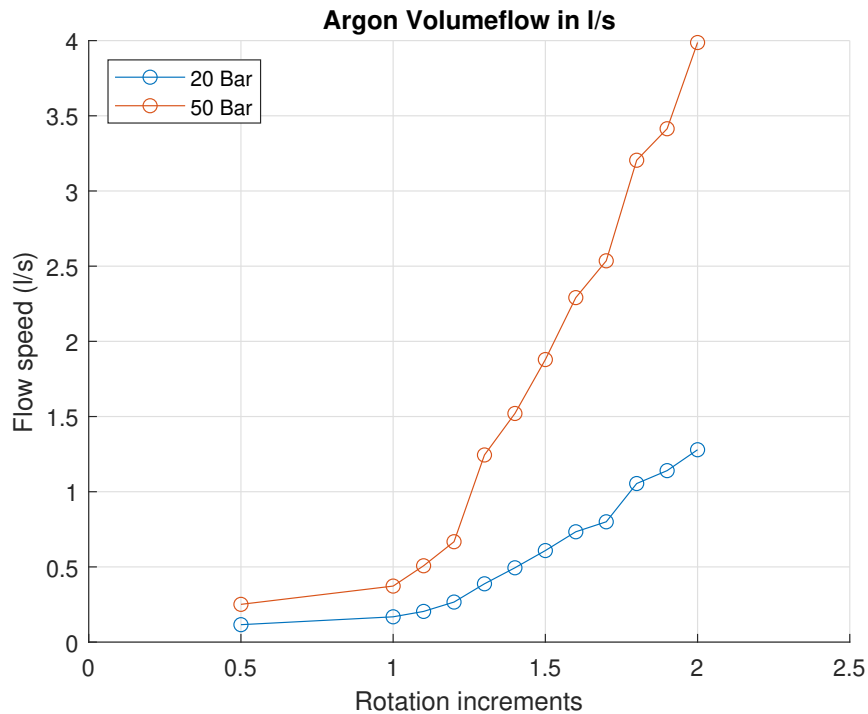


Figure 2: Flow rate vs Rotation for the flow regulator at 2000 kPa and 5000 kPa for argon.

The same linear relationship holds for argon as well.

Summary

The results demonstrate that the needle valve exhibits a linear response to pressure increases for both air and argon. The required volume flow rates can be achieved by adjusting the needle valve rotations accordingly.

Chapter 2: Calculation of A^* for Argon System

Parameters and Introduction

The critical area A^* is calculated based on the mass flow rate of 0.6 g/s of argon. The parameters used in the calculation are:

- Pressure at needle valve entry (P_0): 5000 kPa
- Temperature (T): 293 K
- Pressure in the combustion chamber (P_c): 2000 kPa
- Mass flow (\dot{m}): 0.6 g/s
- Gas constant for argon (R): 208.13 J/(kg·K)
- Specific heat ratio for argon ($\gamma = 1.67$)

Calculation of A^* for the test setup

The critical area A^* can be calculated using the equation for choked flow:

$$\dot{m} = A^* \cdot P_0 \cdot \sqrt{\frac{\gamma}{R \cdot T}} \cdot \left(\frac{2}{\gamma+1} \right)^{\frac{\gamma+1}{2(\gamma-1)}} \quad (3)$$

Rearranging for A^* :

$$A^* = \frac{\dot{m}}{P_0 \cdot \sqrt{\frac{\gamma}{R \cdot T}} \cdot \left(\frac{2}{\gamma+1} \right)^{\frac{\gamma+1}{2(\gamma-1)}}} \quad (4)$$

Substituting the values:

$$\begin{aligned} A^* &= \frac{0.0006}{5000 \times 10^3 \cdot \sqrt{\frac{1.67}{208.13 \cdot 293}} \cdot \left(\frac{2}{1.67+1} \right)^{\frac{1.67+1}{2(1.67-1)}}} \\ A^* &= 4.071 \times 10^{-8} \text{ m}^2 \\ A^* &= 0.04071 \text{ mm}^2 \end{aligned} \quad (5)$$

Volume Flow and Density at Given Pressures

The volume flow (\dot{V}) can be calculated using the ideal gas law:

$$\dot{V} = \frac{\dot{m} \cdot R \cdot T}{P_0} \quad (6)$$

Substituting the values:

$$\begin{aligned} \dot{V} &= \frac{0.0006 \cdot 208.13 \cdot 293}{5000 \times 10^3} \\ \dot{V} &= 7.318 \times 10^{-6} \text{ m}^3/\text{s} \\ \dot{V} &= 0.007321/\text{s} \end{aligned} \quad (7)$$

The density (ρ) of argon at $P_0 = 5000$ kPa and 293 K can be calculated as:

$$\rho = \frac{P_0}{R \cdot T} \quad (8)$$

$$\begin{aligned} \rho &= \frac{5000 \times 10^3}{208.13 \cdot 293} \\ \rho &= 81.99 \text{ kg/m}^3 \end{aligned} \quad (9)$$

Rotation increments for different opening areas

With all the previous information, the opening area of the needle valve can be calculated for different opening positions. This is done by calculating the mass flow rate for all the volume flows at different increments and then calculating the opening area using Equation 4. This results in the table displayed below.

We calculate the opening area for each rotation increment provided in the argon table at a given upstream pressure ($P_0 = 5000$ kPa).

Table 3: Calculated Opening Area for Needle Valve at Different Rotations (Upstream Pressure = 5000 kPa and Outlet Pressure = 100 kPa)

Increment	Volume Flow (L/s)	Mass Flow (g/s)	Area (mm ²)	Diameter (mm)
0.50	0.25	0.41	0.028	0.188
1.00	0.37	0.61	0.041	0.229
1.10	0.51	0.84	0.057	0.269
1.20	0.67	1.10	0.075	0.308
1.30	1.24	2.03	0.138	0.419
1.40	1.52	2.49	0.169	0.464
1.50	1.88	3.08	0.210	0.517
1.60	2.29	3.76	0.255	0.570
1.66	2.54	4.17	0.283	0.600
1.70	2.84	4.66	0.317	0.635
1.80	3.20	5.25	0.357	0.674
1.90	3.41	5.59	0.380	0.696
2.00	3.99	6.54	0.445	0.752

Summary

These results are computed for the test setup and not for the experiment. This will later be compared to how this can be adapted to the experiment. For the test setup, $P_0 = 5000 \text{ kPa}$ is used as the incoming pressure, and after the needle valve, the flow is released into the atmosphere with a pressure of $P_a = 100 \text{ kPa}$. Because of this high-pressure difference, only a very low volume flow is required to fulfill the requirement of the mass flow rate. Later on, the volume flow and mass flow will remain the same, but the A^* will change due to the different pressure conditions.

Chapter 3: Calculation of A^* for the Experiment

In this chapter, we will calculate the critical area (A^*) for a needle valve with an inlet pressure (P_0) of 50 bar, which exits into a compression chamber with a pressure (P_c) of 20 bar. The temperature in the chamber is considered to be 1200 K.

Parameters and Formula

To calculate A^* , we use the pressure difference ($P_0 - P_c$) instead of just the upstream pressure. This approach is valid because the flow rate through the valve is driven by the pressure difference between the inlet and the outlet, which directly influences the velocity of the gas and the resulting mass flow rate. Also, from now on, the mass flow rate is slightly adjusted to meet the required mass flow rate of the experiment.

The general equation for calculating the critical area (A^*) is:

$$A^* = \frac{\dot{m}}{(P_0 - P_c) \cdot \sqrt{\frac{\gamma}{RT}} \cdot \left(\frac{2}{\gamma+1}\right)^{\frac{\gamma+1}{2(\gamma-1)}}} \quad (10)$$

The given parameters are:

- Mass flow rate, $\dot{m} = 0.641 \text{ g/s} = 0.000641 \text{ kg/s}$
- Upstream pressure, $P_0 = 50 \text{ bar} = 5 \times 10^6 \text{ Pa}$
- Downstream pressure, $P_c = 20 \text{ bar} = 2 \times 10^6 \text{ Pa}$
- Pressure difference, $\Delta P = P_0 - P_c = 30 \text{ bar} = 3 \times 10^6 \text{ Pa}$
- Specific heat ratio for argon, $\gamma = 1.67$

- Gas constant for argon, $R = 208.13 \text{ J/(kg}\cdot\text{K)}$
- Temperature in the chamber, $T = 1200 \text{ K}$

Calculation of A^*

Substituting these values into the formula:

$$A^* = \frac{0.000641}{3 \times 10^6 \cdot \sqrt{\frac{1.67}{208.13 \cdot 1200}} \cdot \left(\frac{2}{1.67+1}\right)^{\frac{1.67+1}{2(1.67-1)}}} \quad (11)$$

$$A^* = 1.4695 \times 10^{-7} \text{ m}^2$$

$$A^* = 0.147 \text{ mm}^2$$

This results in a diameter for A^* of $d = 0.4326 \text{ mm}$

Summary

The calculated critical area A^* for the needle valve, with an inlet pressure of 50 bar and exiting into a compression chamber with a pressure of 20 bar at a temperature of 1200 K, is 0.147 mm^2 . This area ensures the desired mass flow rate of 0.641 g/s under the given conditions. Understanding this critical area is crucial for accurately controlling the flow rates and achieving efficient performance in the laser-powered rocket engine.

Chapter 4: Conclusion and Recommendation

Conclusion

The document demonstrated that the needle valve exhibits a linear response to pressure increases for both air and argon, with the required volume flow rates achievable by adjusting the needle valve rotations. The critical area A^* for the test and experimental setups was calculated, showing that the flow rates can be accurately controlled by considering the pressure differences and temperature conditions.

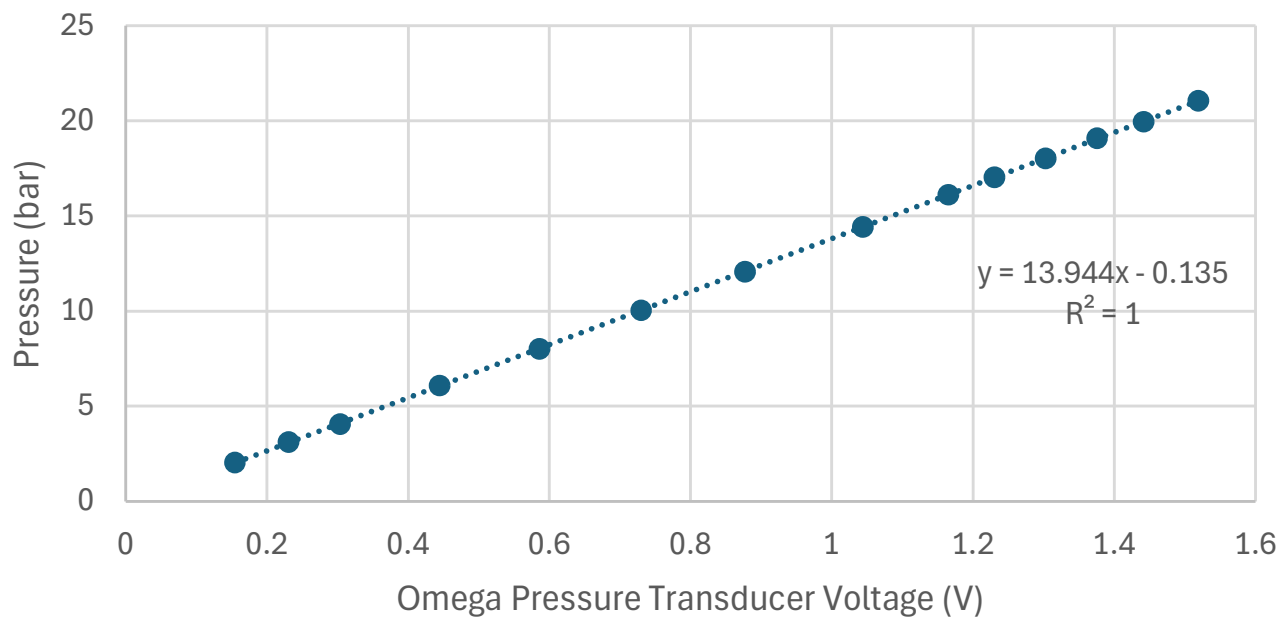
Recommendation

For future experiments, it is recommended to use a rotation increment of approximately 1.33 to achieve an A^* of 0.147 mm^2 with a diameter $d = 0.433 \text{ mm}$ and a mass flow of 0.641 g/s. This way, all the requirements are met. Keep close monitoring of the pressure in the combustion chamber to ensure it stays at 20 bar. If the pressure increases, this could indicate that the nozzle exit is dirty and therefore has a narrower diameter than supposed. For checking the calculations, the MATLAB script used is included in the appendix.

Appendix D

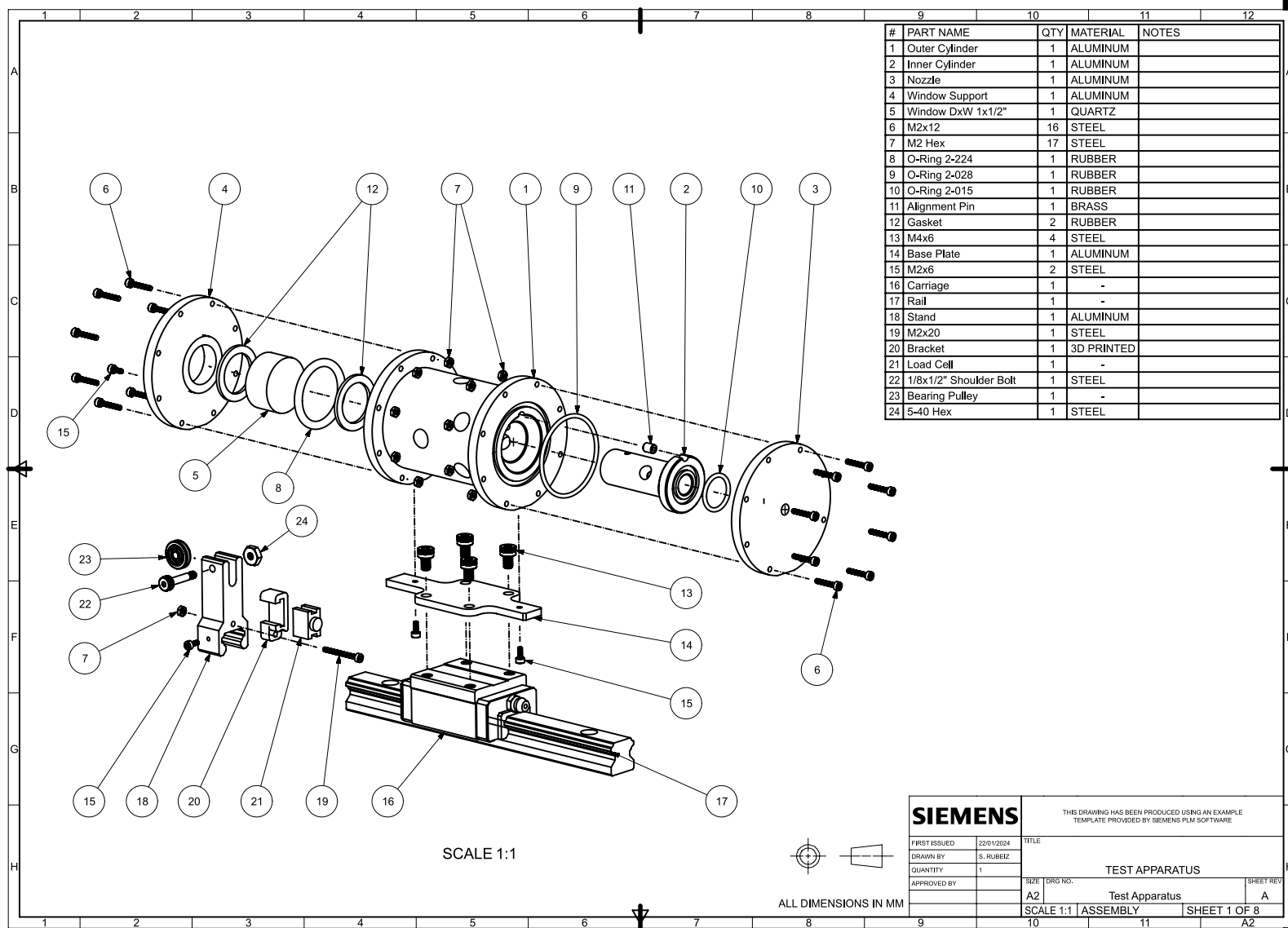
Omega PX119A-1KG5V Calibration

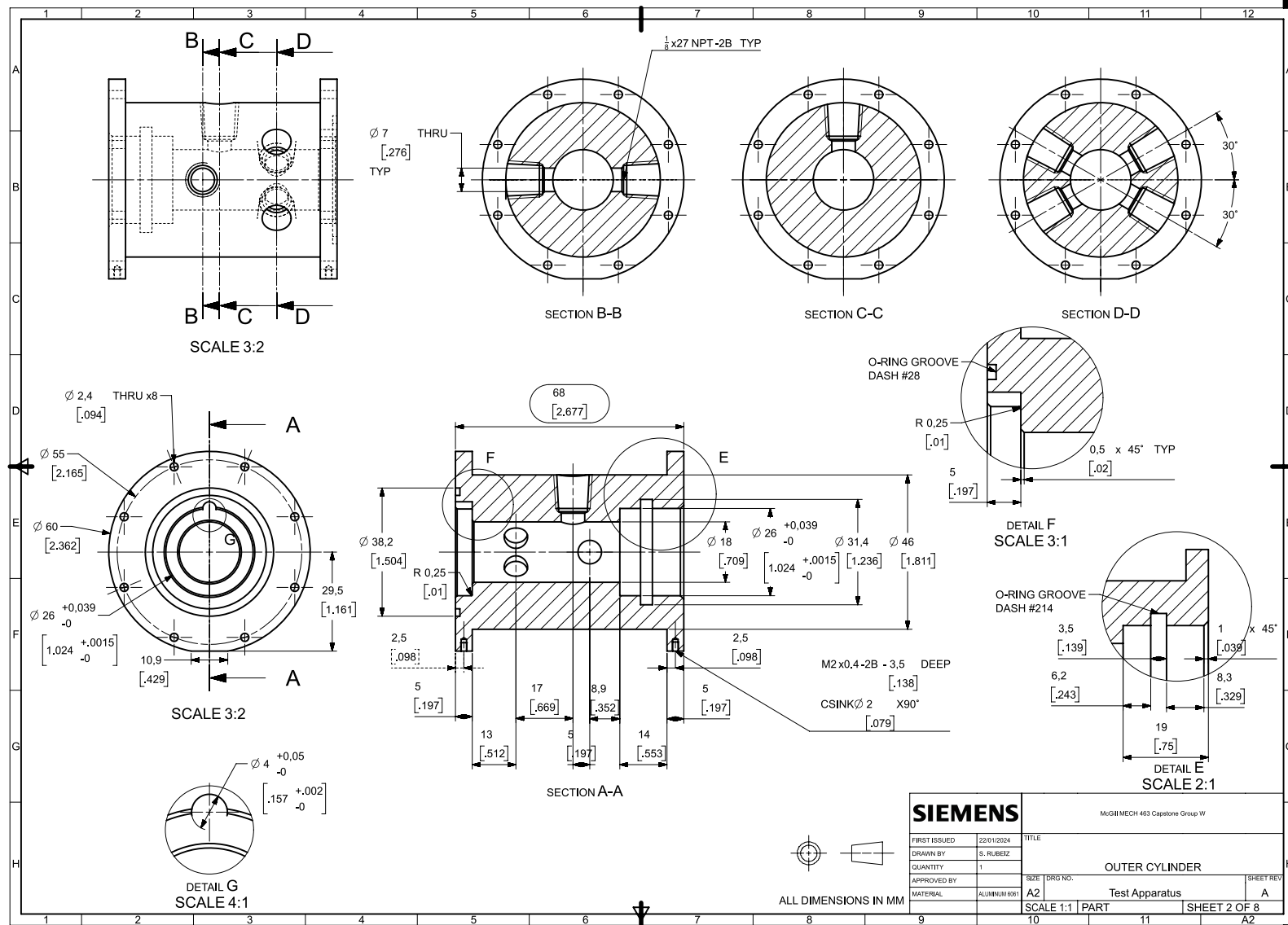
Omega PX119A-1KG5V Calibration



Appendix E

V2 Test Section Parts Drawings



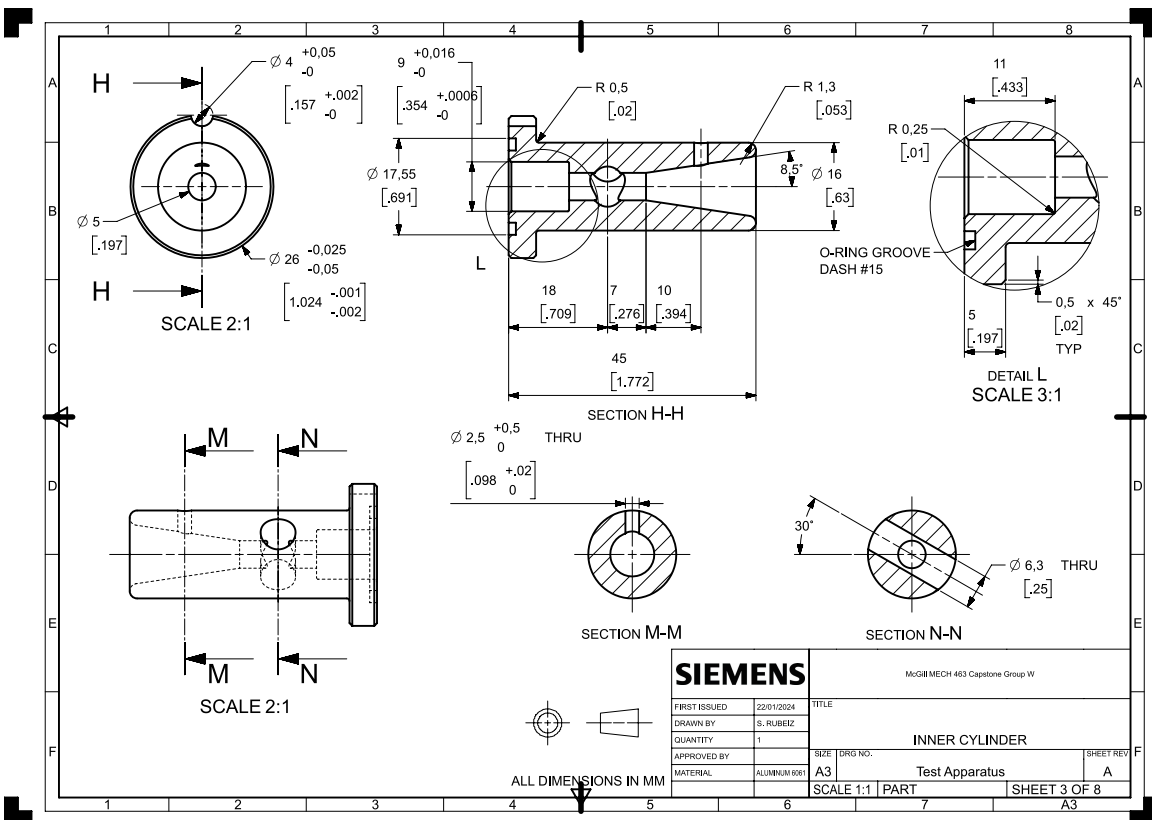


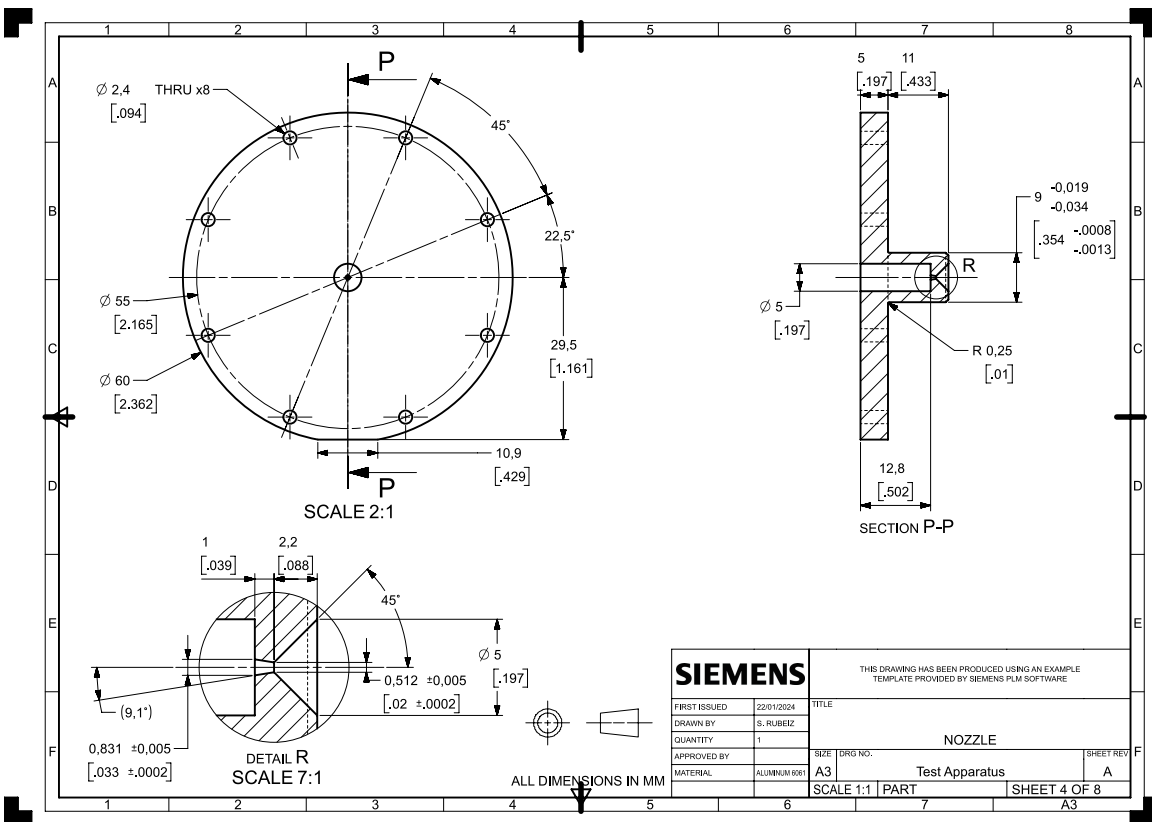
SIEMENS

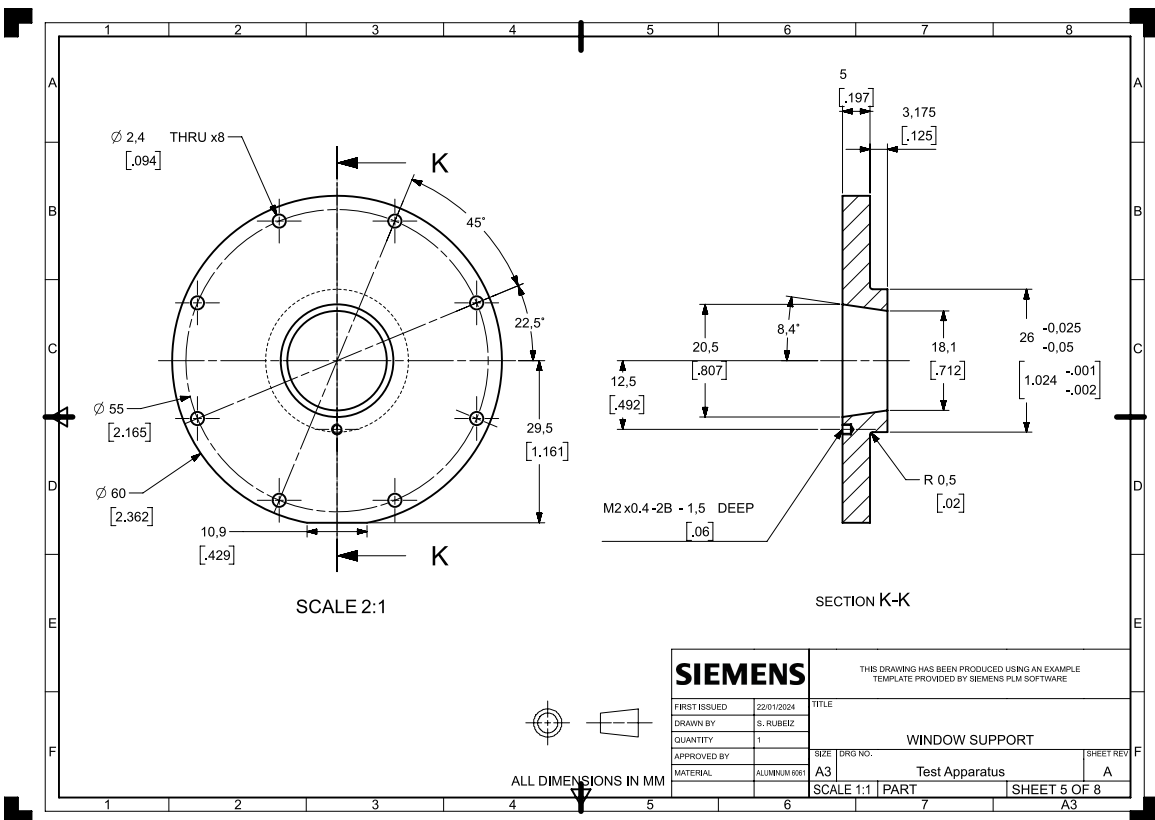
McGILL MECH 463 Capstone Group W

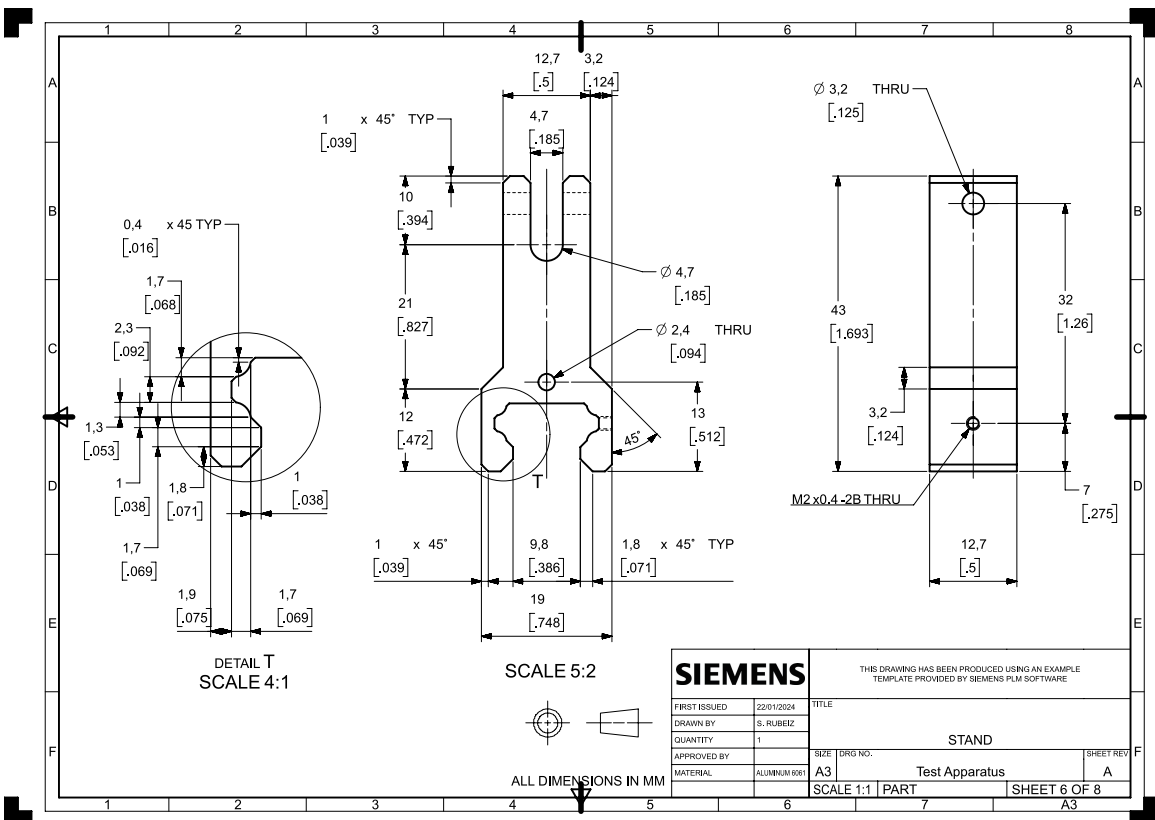
FIRST ISSUED	22/01/2024	TITLE	
DRAWN BY	S. RUBEZ	OUTER CYLINDER	
QUANTITY	1	SIZE	DRG NO.
APPROVED BY		A2	Test Apparatus
MATERIAL	ALUMINUM 6061	SCALE 1:1	PART
			SHEET REV A
			SHEET 2 OF 8

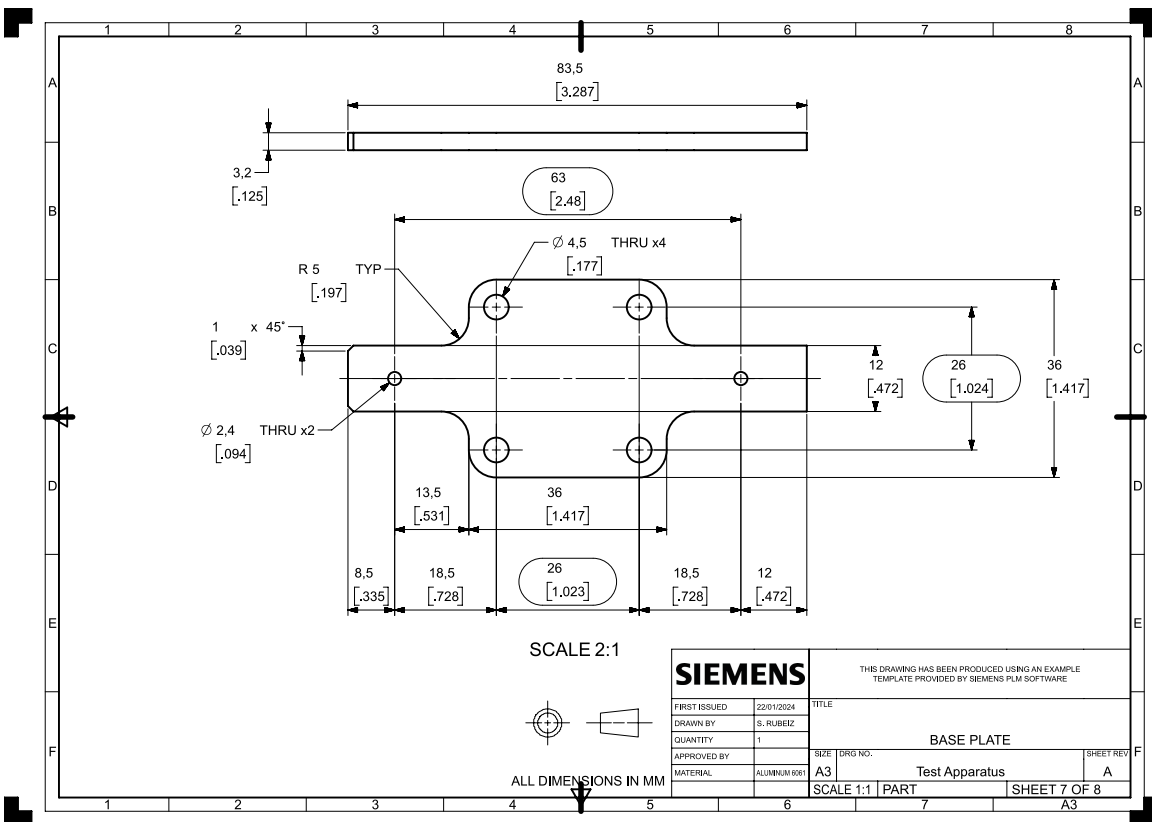
ALL DIMENSIONS IN MM

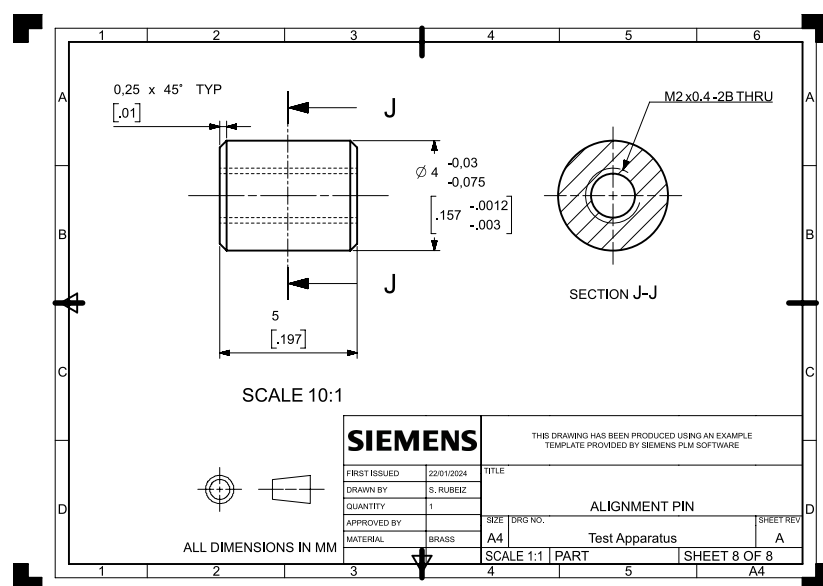






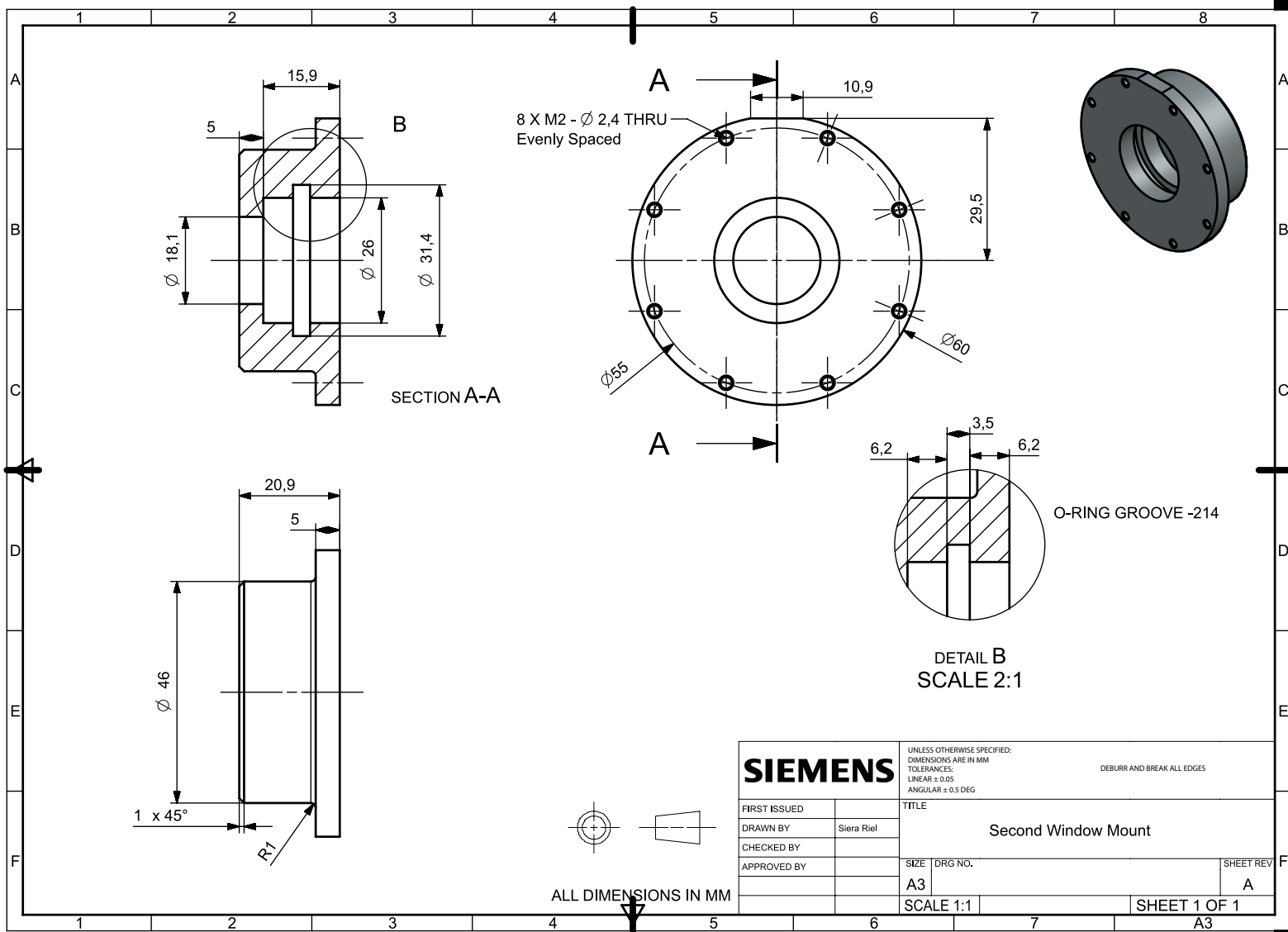






Appendix F

V2 Second (Rear) Window Mount



Appendix G

Untested V2 Parts Drawings

